Fall 2011

Alloy dissolution in argon stirred steel

Darryl S. Webber

Department: Materials Science and Engineering

ALLOY DISSOLUTION IN ARGON STIRRED STEEL

by

DARRYL SCOTT WEBBER

A DISSERTATION

Presented to the Graduate Faculty of the

MISSOURI UNIVERSITY OF SCIENCE AND TECHNOLOGY

In Partial Fulfillment of the Requirements for the Degree

DOCTOR OF PHILOSOPHY

in

METALLURGICAL ENGINEERING

2011

Approved by

Kent D. Peaslee, Advisor
Von L. Richards, Advisor
Simon Lekakh
William G. Fahrenholtz
VK Sharma

ABSTRACT

Alloying is required for the production of all steel products from small castings to large beams. Addition of large quantities of bulk alloys can result in alloy segregation and inconsistent alloy recovery. The objective of this research was to better understand alloy dissolution in liquid steel especially as it relates to Missouri S&Ts' patented continuous steelmaking process.

A 45-kilogram capacity ladle with a single porous plug was used to evaluate the effect of four experimental factors on alloy dissolution: alloy species, alloy size or form, argon flow rate, and furnace tap temperature. Four alloys were tested experimentally including Class I low carbon ferromanganese, nickel and tin (as a surrogate for low melting alloys) and Class II ferroniobium. The alloys ranged in size and form from granular to 30 mm diameter lumps.

Experimental results were evaluated using a theoretically based numerical model for the steel shell period, alloy mixing (Class I) and alloy dissolution (Class II). A CFD model of the experimental ladle was used to understand steel motion in the ladle and to provide steel velocity magnitudes for the numerical steel shell model.

Experiments and modeling confirmed that smaller sized alloys have shorter steel shell periods and homogenize faster than larger particles. Increasing the argon flow rate shortened mixing times and reduced the delay between alloy addition and the first appearance of alloy in the melt. In addition, for every five degree increase in steel bath temperature the steel shell period was shortened by approximately four percent. Class II ferroniobium alloy dissolution was an order of magnitude slower than Class I alloy mixing.

ACKNOWLEDGMENTS

This material is based upon work supported by the U.S. Department of Energy under cooperative agreement number DE-FC36-03ID14279. Any opinions, findings, and conclusions or recommendations expressed in the material are of the author and do not necessarily reflect the views of the Department of Energy.

I would like to thank my co-advisor, Dr. Kent Peaslee for his great patience, financial support, and for allowing me to watch him teach and interact with students. I would also like to thank my co- advisor, Dr. Von Richards, for financial support and scholarships, for inspiring me to be an FEF Key Professor, for finding me a teaching position as an FEF Key Professor, and for being my mentor as a Key Professor. They have both had a tremendous impact on how I conduct myself as a professional.

I would like to acknowledge Dr. Simon Lekakh for being my friend, teacher, CFD modeler, and committee member. He provided an entirely different viewpoint on science, research and kept me entertained and optimistic.

I would also like to acknowledge Dr. VK Sharma for coaxing and coaching me along the path to completion of this dissertation. As well as, Dr. William Fahrenholtz who provided the non-metallurgist view point for this document and who helped me with my approach to teaching thermodynamics.

Finally, I would like to thank my wife Katherine for her unending support in life and my three children who keep me young at heart.

TABLE OF CONTENTS

LIST OF ILLUSTRATIONS

LIST OF TABLES

1. INTRODUCTION AND LITERATURE REVIEW

1.1. PROJECT INTRODUCTION

Alloying is a key step in the production of steel products. Adding large amounts of alloying elements to industrial ladles often results in alloy segregation and inconsistent alloy recovery in the ladle. Argon stirring of the liquid steel using either top lances or through porous plugs in the bottom of the ladle enhances alloy mixing and melting by increasing the heat transfer rates and bulk or convective diffusion.

In addition to the resulting improvement in melting and mixing of alloying agents, argon stirring increases reaction rates, improves alloy recovery, assists in the floatation of inclusions and removal of undesirable gases while promoting a more homogeneous temperature and chemistry.

A new patented process for continuous steelmaking has been developed at Missouri University of Science and Technology. Each argon stirred reactor in the process has liquid metal entering and exiting at the same rate with bulk alloy additions added to adjust the chemistry of the metal exiting the process as needed. Since this is a continuous steelmaking process, a better understanding of the dissolution and mixing of alloy additions in stirred vessels is critical to the operation of the new process.

The purpose of this research is to develop an understanding of the mechanisms of alloy dissolution and mixing in metallurgical reactors to understand the possible regimes of operation in continuous steelmaking with various alloy addition types and forms. In addition, this work is helpful to optimizing alloying in ladle metallurgy facilities in steelmaking and steel foundries. The work summarized in this dissertation includes both experimental alloying in foundry ladles to understand dissolution and mixing in stirred vessels and development of appropriate mathematical models to understand dissolution and mixing.

The laboratory apparatus and experimental procedure were developed through multiple equipment configurations including early work using a lance to introduce argon and a variety of alloys. The final equipment used a bottom mounted porous plug for argon stirring. Three alloys, with melting points below the liquid steel temperature (low

carbon ferromanganese, nickel, and tin), and one with a melting point above the liquid steel temperature (ferroniobium) were chosen for evaluation.

1.1.1. Continuous Steelmaking. In an effort to reduce energy consumption and the cost of steel, researchers at the Missouri University of Science and Technology (Missouri S&T) have studied the design of a novel-scrap based continuous steelmaking process.[1] The system consists of a Consteel® Electric Arc Furnace (EAF) connected to three argon-stirred refining vessels and a tundish.

In the Consteel® furnace, charge material is preheated by furnace off-gas and continuously charged into the EAF. Steel from the EAF continuously flows into an oxidizing vessel for removal of carbon and phosphorus, followed by a reducing vessel where desulfurization, deoxidation, and alloying occur. The steel continuously flows into the finishing vessel for final chemistry adjustment before entering the tundish and continuous caster. A sketch of the continuous steel equipment is shown in Figure 1.1.

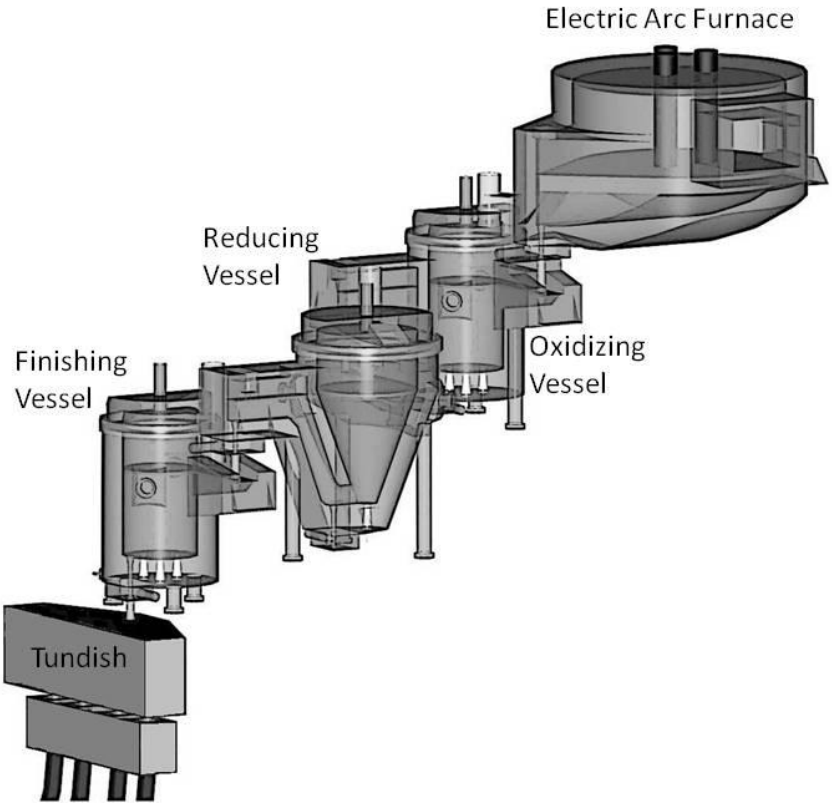

Figure 1.1. Conceptual Sketch of the Continuous Steelmaking Vessels[2]

1.1.1.1 Alloying – bulk or wire. A significant hurdle to the implementation of a continuous process is the assurance that alloy additions are completely mixed and steel composition exiting each vessel is consistent with theoretical calculations. In traditional batch steelmaking, the vast majority of alloying is by bulk additions in the ladle furnace where argon stirring and long hold times assure complete mixing which is confirmed by a final ladle chemical analysis. Some steelmakers make minor chemistry adjustments using cored-wire downstream from the ladle furnace in the tundish but there is little information available as to the actual mixing characteristics. Because of the continuous nature of the continuous steelmaking process, steel chemistry cannot be checked for the batch, therefore, it is critical that alloys are adequately mixed and the chemistry discharged from each vessel is consistent with periodic chemistry checks.

1.1.1.2 Research objective. In order to evaluate alloying concerns in the Missouri S&T continuous steelmaking design, laboratory scale experiments were completed to study dissolution time and mixing characteristics for bulk alloy additions in an argon stirred ladle of steel. This was accomplished by constructing and operating a scale model of an argon stirred ladle and mathematically modeling the system using computational fluid dynamics software and a simplified-spreadsheet based model. Prior to discussing construction, operation, and modeling of the scale model, a summary of the pertinent literature is presented.

1.1.2. Other Applications. Steelmakers benefit from the use of ladle metallurgy, where gas stirring assists in the floatation of inclusions, removal of undesirable gases, enhanced alloy recovery, and a more homogeneous temperature and chemistry. Employment of an argon stirred ladle, similar to that used in the experimental program, could transfer these benefits to steel foundries with ladle capacities much smaller than those used in steelmaking facilities.[3]

1.2. INTRODUCTION TO LITERATURE

Alloy additions are made to overcome deleterious effects of other elements in the molten or solid steel, or to impart or modify physical properties in the finished steel. Sixty to ninety percent of bulk alloy additions are still made to the ladle during tapping of

the steel[4] but there is a trend towards making more additions at the ladle metallurgy station/ladle furnace or even at the tundish using specialty wire products.[5]

No matter where the addition is made, alloy dissolution is an important aspect of the steelmaking process. Ladle hydrodynamics and alloy size, as well as physical and chemical properties affect the way in which the alloy is integrated into the melt. In nearly all cases, the addition of alloys results in the solidification of a steel shell on the surface of the cold alloy followed by a melting of the shell and release of the alloy into the bath. Therefore, alloy dissolution is affected by both mass and heat transfer.

Closed form analytical solutions are seldom found for metallurgical transport processes like alloy dissolution. Such problems can be dealt with through modeling, either physical or mathematical (computational), or with extensive industrial trials. Because of the high temperature and hazards associated with liquid steel, computer and water modeling have been popular approaches to evaluating transport processes.

Modeling of the present research primarily relies on Computational Fluid Dynamics (CFD – Section 1.4), heat and mass transfer (Sections 1.6.1and 1.6.2) and mixing (Section 1.8.3.2). Assumptions for the heat and mass transfer arise from the dissolution behavior described in Section 1.5.4. A discussion of the effect of sampling and alloy addition (Section 1.8.1) helps reconcile the difference between the mixing model and experimental results.

1.3. HYDRODYNAMICS

Molten steel motion increases the rate of alloy dissolution and aids in the flotation of inclusions, while reducing chemical and temperature inhomogeneities. Steel motion is induced by natural convection from temperature gradients, electromagnetic stirring, or by gas injection through a lance, plug, or tuyere. Gas injection via lances and porous plugs is the predominant method of stirring used in industry.

Efficient alloying requires that the alloy be immersed in the steel bath for a sufficient time to melt or dissolve. Low density additions may not penetrate the slag layer or if too large, could float to the surface before melting. In either case, the alloy could be transferred to the slag rather than the metal. High density alloys may sink to the ladle

bottom, where there is less steel movement and potentially lower steel temperatures. Increased steel movement and temperature enhance heat/mass transfer rates.

1.3.1. Melt Circulation. Steel motion initially results from the transfer of steel from the furnace to the ladle. Steel makers frequently add alloys to the stream of metal falling from the furnace to take advantage of the resulting stirring.[6] Fluid friction eventually damps this motion but the melt continues to circulate due to other effects.

Natural convection is buoyancy driven. Steel at the ladle surface cools, becomes denser, causing it to sink. Warmer, less dense, steel flows to the surface to replace the cooled steel. Natural convection aids inclusion flotation, but is not effective for reaction driven processes, like desulfurization or decarburization.[7]

In gas stirred reactors, liquid metal motion is imparted by the transfer of buoyant energy from the rising gas plume to the metal. This exchange of energy results in a recirculating motion (shown schematically in Figure 1.2) characterized by a central rising region, outward flow from the center along the melt surface, and a downward current along the ladle wall. Unfortunately, actual local flow patterns in a gas stirred ladle are transient and/or exhibit inherent instabilities.[8, 9]

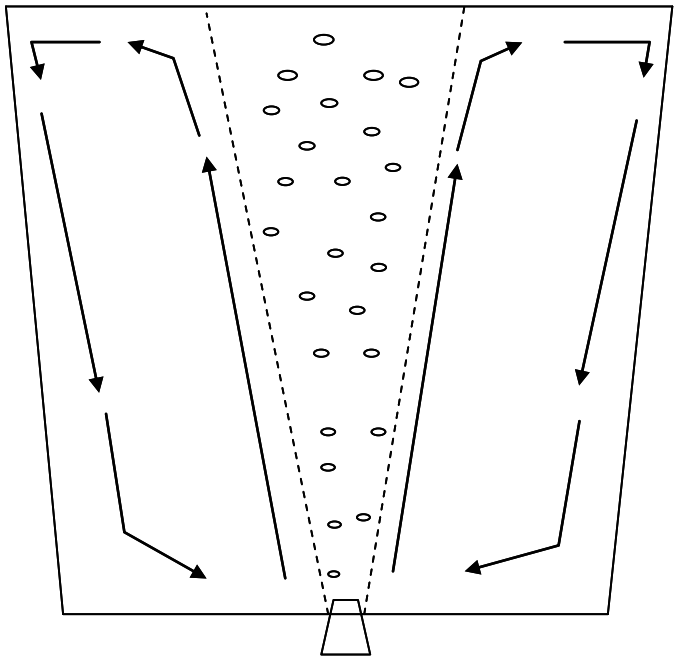

Figure 1.2. Recirculatory Motion in Gas Stirred Ladle

Effective stirring power, $\dot{\varepsilon}$, (equation 1.1) is a semi-empirical measure of the buoyant energy transferred from the bubbles to the metal. It can be used to compare operation of different size ladles and is frequently used in expressions for melt homogenization time (discussed in Section 1.8.2) and was used as a guide in choosing argon flow rates for the present experimental work.[10]

$$\dot{\varepsilon} = \frac{14.23VT}{M}\ln\left(1+\frac{H}{1.48P_O}\right) \tag{1.1}$$

V – gas flow rate (normal m^3 per minute); T – Melt temperature (K);

M – mass of steel (tonnes); H – gas injection depth (m);

P_O – pressure at melt surface (atm)

Stirring power has a direct effect on the velocity of the steel in the mixing vessel, which plays a critical role in heat transfer to alloy particles and in the distribution of alloying elements. Peter et al. compiled stirring power values from literature for several industrial applications. These values are presented in Table 1.1 along with stirring power for two proposed version of the continuous steelmaking oxidizer vessel and the laboratory ladle used for experiments in this dissertation.[11]

Table 1.1. Stirring Power for Industrial Applications and Proposed Continuous Steelmaking Oxidizer Vessel[12]

Application	Stirring Power – watts per ton
Continuous Steelmaking Oxidizer Vessel	370 or 1000
50 t ASEA-SKF (electromagnetic stirred ladle/degasser)	190 to 600
6 t argon stirred ladle	300 to 470
58.9 t argon stirred ladle	23 to70
50 t argon stirred ladle	5.9 to 22
300 t argon stirred ladle	3.4
200 t RH (degasser)	2.8 to 3.7
45 kg laboratory scale ladle	286 to 733

1.3.2. Slip Velocity. Slip velocity, *u*, the relative velocity between an alloy particle and the steel melt, is used in the calculation of heat transfer from the steel melt to the steel shell and for calculation of mass transfer for high melting point alloy dissolution. Slip velocity is a function of local steel velocity and alloy particle initial velocity, size, shape, and density, with the steel shell thickness altering apparent size and density. Zhang and Oeters suggest that even though slip velocity is a function of particle radius, the effect on total melting time (Class I alloys, see Section 1.5.4) is weak and the slip velocity can be assumed constant. This assumption was justified by indicating that melting time is inversely proportional to the square root of slip velocity, while slip velocity is proportional to the square root of radius.[13]

Literature values for slip velocity in the ladle generally range up to 0.5 m/s.[14, 15] When modeling Missouri S&T's scrap-based continuous steelmaking process, Aoki et al. used a slip velocity of 0.4 m/s for silicomanganese dissolution, based on computed flow fields.[16]

Slip velocity is a balance between the particle's inertia and a combination of drag and gravitational forces, which are shown in equation 1.2.[17] Prior to being influenced by steel motion, the inertial term (left hand side of equation 1.2) is due to the velocity of the alloy particle from the free fall into the ladle. Frictional or viscous drag (first term- right hand side equation 1.2) is determined by particle shape and velocity and influences the behavior of the particle subjected to stirring currents within the ladle. The gravitational term determines whether the alloy particle would sink (alloy density greater than melt) or float (alloy density less than melt) in an unstirred melt.

$$-\frac{4\pi}{3}R^3\rho_P\frac{du}{dt}=C_D\frac{\pi}{2}\rho_M R^2u^2-\frac{4\pi}{3}R^3g(\rho_P-\rho_M) \qquad (1.2)$$

R – particle radius; t – time; C_D – drag coefficient; ρ_P – particle density; ρ_M – melt density; g – gravitational acceleration; u – particle velocity

Upon entry into a stagnant bath, the alloy particle will rapidly slow to terminal velocity, u_∞. Terminal velocity, equation 1.3, can be derived from equation 1.2 by setting the acceleration term ($\frac{du}{dt}$) to zero. For example, a four centimeter diameter

ferromanganese particle, falling four meters into a stagnant steel melt would have an initial velocity of about 8 m/s and reach a terminal velocity of 0.3 m/s within one second of entry in the steel; this particle would reach a depth of approximately 95 cm in one second.[18] For a low-density addition such as 75% ferrosilicon, the alloy particle would rise toward the melt surface due to the difference in density between alloy and melt.

$$u_{\infty} = \left(\frac{\rho_P - \rho_M}{\rho_M} \frac{8gR}{3C_D} \right)^{\frac{1}{2}} \tag{1.3}$$

In an agitated bath, Aboutalebi and Khaki used a fluid-flow computational approach to predict slip velocity of solid particles (direct reduced iron) to determine heat transfer rates.[19] Instantaneous slip velocity determination started with the computation of flow profiles in the gas-stirred vessel, followed by evaluation of particle trajectory, to determine local steel velocity as a function of time. A numerical solution is required because of property temperature dependence and non-linear boundary conditions.

For improved accuracy, Aboutalebi and Khaki used an additional term (equation 1.4) in conjunction with equation 1.2, to account for the added mass effect, which is due to the acceleration of fluid adhered to the particle. Additionally, the drag coefficient, C_D, for a spherical particle was determined using semi-empirical relations based on Reynolds number (*Re* - the ratio of inertial force to viscous force; equation 1.5), as shown in Table 1.2. These semi-empirical relations were used in the present work to help ascertain the effect of particle size on slip velocity.

$$F_A = C_A \frac{4\pi}{3} R^3 \rho_P \frac{du}{dt} \tag{1.4}$$

F_A – added mass force; C_A - added mass coefficient

$$\mathrm{Re} = \frac{\rho_M d_{alloy} u}{\mu} \tag{1.5}$$

ρ_M - melt density; d_{alloy} - alloy diameter; μ -melt viscosity

Table 1.2. Semi-empirical Relations between Drag Coefficient and Reynolds Number[20]

Region	Reynolds Number	Relation
Stoke's Law	$10^{-3} < \mathrm{Re} < 2$	$C_D = \frac{24}{\mathrm{Re}}$
Intermediate	$2 \le \mathrm{Re} \le 500$	$C_D = \frac{18.5}{\mathrm{Re}^{0.6}}$
Newton's Law	$500 < \mathrm{Re} \le 2 \times 10^5$	$C_D = 0.44$
	$\mathrm{Re} > 2 \times 10^5$	$C_D = 0.09$

1.4. MATHEMATICAL AND COMPUTATIONAL MODELING

Mathematical models can be developed to describe the hydrodynamics of the ladle and hydrodynamic effects on matters like, alloy trajectory, temperature homogeneity, inclusion flotation, and alloy mixing. Specific discussion of models for alloy dissolution, melting, and mixing along with governing equations are deferred to Section 1.6.

Developing a mathematical model for stirred ladles requires making simplifying assumptions. Many models assume that the ladle is cylindrical and axisymmetric, that is the fluid motion is symmetrical about a vertical axis through the center of the ladle. This contrasts with industrial practice where the ladle is not a perfect cylinder, gas injection is typically off-center and can be from multiple porous plugs. Another area of simplification is a reduction in the number of phases. Real systems include four phases, liquid steel, liquid slag (often containing solids), gas, and solid alloy particles. Additional simplifying assumptions might include isothermal conditions (applicable to well mixed industrial scale vessels), ideal gas behavior, and alloy addition made to the center of the gas plume or in a ring concentric with the gas plume.

After boundary conditions are determined, the model is usually evaluated using computational fluid dynamics (CFD). As computing power has increased (and cost decreased), the complexity of the models has increased, resulting in more accurate predictions.

Jauhiainen et al. modeled a 110-tonne production ladle at Rautaruukki Steel to investigate alloy mixing with a pair of porous plugs in four configurations.[21] Rautaruukki Steel uses a two section-truncated conical ladle, which gradually tapers in the main

section and then sharply tapers near the bottom. Mass transport equations were solved using Phoenics software [Concentration, Heat, and Momentum Limited (CHAM); London, UK], with a stirring time of 10 minutes and gas flow rate of 400 liters per minute for each plug. Results indicated that centric gas stirring provided the best mixing but was most sensitive to alloy addition location. The authors attempted to verify the model by comparing model surface velocities to published measurements taken from a ladle at Sandvik Steel.

Investigators at the Missouri University of Science and Technology and the University of Illinois have produced a CFD model of alloy dissolution in a 130 tonne Ladle Metallurgy Furnace (LMF) using FLUENT software [Fluent USA; Lebanon, New Hampshire].[22] Physical verification of the model was performed by taking timed samples from an industrial LMF. Simulated model output, showing distribution of manganese (kg/m^3 in top view and mass fraction in side view) at some time after addition of silicomanganese in a 130 tonne LMF, is depicted in Figure 1.3.

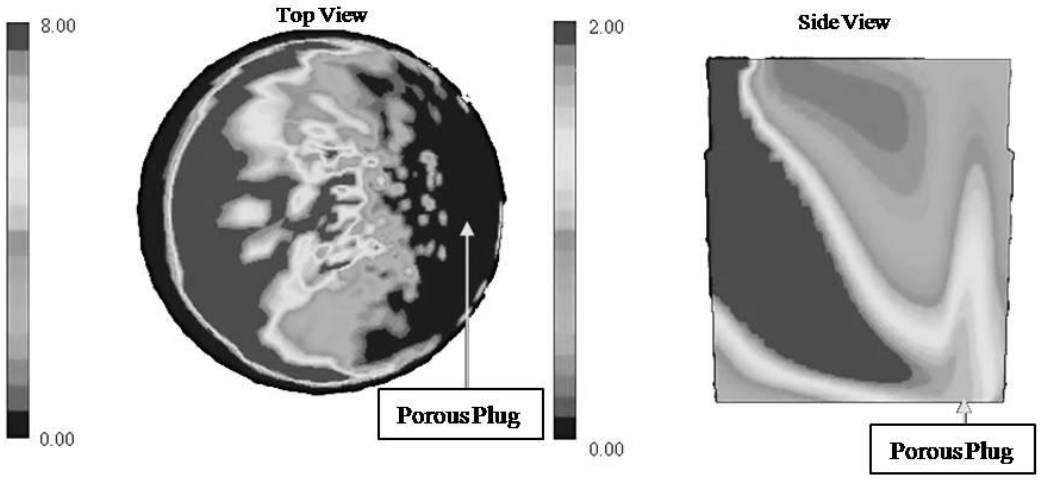

Figure 1.3. Simulated Output from a Computational Fluid Dynamics Model of a Ladle Showing Manganese Distribution for Top (left) and Side (right) Views of a 130 Tonne Ladle Metallurgy Furnace with Offset Porous Plug[23]

The effect of bulk alloy additions to the ladle during furnace tapping was modeled by Berg et al. to determine optimum alloy size and addition timing.[24] During furnace

tapping, a plunging steel jet creates molten metal circulation in the ladle, which affects the motion of alloy additions. Fluent (version 4.4) CFD software was used to determine both the motion of steel and alloy trajectories in the ladle. Simulations were run for six ladle-filling levels, five alloys sizes, and three types of bulk alloys. General conclusions were that 5 to 20 mm alloy particles were more effective than 80 mm alloys, feed rates must be slow enough to prevent alloy agglomeration, and optimum addition timing depends on the specific alloy. Model predictions compared favorably with experiments conducted at two unidentified European steelmaking plants. A simplified schematic of a trajectory model output is depicted in Figure 1.4, where the lines indicate the path of individual alloy particles within the ladle.

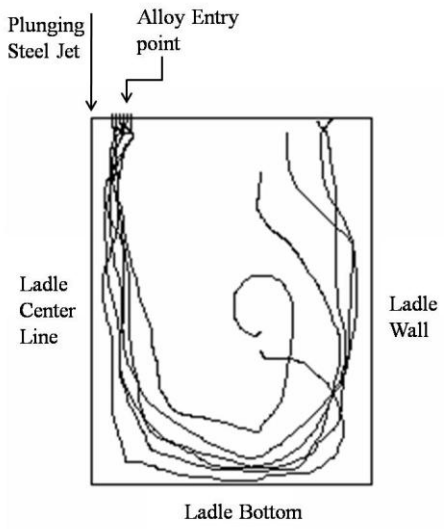

Figure 1.4. Simplified Schematic of Particle Trajectory Model Output, Showing Path of Individual Low-Density Alloy Particles within the Ladle (SiMn alloy enters 25 cm from ladle centerline with ladle 60% filled with a steel jet velocity of 7.2 m/s)[25]

1.5. ALLOY DISSOLUTION

Knowledge of alloy dissolution is essential to determine if bulk alloy additions are feasible for all alloy types in continuous steelmaking. This understanding needs to include parameters like stirring intensity, alloy size, and steel bath temperature. Failure to

properly melt and mix alloys prior to casting would result in rejected product and an economic loss. Excessive temperature, stirring temperature, and/or fine alloy size in pursuit of dissolution would result in unnecessary production cost.

1.5.1. Bulk Alloy Size. Heat transfer driven dissolution kinetics suggests that minimizing alloy size should improve dissolution rate. Unfortunately, small size means more surface area on which to transport undesirable gases and moisture, plus, small alloy size increases dust losses and incurs handling difficulties. Historical practice has been to employ large lumpy additions to aid in penetrating the slag layer for gravimetric additions. Wire and powder injection are both means of introducing small alloy particles into the melt below the slag layer.

Lee et al. determined that the optimum size for bulk alloys, added gravimetrically to the ladle, is between 3 and 20 mm in diameter.[26] Any alloy smaller than 3 mm was deemed impractical to handle in a typical steelmaking environment, while the upper limit was determined by examining the time for 75% ferrosilicon or silicomanganese to float to the steel melt surface or high carbon ferromanganese to sink to the ladle bottom. In what Lee et al. termed 'normal' steelmaking ladles, 20 mm alloy particles would dissolve before reaching the melt surface or ladle bottom. Dissolution times were taken from a previous Lee, Berg, and Jensen publication.[27]

1.5.2. Alloy Wire. Cored steel wire is used to add difficult alloying elements or to make fine (trim) adjustments to steel chemistry in the ladle or tundish. Difficult alloys include species of low density, low melting/boiling point, and excessive reactivity with slag, air or moisture. In addition to alloys, the cored wire can contain fluxes like fluorspar.

Crawford suggests that encasing alloy and flux powders in a 3 to 18 mm diameter steel sheath overcomes the difficulties associated with handling small alloy particles.[28] These difficulties include dust losses and the transport of gases and moisture on the alloy surface. Alloy powder also reaches molten metal without reacting with slag or air at the melt surface. Crawford asserts that wire feeding can often deliver alloys more effectively and with greater repeatability than bulk alloy additions.

Wire feeding equipment is more expensive to purchase and maintain than equipment to make bulk additions. A wire feeder is required for each different alloy wire,

while bulk additions can be made by hand. Alloy wire is also more expensive than the same materials in bulk.

Wire injection is commonly used with very reactive alloys (calcium), for low-density additions (calcium-silicon, aluminum, sulfur), for alloys which form toxic vapors (lead, selenium, tellurium), or for trim additions of micro-alloys (niobium, titanium, vanadium).[29] Boron additions of 0.0005% to 0.005% are a special application where wire feeding is a more accurate and predictable method than bulk alloy addition.[30]

Calcium addition by deep wire injection has significant benefits. At steelmaking temperatures and atmospheric pressure, calcium is a gas. Subsurface ferrostatic pressure at wire injection depth is sufficient to suppress calcium vaporization, resulting in liquid calcium entering the melt. Liquid calcium droplets rise more slowly than vapor, resulting in better calcium recovery and utilization.

Tateyama et al., investigated magnesium wire deoxidation, as an aluminum substitute with the additional benefit of sulfur removal.[31] Like calcium, magnesium is a vapor at steelmaking temperatures and atmospheric pressure, thus, wire injection is probably the best addition method for magnesium.

1.5.3. Alloy Properties. Several physical and chemical properties of the alloys to be added affect how the element is incorporated into the steel melt. The melting point of the alloy in relation to the melt has been identified as the primary factor. Investigators at McGill University have classified alloy additions as either Class I, for alloys that melt below the steel bath temperature and Class II, for alloys that melt above the bath temperature.[32] Class I alloys include: (1) ferromanganese, (2) silicomanganese, (3) ferrochrome, and (4) ferrosilicon. Examples of Class II alloys include: (1) ferrovanadium, (2) ferrotungsten, and (3) ferromolybdenum.

A strong exothermic reaction between the alloy and steel (enthalpy of mixing or reaction between alloy and dissolved oxygen) can substantially reduce the assimilation time. Heat of mixing and heat of dissolution (sum of heat of mixing and heat of fusion) for several alloying elements are given in Table 1.3. The thermal effect column shown in Table 1.4 represents the temperature gain or loss when 0.5 kilograms of alloy is added to 1000 kilograms of steel. This thermal effect includes heat of mixing, energy required to heat the alloy (specific heat) and melt the alloy (heat of fusion) but does not include

reaction with dissolved oxygen. Kubaschewski and Chart indicated that the reaction of aluminum, silicon, or 75% ferrosilicon with 0.01% oxygen would result in an equivalent thermal effect of +3.05, +2.35, or +2.26 ºC per 0.5 kg addition to one ton of steel, respectively.[33]

Table 1.3. Heats of Mixing and Dissolution for Selected Elements in Liquid Iron[34]

Element	Heat of mixing in iron kJ/kg	Heat of dissolution (sum of heat of fusion and mixing) kJ/kg
Aluminum	-2380[35]	-1982
Chromium	-160.8	210.4
Manganese	76.16[36]	344.2
Molybdenum	-165.5	258.5
Niobium	-405.4	-121.6
Nickel	-133.6	158.6
Silicon	-4682[37]	-2756
Tantalum	-249.5	-76.13
Titanium	-1319.4	-996.9
Vanadium	-463.10	-36.1
Zirconium	-905.9	-720.7

From Table 1.4, silicon metal and 75% ferrosilicon should have shortened dissolution times due to exothermic reactions. Several elemental additions (niobium, tantalum, titanium, vanadium, and zirconium) should also show reduced dissolution times, due to an exothermic mixing reaction. In addition to heat of mixing, the exothermic formation of an intermetallic or silicide could reduce assimilation time.

Schade, Argyropoulus and McLean took advantage of silicon's exothermic behavior to develop what they termed microexothermic alloys.[38] Powdered silicon was mixed with powdered alloys (FeMo, FeNb, FeCr) in cored wires. The modified Class II alloys were found to mix up to 80% faster than their unmodified counterparts. Class I, ferrochromium showed no improvement. The authors hypothesized that heat released from the formation of Nb_5Si_3 or Mo_5Si_3 melted the Class II alloys, essentially changing them into a Class I alloy.

Table 1.4. Properties of Selected Ferroalloys and Alloying Elements

Alloy	Liquidus °C[39]	Solidus °C[40]	Thermal Effect °C per 0.5 kg/ton[41]	Thermal Conduct-ivity (W/mK)[42]	Density ratio $\rho_{alloy}/\rho_{steel}$[43]	Heat Capacity (J/kgK)[44]	Latent heat fusion (kJ/kg)[45]
Aluminum[46]	660.25	660.25	+0.09[47]	237	0.385	900	399.9
Chromium Electrolytic/ Aluminothermic	1900/1850	1900/1850	-0.9	60[48]	0.987[49]	972[50]	371.2[51]
Ferrochrome Charge Grade (63% Cr, 5.5% C, 7%Si)	1500	1400	-1.2				
Ferrochrome High Carbon (69% Cr, 4-6% C, 1% Si)	1500	1350	-1.2	12.55[52]	0.982[53]	891[54]	309.0[55]
Ferrochrome Low Carbon (72% Cr 0.01% C/ 0.05% C)	1690/1670	1660/1639	-0.9	*6.50*	*0.977*	*670.0*	*324.5*
Ferromanganese Low Carbon (88% Mn, 0.1% C)	1205	1200	-1.0		1.03		
Ferromanganese Standard (78% Mn, 7% C)	1265	1149	-1.2	7.53	1.03	700.0	534.7
Ferromolybdenum (60% Mo)	1900	1800	-0.7				
Ferroniobium (65% Nb)	1580	1400	-0.7		1.15[56]		
Ferrosilicon (75% Si)	1332	1266	+0.2	2.93[57]	0.399[58]	938[59]	1446.6[60]
Ferrosilicon (65% Si)	1270	1205	-0.1				
Ferrosilicon (50% Si)	1227	1210	-0.4	9.62	0.635	586.0	908.2
Ferrotungsten (90% W)	2500	1650	-0.4				
Manganese[61]	1250	1250	-0.915[62]	50	1.06	800	266.5
Nickel (99% Ni)	1455	1455	-0.7	85.5[63]	1.27[64]	570[65]	292.2[66]
Niobium[67]	2467	2467	-0.36[68]	73.3	1.23	290	405.4
Silicomanganese (67% Mn, 17% Si)	1293	1162	-0.8	6.28	0.797	628.0	578.8
Silicon Metal (98.4% minimum)	1440	1410	+0.8	33.5[69]	0.342[70]	728.5[71]	1621.0[72]
Tin[73]	231.93	231.93		66.6	1.04	277	59.2

Data in *italics* is for low carbon ferrochrome with only 50-58% chromium

Other important alloy properties include density, thermal conductivity, specific heat, and enthalpy of mixing. Density determines whether the addition will float (ferrosilicon), sink (ferroniobium) or be entrained within the melt (ferrochromium). Thermal conductivity along with specific heat and density determine the thickness of the steel shell formed on the cold ferroalloy when added to the liquid steel. These properties, for selected ferroalloys and alloying elements, are compared in Table 1.4, where the density is the ratio of alloy density to the steel melt (7020 kg/m^3).

1.5.4. Routes of Dissolution Argyropoulos and Guthrie published five theoretical dissolution routes, depicted in Figure 1.5, for bulk additions to steel.[74] In almost all cases, a steel shell is frozen onto the surface of the alloy. Heat transferred from the molten bath remelts this shell back to the original alloy surface. Convective heat transfer, which is a function of bath stirring, governs shell melting.

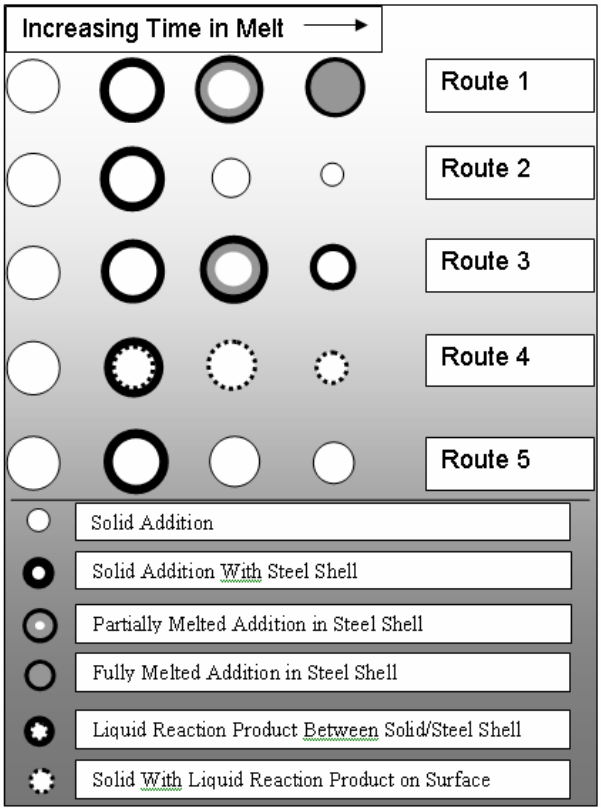

Figure 1.5. Illustration of Proposed Alloy Assimilation Routes. Route 1. Typical for Class I Alloys; Route 2 and 3 Class I Alloys with Low Thermal Conductivity, Large Size, and Excess Superheat; Route 4. Class I Alloys with Substantial Enthalpies of Mixing; Route 5. Class II Alloys[75]

Class I alloys typically melt within the steel shell, so that liquid alloy is released when the steel shell is melted (route 1). Two other routes (routes 2 and 3) exist when the addition lump size is large, the liquid metal is at high superheat and the ferroalloy has low thermal conductivity. In route 2, a very thin steel shell is formed that melts so rapidly that the alloy does not have enough time to melt, or in some cases, the alloy is partially melted, the liquid alloy is released, and a second steel shell forms on the remaining solid (route 3). For routes 2 and 3, assimilation of the remaining solid is still rapid because of the large difference between the bath temperature and alloy melting temperature.[76]

Dissolution of alloys with considerable enthalpies of mixing, e.g. silicon and titanium, follows route number 4. In this case, the alloy exothermically reacts with the inside of the steel shell forming a eutectic liquid, which erodes the shell and speeds bulk melting of the alloy.[77] The exothermic dissolution reaction of silicon and 75% ferrosilicon can be strong enough to rupture the steel shell. In the case of ferrosilicon, Elkem researchers observed that bright white jet streams were ejected radially which resulted in a disappearance of both the ferroalloy lump and steel shell.[78] Energy released by this reaction, while important for alloy dissolution, has only minor effects on the temperature of the bulk steel in industrial practice.

The dissolution of Class II alloys follows the fifth route, which is controlled by a mass transfer phenomenon. A steel shell is formed, remelts, and the solid subsequently dissolves in the melt via diffusion through a liquid boundary layer into the bulk steel.[79] In cases where the solid diffuses across a boundary layer, Argyropoulos indicated that mass transfer rates are typically an order of magnitude slower than the other routes.[80]

1.5.5. Experimental Methods. Alloy dissolution research is complicated by several factors, especially in the industrial environment. Industrial production schedules and the massive size of steelmaking vessels are not conducive to research. Even on a laboratory scale, the high temperatures associated with handling molten steel and the inability to directly observe events in the liquid metal, hamper experiments. Such factors have contributed to most researchers working at small scales and/or substituting low temperature materials for steel, i.e. water, often in conjunction with a computer model. For the literature surveyed, most experiments were conducted with small quantities of molten steel, 40 grams up to a few hundred kilograms, which may not be representative

of conditions encountered in steelmaking with heat sizes up to 300 tons, so care must be exercised when incorporating research results into actual industrial practice.

Investigators have typically used two distinct methods for determining dissolution rates. The first method is to make a bulk addition, then take consecutive samples of the molten metal for chemical analysis.[81] An alternate approach is to immerse an alloy sample in the melt while it is attached to a load cell.[82] Dissolution rate can then be determined by examining the weight loss from the alloy sample as a function of time. In addition to dissolution rates, steel shell formation has been investigated by dipping samples, attached to molybdenum wire, into melts for various lengths of time. After dipping, each sample was sectioned and the thickness measured.[83]

1.5.6. Experimental Results. Gourtsoyannis, Guthrie, and Ratz hung alloy cylinders and lumps attached to a load cell in a steel bath (induction furnace with power either on or off).[84] By measuring the alloy weight versus time they were able to establish mass transfer rates for molybdenum, ferromolybdenum, niobium, and ferroniobium. They found that the dissolution rate of ferromolybdenum in an inductively stirred bath (1600ºC) was five times faster than ferroniobium. However, dissolution of pure niobium "is much faster" than pure molybdenum in an inductively stirred bath (1600ºC). This was attributed to the exothermic mixing of pure niobium with iron.

The alloy cylinders were prone to breaking, so Gourtsoyannis, Guthrie, and Ratz switched to hanging lumps and lump additions with chemical sampling. Their results for standard ferroniobium (66.5% Nb) suspended lumps, and lump additions are given in Table 1.5. Lumps were assumed to be spherical for the purpose of determining surface area. Dissolution rate was then determined as rate of weight change per unit of original surface area.

Scatter in the data was attributed to small variations in chemical composition and crystal structure. The variation was from using remelted cylinders, remelted lumps, and primary lumps (as supplied). No explanation was offered for the lower dissolution rate of the induction stirred (power on) specimen versus the stagnant bath. In spite of the data scatter, the authors concluded that dissolution rate increases with temperature. They then extrapolated their results to stirred steel baths at 1600°C indicating that a 2 inch (50.8 mm) ferroniobium lump would dissolve in 6.4 minutes. They also suggest that

ferroniobium should be crushed to 3 mm in order to completely dissolve the alloy before settling in a 3.5 meter deep bath.

Table 1.5. Dissolution Rates for Standard Ferroniobium Lumps in an Induction Furnace with Power off Versus Steel Bath Temperature [85]

Temperature °C	Dissolution Rate grams per second·cm^2
1575	0.0243
1580	0.0086
1600	0.0043
1600	0.0229
1600	0.0286
1635	0.0471
1650	0.0150*
1650	0.0271
1660	0.0400
1660	0.0571

*Induction power on

1.6. MATHEMATICAL MODELING OF ALLOY MELTING AND MIXING

Modeling of alloying requires the evaluation of the steel shell formation, melting or dissolution, and finally mixing of the liquid or dissolved alloy. The length of time that the steel shell persists and the condition of the alloy when the steel shell disappears are of interest because no alloy enters the melt during this period and a liquid alloy mixes more rapidly than a solid.

Liuyi Zhang and Franz Oeters have published a thorough mathematical treatment of alloy mixing (in the form of a book[86] and follow-up paper[87]). This work served as the basis for the development of the heat transfer portion of the steel-shell model (Section 2.4.3) and Class II dissolution model (Section 2.6). An examination of their work, as related to this research, follows in the sections on the period where a steel shell exists, and alloy melting/dissolution.

1.6.1. Period with a Steel Shell. Upon entering the melt, a steel shell solidifies on the alloy particle, preventing the release of alloying elements. The steel shell period

occurs between the time that the alloy is added and the melting of the steel shell. Development of the shell governing equations is simplified by making a number of assumptions, including spherical alloy particles (radial coordinate, r), sufficient spacing between alloy particles to prevent interaction of boundary layers, high thermal conductivity of the alloy (not the case for high carbon ferroalloys), and initially that no melting occurs beneath the shell.

1.6.1.1 Shell formation without melting. Shell formation without melting behind the steel shell is a balance between alloy particle heating and heat transfer between the melt, shell, and alloy particle.[88] Thus equations need to be written for the temperature changes of the alloy particle, the steel shell, interface of melt and composite particle (combined shell and alloy particle, shown in Figure 1.6), and the interface between alloy particle and shell.

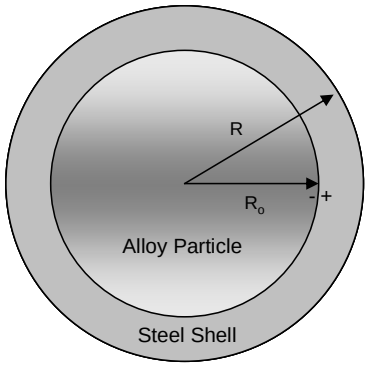

Figure 1.6. Schematic of Alloy Particle with Steel Shell[89]

Alloy heating is given by equation 1.6, where T_P, is the temperature of the alloy particle at time, t, with initial radius, $R_{o,}$ and alloy thermal diffusivity of α_P. At time zero, the alloy particle has an initial temperature, T_o, and surface temperature of the shell, $T_{S,shell}$, which is the solidification temperature of the melt. When the alloy particle enters the melt (t=0), the interior of the alloy is assumed to be room temperature (T_o), while the surface temperature is assumed to immediately reach the solidification temperature of the steel melt.

$$\frac{\partial T_P}{\partial t} = \alpha_P \left[\frac{\partial^2 T_P}{\partial r^2} + \frac{2}{r} \frac{\partial T_P}{\partial r} \right] \qquad 0<r<R_o \tag{1.6}$$

at t =0 {$T_P = T_o$ for $r<R_o$ and $T_P = T_{S,shell}$ for $r= R_o$}; at r =0 {$\frac{\partial T}{\partial r}$ =0}

Heating of the steel shell is given by equation 1.7, where T_{shell}, is the temperature of the shell, with radius, R, and thermal diffusivity, α_{shell}. At addition time (t=0), the shell radius is equal to the alloy particle radius and the temperature of the shell is assumed to be the solidification temperature of the melt. As the shell radius increases, the shell surface temperature is assumed to be at the melt solidification temperature.

$$\frac{\partial T_{shell}}{\partial t} = \alpha_{shell} \left[\frac{\partial^2 T_{shell}}{\partial r^2} + \frac{2}{r} \frac{\partial T_{shell}}{\partial r} \right] \qquad R_o<r<R \tag{1.7}$$

At t =0 { R=R_o and T_{shell}= $T_{S,shell}$}; at r =R {T= $T_{S,shell}$}

The heat flux at the melt-composite particle interface (steel shell to melt) is specified in equation 1.8, which is only valid for small (30°C) superheats. k_{shell}, is the thermal conductivity of the shell, $\rho_{shell,}$ is density of the steel shell, $\Delta H_{f,shell}$, is the latent heat of fusion for the steel shell, h, is the heat transfer coefficient at the interface, and T_M, is the temperature of the melt.

$$k_{shell} \left[\frac{\partial T_{shell}}{\partial r} \right]_{r=R} = \rho_{shell} \Delta H_{f,shell} \frac{\partial R}{\partial t} + h(T_M - T_{shell}) \tag{1.8}$$

At t =0 {R =R_o}

Equation 1.9 shows the heat flux balance for the shell-alloy particle interface, where k_P is the thermal conductivity of the alloy particle, R_o-, is the initial alloy particle radius - inside of interface, and R_o+, is initial alloy particle radius - outside of interface. At the boundary the temperature of the particle and shell are the same.

$$k_P\left[\frac{\partial T_P}{\partial r}\right]_{r=Ro-} = k_{shell}\left[\frac{\partial T_{shell}}{\partial r}\right]_{r=Ro+} \quad (1.9)$$

$$T_{P,r=Ro}=T_{shell,r=Ro}$$

In dimensionless form, the above equations demonstrate that the ratios of k_P/k_{shell} and α_P/α_{shell} are significant characteristics for melting behavior of various alloys.[90] Under the stated conditions, this is applicable to elemental alloys and ferroalloys, but the authors only presented data for pure elemental additions to a pure iron bath.

1.6.1.2 Shell formation with liquid behind shell. Experimental results, with Class I alloys, indicate that melting does occur inside the shell, which requires the introduction of another equation with appropriate boundary conditions, as well as assumptions about the behavior of the liquid inside the shell, as depicted in Figure 1.7.

The formation of liquid under the steel shell is considered for two limiting cases, a) liquid does not circulate and b) liquid moves very rapidly, creating a homogenous temperature throughout the liquid. A stagnant liquid results in a conservative (low rate of heat transfer) estimate of shell existence time. A liquid with homogenous temperature would provide a greater rate of heat transfer and shorter shell existence time.

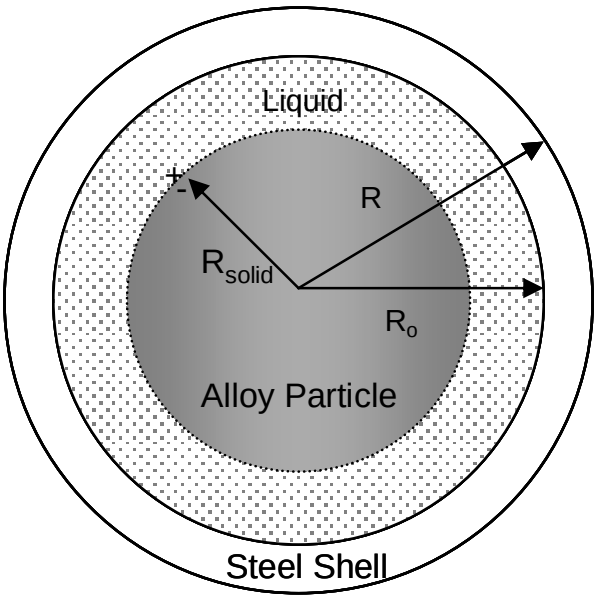

Figure 1.7. Schematic of Alloy Particle with Liquid under Steel Shell[91]

A third case could be encountered where eutectic formation occurs between the steel shell and the alloy liquid; this reaction could hasten both shell and alloy melting. Zhang and Oeters did not provide a mathematical treatment for eutectic formation.[92]

In the case where there is no liquid circulation, a heat balance at the melting alloy surface was used to formulate equation 1.10.[93] R_{solid}, is the radius of the solid alloy, which is also the position of the solid-liquid interface and R_{solid-} and R_{solid+} refer to inside and outside radius of the interface. $k_{p,l}$ and $k_{p,s}$ are the thermal conductivity of the liquid and solid alloy, ρ_p, is density of the alloy, and $\Delta H_{f,p,}$ is the latent heat of fusion for the alloy.

$$k_{P,l}\left.\frac{\partial T}{\partial r}\right|_{r=R_{solid+}} - k_{P,s}\left.\frac{\partial T}{\partial r}\right|_{r=R_{solid-}} = -\rho_P \Delta H_{f,P}\frac{dR_{solid}}{dt} \qquad (1.10)$$

1.6.1.3 Shell thickness. In order to determine the shell existence time, an estimation of the shell thickness is required. Shell thickness depends on two factors, first, the rate of heat transfer from the bath, where greater heat transfer due to higher superheat and/or melt agitation (increased slip velocity) reduces the thickness, and second, the ability of the alloy particle to act as a heat sink. A higher relative thermal conductivity, density, and heat capacity all support a thicker shell.

Zhang and Oeters performed numerical simulations to determine shell thickness for different conditions in pure iron. First, important physical property ratios, between the alloy and iron, were defined (equations 1.11, 1.12 and 1.13). These ratios determine the ability of the alloy to act as a heat sink.[94] Second, a range of heat transfer rates were chosen. Plots were then prepared to show interactions between the thermal conductivities, heat capacities and heat transfer coefficients.

Ratio of thermal conductivities - alloy to shell: $r_k = \frac{k_p}{k_{shell}}$ (1.11)

Ratio of thermal diffusivities - alloy to shell: $r_\alpha = \frac{\alpha_p}{\alpha_{shell}}$ (1.12)

Ratio of heat capacities - shell to alloy: $r_{cp} = \frac{C_{p,shell}\rho_{shell}}{C_{p,p}\rho_p}$ (1.13)

Thus $r_\alpha = r_k r_{cp}$

Changing the thermal conductivity ratio only weakly influenced the shell thickness. For example, a six fold increase in r_k (from 0.5 to 3) resulted in an increase in composite-particle radius of around five percent. However, doubling the heat capacity ratio, r_{Cp}, from 1 to 2 decreased the composite-particle radius by about eleven percent. Zhang and Oeters, without explanation, chose not to include the effect of r_α.

Decreasing the heat transfer coefficient from 6.28 to 1.8 W/cm^{2}K, increased the composite-particle radius by more than fourteen percent. Calculations for 1 cm alloy particles suggest that the average shell thickness is $0.2R_o$ with a maximum composite-particle radius of between 1.25 and 1.475 cm.[95]

In an unrelated experiment, Lee, Berg, and Jensen dipped 19.1 millimeter-diameter lollipops in an induction furnace with the power off (intervals between 2 and 9 seconds with 2 to 5 samples per alloy).[96] Table 1.6 shows the original radius, R_o, the calculated/observed maximum composite-particle radius, R_{max}, and a maximum radius when adjusted to 1 cm (by dividing by 0.955), R_n, for 75% ferrosilicon (75% FeSi), silicomanganese (SiMn), high-carbon ferromanganese (HCFeMn), and high-carbon ferrochromium (HCFeCr). Measured normalized radius ranged from 1.14 to 1.35 cm.

Table 1.6. Steel Shell Thickness Formed When Dipping Alloy-Spheres in Stagnant Steel Bath at 1873 K[99]

Ferroalloy	R_o – cm	R_{max} calculated (@ seconds)	R_{max} observed (@ seconds)	Normalized R_n; normalized to 1 cm R_o
75% FeSi	0.955	1.175 (4)	1.085 (4)	1.14
SiMn	0.955	1.135 (6)	1.135 (6)	1.19
HCFeMn	0.955	1.215 (6)	1.285 (6)	1.35
HCFeCr	0.955	1.235 (8)	1.255 (8)	1.31

The numerical model of Lee et al. for shell formation in a stagnant bath was run with a variety of values for the ferroalloy thermal conductivity.[97] The thermal conductivity value giving the best approximation of experimental results was then used. Lee explained that this was an apparent thermal conductivity (assumes no interfacial resistance), which differed from values published by Argyropoulus and Guthrie.[98]

The numerical model of Lee et al. also showed good agreement for HCFeMn and HCFeCr. However, SiMn and 75% ferrosilicon composite particles were smaller than predicted. Lee et al. offered two explanations for the lack of agreement. First, the steel bath was not entirely stagnant, increasing the rate of heat transfer (which should have affected all alloys). Second, there was an exothermic reaction between silicon and iron which reduced the shell thickness for 75%FeSi and SiMn.

1.6.1.4 Steel shell existence time Class I alloys. Because of the complexity and transient nature of the alloying process, determination of steel shell existence time, t_{shell}, requires an approximate numerical solution. In the case of small-size Class I alloys, a simpler approach can be used.

Zhang and Oeters calculations (melt temperature 1600°C and slip velocity 0.1 m/s) indicate that for large manganese particles (80 mm diameter) only 6% of the original volume is still solid when the shell melts and the remaining solid is pre-heated to the melting temperature of the alloy.[100] For 60 mm and smaller manganese particles, calculations indicated that the core was fully melted when the shell disappeared. Thus, the authors indicated that it was probably reasonable to assume that for smaller manganese particles the steel shell melt time represents the existence time of the solid. Similar calculations for nickel, which has a higher melting temperature and a larger heat capacity, yield similar results for 40 mm diameter particles.[101] Based on these calculations, a reasonable assumption for the steel shell-melting period, for low melting range alloys, like low-carbon ferromanganese (1200 to 1205°C), is to assume that the shell period is the melting time of the alloy particle.[102]

An approximation for the melting time of an alloy shell, t_{shell}, which also represents the particle dissolution time for Class I alloy is represented by equation 1.14, where $C_{P,P}$, is the heat capacity of the alloy particle, ρ_P, is the alloy density, R_o, is the original alloy particle radius, h, is the heat transfer coefficient, $T_{s,melt}$, is the solidification

of the melt, $T_{o,alloy}$, is the initial temperature of the alloy, and T_{melt}, is the steel bath temperature.[103] This approximation ignores the composite-particle radius and assumes that there is negligible resistance to heat flow through the steel shell.

$$t_{shell} = \frac{C_{P,P}\rho_P R_o}{\pi h}\left(\frac{T_{s,melt} - T_{o,alloy}}{T_{melt} - T_{s,melt}}\right) \tag{1.14}$$

The most commonly used correlation to determine the heat transfer coefficient for spherical particles in an agitated bath, was Whitaker's equation 1.15, (within 30%).[104] This coefficient depends on alloy particle diameter, d_{alloy}, melt thermal conductivity, k_{melt}, and the ratio of melt viscosity to viscosity at the alloy surface, $\frac{\mu}{\mu_s}$. Zhang and Oeters, [105] as well as, Aoki, et al.[106] set the viscosity-ratio term to one when calculating the heat transfer coefficient during modeling of alloy dissolution.

In general, for alloying in ladles, the Reynolds number (equation 1.5) is between 1,200 and 28,000 and for an alloy particle at 1536°C in a 1600°C steel melt, the approximate viscosity ratio and Prandtl number (Pr - equation 1.16) are 0.86 and 0.13 respectively, both of which are outside of the intended range for Whitaker's correlation.[107] Additionally, Poirier and Geiger indicate that this correlation should not be used for liquid metals.[108]

$$h = \frac{\left(2 + (0.4\,\mathrm{Re}^{\frac{1}{2}} + 0.06\,\mathrm{Re}^{\frac{2}{3}})\,\mathrm{Pr}^{0.4}(\frac{\mu}{\mu_s})^{\frac{1}{4}}\right)k_{melt}}{d_{alloy}} \tag{1.15}$$

Valid for: $0.71 < \mathrm{Pr} < 380$; $3.5 < \mathrm{Re} < 7.6\times10^4$; $1.0 < \frac{\mu}{\mu_s} < 3.2$

$$\mathrm{Pr} = \frac{C_{P,M}\mu}{k_M} \tag{1.16}$$

For the experimental research conducted with alloy cylinders hung in an induction furnace, an alternative to Whitaker's correlation is given by Churchill and Bernstein,

equation 1.17, which was tested with liquid sodium.[109] The heat transfer coefficient is obtained from the Nusselt number (Nu) in equation 1.18. This correlation is valid for cylinders at Reynolds numbers from 100 to 10,000,000 and products of Reynolds and Prandtl number greater than 0.2. A slight modification is suggested for Reynolds numbers between 20,000 and 400,000, where the exponent 5/8 in the far right term is replaced with ½.

$$Nu = 0.3 + \frac{0.62\,\mathrm{Re}^{1/2}\,\mathrm{Pr}^{1/3}}{\left[1+\left(\frac{0.4}{\mathrm{Pr}}\right)^{2/3}\right]^{3/4}}\left[1+\left(\frac{\mathrm{Re}}{2.82x10^{5}}\right)^{5/8}\right]^{4/5} \tag{1.17}$$

$$Nu = \frac{hd_{alloy}}{k_{melt}} \tag{1.18}$$

Argyropoulus and Guthrie modeled the melting time of spherical ferromanganese particles in stagnant steel baths at1570, 1600, and 1620°C.[110] Their results are shown in Figure 1.8. A stagnant bath should give the longest time required to melt a Class I alloy for a given alloy size and melt temperature. Nusselt number was calculated using a correlation from Churchill and Chu for natural convection, equation 1.19. Predicted times ranged from approximately 15 seconds for a 2 cm diameter particle at 1620°C to 1050 seconds for a 20 cm particle at 1570°C. For comparison, Zhang and Oeters computed times from 7 seconds (1600°C, 2 cm diameter, u=0.5 m/s) to slightly more than 200 seconds (1600°C, 10 cm diameter, u=0.05 m/s) for ferromanganese under stirred conditions.[111]

$$\sqrt{Nu} = 0.60 + \left[\frac{Ra}{\left(1+\left(\frac{0.559}{\mathrm{Pr}}\right)^{\frac{9}{16}}\right)^{\frac{16}{9}}}\right]^{\frac{1}{6}} \tag{1.19}$$

$$Ra = \frac{\rho\beta g C \Delta T d^3}{\mu k}$$

ρ – fluid density; β – fluid expansivity; g – acceleration due to gravity;
ΔT – temperature difference; d – particle diameter; μ – viscosity; k – fluid conductivity

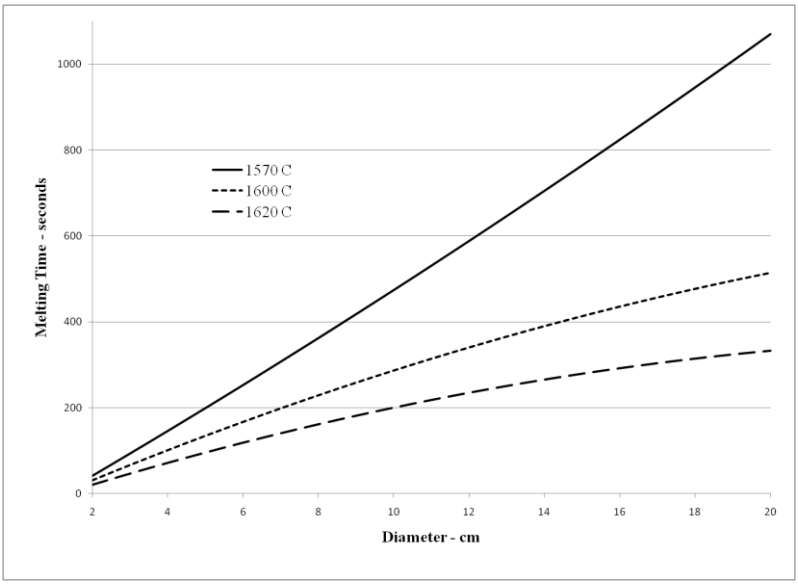

Figure 1.8. Predicted Melting Times for Spherical Ferromanganese Particles, 2 to 20 cm Diameter, in a Stagnant Steel Bath at Various Temperatures[112]

1.6.2. Dissolution of Class II Alloys. For alloys with a liquidus temperature higher than the steel melt, the particle core is still solid after the steel shell is melted away. In this case, alloy liquefaction is by dissolution, which requires a coupled heat and mass transfer model. Zhang and Oeters indicated that dissolution time, t_{disolv}, including the steel shell period through the disappearance of the alloy core, is expected to be proportional to the original alloy radius, R_o, raised to the power of 1.5, divided by the square root of the slip velocity, equation 1.20.[113]

$$t_{disolv} \propto \frac{R_o^{1.5}}{u^{0.5}} \qquad (1.20)$$

The heat transfer portion of the coupled model begins with a heat flow balance on the particle-melt interface, which yields equation 1.21. For an alloy particle of radius, *R*, the rate of dissolution is, - *dR/dt*, with ΔH_{sl} representing the sum of the latent heat of fusion for the alloy and the heat of mixing of the alloy in steel. In the event that the alloy particle was not heated to the melt temperature at the end of the shell period, the additional energy required could be added to the latent heat of fusion. Argyropoulos and Sismanis suggested equation 1.22 as a means of determining the heat of mixing, ΔH_{mix}, for niobium–iron mixtures; [114] This heat of mixing is added to latent heat of fusion to obtain ΔH_{sl} for ferroniobium. No other equations for heat of mixing were found in the literature reviewed. However, some values for heat of mixing are shown in Table 1.3.

$$\frac{dR}{dt} = -\frac{h}{C_{P,M}\rho_M}\ln\left(1+\frac{C_{P,M}\rho_M(T_M - T_{S,P})}{\rho_P \Delta H_{sl}}\right) \tag{1.21}$$

$$\Delta H_{mix} = X_{Fe}X_{Nb}(-37.756 - 48.869X_{Nb} + 26.351X_{Nb}^{2}) \tag{1.22}$$

The mass transfer portion of the coupled model, equation 1.23, is the result of a mass flow balance at the particle-melt interface.[115] Where c_P is the concentration of the alloying element in the particle, c_M is the alloying element concentration in the melt, and c_l is the concentration in the liquid interface. Equations 1.21 and 1.23 serve as the basis for the numerical Class II dissolution model (Section 2.6) used to model the present research.

$$\frac{dR}{dt} = -k\ln\left(\frac{c_P - c_M}{c_P - c_l}\right) \tag{1.23}$$

$\frac{dR}{dt}$ has to be the same for both heat and mass transfer, thus equations 1.21 and 1.23 may be combined, and through manipulation, yields equation 1.24 where α_M is the thermal diffusivity of the melt and D_a is the mass diffusivity of the alloying element in the melt. Zhang and Oeters suggest that resistance to mass transfer for typical Class II

alloys is about one hundred times greater than the resistance to heat transfer, so the process is mass diffusion limited.[116]

$$\ln\left(\frac{c_P - c_M}{c_P - c_l}\right) = \left(\frac{\alpha_M}{D_a}\right)^{2/3} \ln\left(1 + \frac{C_{P,M}\rho_M (T_M - T_{S,P})}{\rho_P \Delta H_{sl}}\right) \quad (1.24)$$

In order to solve equation 1.24, the relationship between interface concentration and temperature must be determined by fitting a curve to the liquidus line on the appropriate phase diagram.

Zhang and Oeters used equation 1.24 to numerically simulate alloying with pure chromium and 70% ferromolybdenum at 1600°C. Because there is little resistance to temperature flow, relative to mass flow, the calculated difference between interface and melt temperature was only 0.1 to 1.5 K for chromium and of a similar magnitude for 70% ferromolybdenum (FeMo). Shell melting time for chromium and 70% FeMo was calculated to be 20 to 100 seconds for particles with a radius less than 5 cm ($0.10 \leq u \leq 0.50$ m/s), while total dissolution ranged from less than 100 seconds (radius <0.5 cm) to 4400 seconds (radius 5 cm, u=10cm/s).[117] This is much longer than the melting time of ferromanganese calculated under the similar conditions (7 seconds to 200 seconds).[118]

Argyropoulos and Guthrie modeled spherical ferrochrome (50 to 58% Cr) and ferroniobium (66.5% Nb) dissolution.[119] Alloy particle size was 2 to 10 cm diameter for ferrochrome and 2 to 6 cm for ferroniobium. Ferrochrome was evaluated at three temperatures in a stagnant bath. From their plots (Figure 1.9), a 20 cm ferrochrome addition could be expected to dissolve in approximately 950 seconds at 1570 °C, 90 seconds at 1600 °C, or 50 seconds at 1620 °C, while a 10 cm addition would require 400, 50, and 25 seconds at the same temperatures. Argyropoulos and Guthrie indicated that any bath agitation would reduce assimilation time of ferrochrome. To illustrate this effect, they modeled ferroniobium at 1600°C with slip velocities of 0.3 and 0.9 m/s in addition to a stagnant bath (natural convection in Figure 1.10). Dissolution times with a slip velocity of 0.9 m/s ranged from 32 to 330 seconds. At 0.3 m/s the 2 cm particles

required almost 4 times longer to dissolve (120 seconds), while the largest particle required 570 seconds. Natural convection required 690 to 2120 seconds.

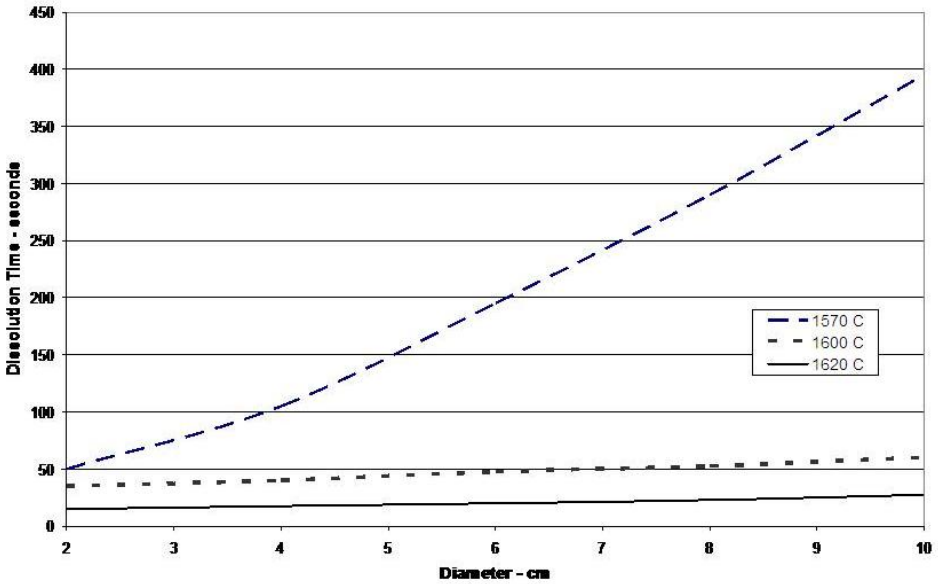

Figure 1.9. Dissolution (Melting) Time Prediction Curves for Spherical Ferrochrome Immersed in Stagnant Liquid Steel at 1570, 1600, and 1620°C[120]

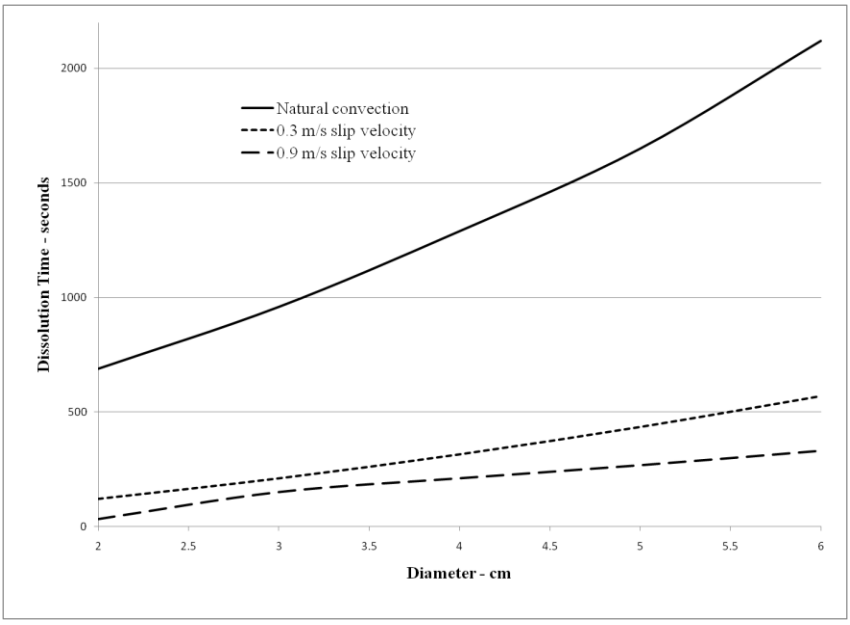

Figure 1.10. Predicted Dissolution Time Curves for Spherical Ferroniobium Immersed in Liquid Steel at 1600°C with Various Convection Conditions[121]

1.7. MIXING IN GAS STIRRED REACTORS

Two general approaches are taken in the literature for describing mixing in gas stirred reactors where homogenization occurs by either a combination of bulk-convective transport and eddy diffusion or is a combination of directed flow, turbulence and diffusion.[122] In either case, the Schmidt number (Sc), equation 1.25, can give an indication as to whether bulk convection (Sc>1) would dominate or eddy diffusion (Sc<1). The same is true for directed flow versus diffusion, where a Schmidt number greater than one favors direct flow over diffusion.

$$Sc = \frac{\nu}{D} \tag{1.25}$$

ν - kinematic viscosity; D – diffusion coefficient

1.8. MIXING MODELS

Mixing models in the literature generally fell into one of three groups. First, mixing time correlations based on gas flow rate or stirring power and a characteristic dimension of the mixing vessel. This group was primarily based on laboratory-scale water models, which were then scaled to full size using the concept of dynamic similarity. The second group utilized circulation, or a modified tank-in-series model (two-tank). The final group employed CFD models as discussed in the hydrodynamics section (Section 1.3). In all cases, mixing time was a key consideration.

1.8.1. Mixing Time. Mixing time is the time required for an alloy or tracer to reach a predetermined fraction or percentage of the expected fully mixed concentration, $C_{\infty,}$ throughout the entire vessel. Generally, most literature considers mixing to have occurred when the fraction is 90 to 99%, with 95% being typical.[123] In some cases, unhomogenized alloy-rich liquid circulates past the sampling position, resulting in measured concentrations exceeding 100% of C_{∞}, as shown in Figure 1.11. In some literature, the mixing time criterion was considered satisfied when the alloy concentration was between a lower and an upper limit. For example a bath would be considered 95% mixed when the measured value, C_{∞}, stayed ±5% of the target composition.[124]

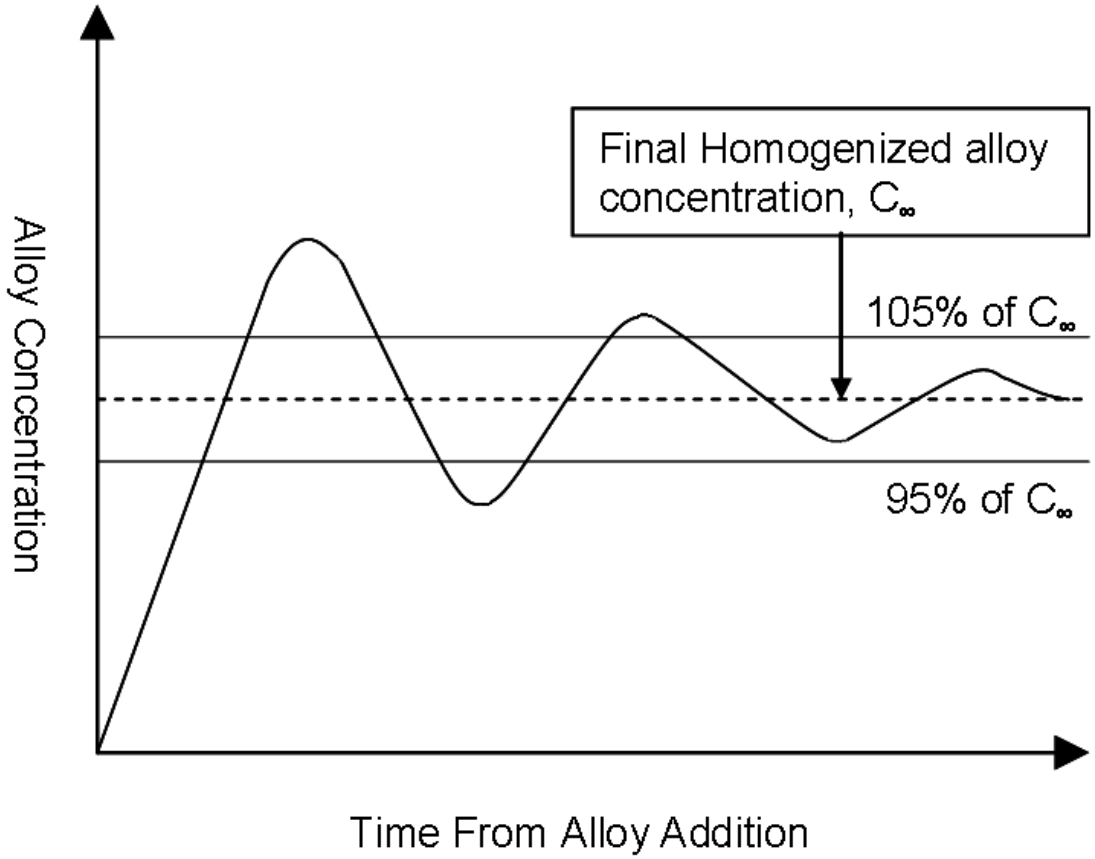

Figure 1.11. Schematic Plot of Alloy Concentration versus Time, Showing the Circulation of Alloy-Rich Liquid past Fixed Sampling Position[125]

Sampling position, relative to the alloy or tracer release location, plays a significant role in the observed mixing behavior. Mazumdar and Guthrie plotted the change in concentration of tracer (hydrochloric acid) versus time, Figure 1.12, for three sample positions in an air-stirred water model with tracer addition made to the eye (top of plume). At a location near the top surface, midway between ladle center and wall, the local concentration started at nearly two times the equilibrium bulk concentration, followed by a decaying rate to equilibrium. At a position below the first, the concentration started at 0.7 times final equilibrium, spiked to approximately 1.4 times C_∞, before falling to equilibrium, while at the bottom of the ladle near the center (but not in the plume) the concentration curve was nearly sigmoidal, starting at zero. Ninety-five percent mixing time for the first two positions was at approximately 52 seconds while the last position occurred at 90 seconds.[126]

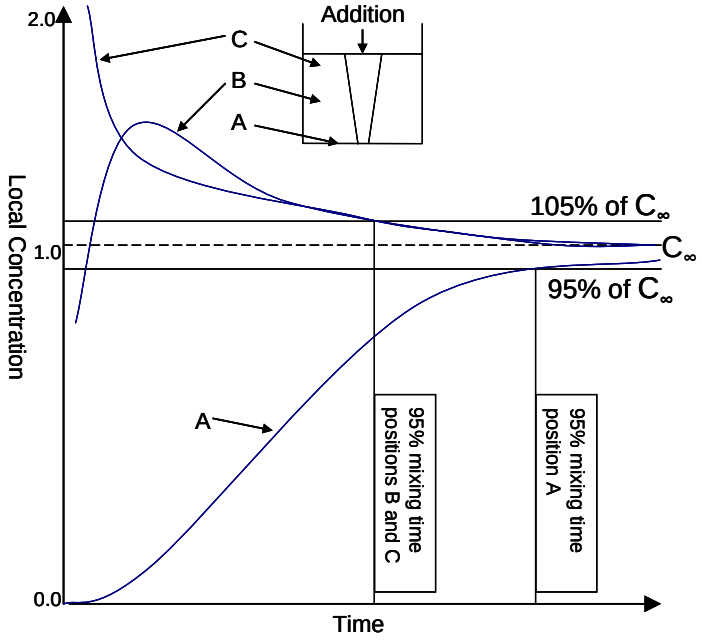

Figure 1.12. Plot of Local Tracer Concentration versus Time for Three Locations (A,B,C) in a Gas-Stirred Water Model, Showing Local Variation in Mixing Time[127]

Mietz and Oeters, found a similar effect, but in this case the tracer injection point was near the bottom corner of a water model.[128] Sampling adjacent to the tracer injection point resulted in a steeply rising concentration curve, which peaked at approximately nine times the final concentration, before decaying to the final concentration. Sampling near the surface, on the opposite side of the ladle from the addition point, resulted in a nearly sigmoidal curve (similar to curve A in Figure 1.12), while measuring at a position below the second sampling position resulted in a similarly-sigmoidal shaped curve, but the initial rise and final peak were shifted to a later time.

With a water model, the tracer can be released at a specified position, but in industrial practice, the alloys may either be added to the ladle prior to filling, into the tap stream at various times during the tap, into the slag eye above the argon stirring plume, or into the bath via wire injection. Initial alloy trajectory and steel currents within the melt result in the alloy being released at a variety of positions creating uncertainty in modeling. In modeling small scale gravimetric additions, the difference between hitting the rapid uprising plume or a dead zone in an area of the ladle is on the order of centimeters. Even in water models, Mandal et al., noted that sodium chloride tracer

additions penetrated to the bottom of their smallest vessel (D=0.30 m) but only to one quarter of the depth of a larger vessel (before the plume forced the tracer upward D=0.60m).[129]

1.8.2. Experimental Correlation Models. Many correlations have been proposed for mixing time as a function of gas injection rate or stirring power. Some models focused only on the rate of stirring energy input, while more refined models incorporated additional dimensional analysis.

1.8.2.1 Early stirring power - mixing time model. One of the earliest correlation models came from Naksnishi, Fujii, and Szekely, who proposed that at steady-state, the rate of eddy current dissipation must be equal to the rate of energy input per unit time. In this case, regardless of stirring method (e.g. gas injection, electromagnetic stirring, or mechanical agitation), mixing time should be a function of stirring power per unit of melt mass.[130] Naksnishi, Fujii, and Szekely fit a straight line through data points of complete mixing time versus stirring power, on a log-log plot, using data from industrial trials (from widely different vessels) and a water model. The resulting equation (1.26) indicates that mixing time, τ_{mix}, was proportional to stirring power, ε_M, to the minus 0.40 power.[131] Equation 1.26 implies that mixing time is independent of size, shape, and vessel configuration. Later work by Mazumdar and Guthrie, indicated that these assumptions are only valid if eddy diffusion dominates.[132]

$$\tau_{mix} = 800\,\dot{\varepsilon}_M^{-0.40} \tag{1.26}$$

1.8.2.2 Stirring power - mixing time model refined using dimensional analysis. Mazumdar and Guthrie performed dimensional analysis for mixing in gas stirred reactors.[133] Mixing time was considered to be a function of liquid depth, mean ladle radius, gravity, and gas flow rate. From this, three groups, dimensionless mixing time, geometric aspect ratio, and dimensionless gas flow rate were created and grouped. To determine the required exponents, Mazumdar and Guthrie examined plots of dimensionless mixing time versus dimensionless gas flow rate from six separate investigations using eight vessel configurations. They proposed that mixing time was

proportional to gas flow rate raised to the negative one-third power ($Q^{-0.33}$). In addition, mixing time decreased with increasing bath depth. These conclusions resulted in an expression for mixing time, shown as equation 1.27.[134]

$$\tau_m = \frac{C_1 R^{2.33}}{Q^{0.33} L} \tag{1.27}$$

τ_m – bulk mixing time; C_1 – empirical constant; L – liquid depth, m;
R – mean ladle radius, m; Q – gas flow rate, m^3/s

Mazumdar and Guthrie translated data from all of the investigations surveyed to a set of reference conditions to determine a numerical value for the empirical constant.[135] The reference condition consisted of five elements: (1) axisymmetric cylindrical vessels ($L/D \approx 1$), (2) 95 percent mixing, (3) negligible kinetic energy input to system, (4) specific potential energy input rate (~10^{-2} W/kg), (5) inertial-gravitational force to viscous force dominate flow regimes (Re on the order of 10^5). The authors then used best fit lines to estimate the constant as having a value of 29.8 $m^{2/3}/s^{4/3}$, which was in agreement with their earlier work.[136]

1.8.3. Scaling Mixing Models Using Dynamic Similarity. In order to translate experimental models to full-scale industrial applications, it is necessary to insure that there is geometric and dynamic similarity. Geometric similarity generally requires that the vessels have similar shapes and height (or liquid depth) to diameter ratios. Dynamic similarity (or dynamic similitude) occurs when key forces, often related through dimensionless numbers, are similar for both the model and the actual system. The two most important similarity criteria are Reynolds number and Froude number (the ratio of inertial force to buoyant force). Unfortunately, it is difficult to maintain both similarity criteria between vessels of greatly differing size. Mazumdar suggests that Froude number is more important than Reynolds number for bubble-stirred reactors.[137]

Mazumdar, Kim, and Guthrie used a theoretical basis to establish the conditions necessary for dynamic similarity. [138] Under Froude dominated flow conditions and with similar height to diameter ratios, a geometric factor, λ (equation 1.28), can be used to

adjust gas flow-rate in the model, using equation 1.29. Further, based on governing equations of material transport, the mixing time of a model, $\tau_{m,model}$, should be equal to mixing time in the full-scale vessel, $\tau_{m,fullscale}$, multiplied by the square root of λ (equation 1.30). The exponent, *n* in equation 1.29, was then determined to have a value of 2.5, by examining mixing time in four different water models.[139]

$$\lambda = \frac{L_{model}}{L_{fullscale}} \tag{1.28}$$

L_{model} – depth of liquid in model; $L_{fullscale}$ – depth of liquid in full scale vessel

$$Q_{model} = \lambda^n Q_{fullscale} \tag{1.29}$$

$$\tau_{m,model} = \lambda^{1/2} \tau_{m,fullscale} \tag{1.30}$$

1.8.3.1 Gas stirring circulation model. Gas-stirring creates circulating flow. Therefore a relatively simple approach to modeling is to consider the time to circulate the entire volume of liquid in the vessel, t_c, which is equal to the total volume of liquid divided by the circulatory volume flow, equation 1.31.

$$t_c = \frac{V_L}{\dot{V}_L} \tag{1.31}$$

V_L – volume of liquid in mixer; $\dot{V}_L$ – circulatory volume flow

With each circulation, mixing occurs, so the mixing time should be proportional to the circulation time ($t_{mix} \propto t_c$). Change in concentration with time for an alloy or tracer takes the form of equation 1.33, where the instantaneous concentration, *c(t)*, is related to the initial concentration, final concentration, c_∞, time, *t*, and a mixing time constant, *k*. Because mixing time is proportional to circulation time, a proportionality factor, *k'*, can be introduced to allow the combination of equation 1.31 and 1.32 to create an expression

for mixing time based on circulation time, equation 1.33.[140] α in equation 1.33, is the dimensionless concentration term on the left hand side of equation 1.32.

$$\frac{c(t)-c_{\infty}}{c_0-c_{\infty}} = \exp(-kt) \tag{1.32}$$

$$t_{mix} = k' t_c \ln\left(\frac{1}{\alpha}\right) \tag{1.33}$$

Increasing the stirring power increases the circulatory volume flow, which reduces the circulation time. Circulatory volume flow is proportional to the volume flow rate at the top of the bubble plume.[141]

Oeters used a combination of theoretical work, relative to recirculation, modified with empirical data to relate mixing time to stirring energy. [142] The theoretical portion centered on the volume flow-rate of steel at the top of the bubble plume, which is related to the expansion energy of the stirring gas. Empirical data for the contribution of gas kinetic energy to steel flow rate and the relationship between injected gas rate and width of the bubble plume were combined with the theoretical description to arrive at equation 1.34.[143] The dimensionless geometry factor, *F*, increases with the ratio of diameter to height, but Oeters did not elaborate on this factor.

$$t_{mix} = F\left[\frac{\left(\frac{m}{\rho_M}\right)^{\frac{2}{3}}}{\dot{\varepsilon}}\right]^{0.337} \tag{1.34}$$

m - mass of melt; ρ_M – melt density; $\dot{\varepsilon}$ - stirring power

1.8.3.2 Tank in series and two tank-model. Tank-in-series is a common approach to mixing in chemical and metallurgical engineering problems. In this

approach, the vessel is divided into a series of *N*, equal volume-ideally mixed tanks, with recirculation; flow from the final tank is fed back into the first tank. A tracer added to the first tank is immediately mixed and the volume of flow through the tank causes the tracer concentration to steadily decrease. Output from the first tank is mixed in the second and subsequent tanks. As the number of tanks approaches infinity, the tank in series model approaches ideal plug flow.

An ideal plug flow reactor would be a good approximation for a gas-stirred vessel where the circulation is well distributed throughout the entire volume of the melt. Unfortunately, gas stirring tends to create zones of low velocity, usually near the bottom of the vessel. These dead zones are especially prevalent in ladles with a single central porous plug. A modified tank-in-series model, the two-tank model, can be used to better describe mixing. In this case, the tanks are divided into two unequal volumes, V_1 for the dead zone and V_2 for the remainder of the vessel, as shown in Figure 1.13, with an exchange volume flow, $\dot{V}$.[144]

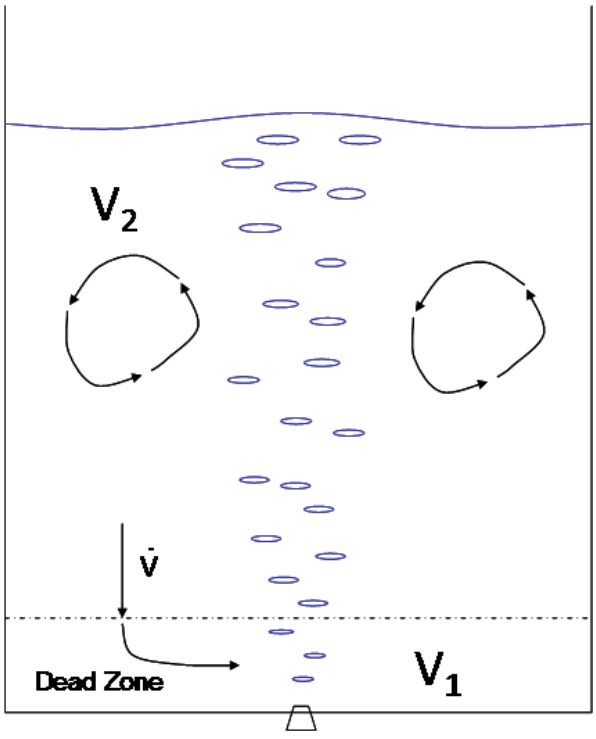

Figure 1.13. Schematic of a Two-Tank Model with Flow Showing Circulating Volume (V_2), Dead Zone (V_1), and Exchange Volume Flow($\dot{V}$)[145]

Both volumes are considered completely mixed with slow exchange between the two volumes. If c_0, c_1, c_2, and c_∞ are the initial alloy concentration, alloy concentration in V_1, alloy concentration in V_2, and final mixed concentration, then a mass balance results in equations 1.35 and 1.36. If at time zero, all alloy is concentrated in volume 1 ($c_1 = c_0$ and c_2=0), then the equations can be integrated to obtain expressions for dimensionless concentration, equations 1.37 and 1.38.[146]

$$\frac{dc_1}{dt} = -(c_1 - c_\infty)\dot{V}\left(\frac{1}{V_1} + \frac{1}{V_2}\right) \tag{1.35}$$

$$\frac{dc_2}{dt} = (c_0 - c_2)\dot{V}\left(\frac{1}{V_1} + \frac{1}{V_2}\right) \tag{1.36}$$

$$\frac{c_1}{c_\infty} = 1 + \frac{V_2}{V_1}\exp(-kt) \tag{1.37}$$

$$\frac{c_2}{c_\infty} = 1 - \exp(-kt) \tag{1.38}$$

Where $k = \dot{V}\left(\frac{1}{V_1} + \frac{1}{V_2}\right)$ in equations 1.37 and 1.38

This model contains two critical parameters, the exchange volume flow and the relative volume of the dead zone, both of which must be determined by measurement. Concentration prediction from this model provided a good match to water model data, however, at some sampling positions there was a lag due to tracer transport. Oeters found that this lag can be corrected by combining the two-tank model with a circulation model.[147]

The combined model continues to assume that the smaller volume (dead zone) is completely mixed, but the larger volume takes time to equalize by circulation and eddy diffusion. The larger volume is treated as a tank in series model, with a circulatory flow that moves through the series, while there is still an exchange volume between the dead

zone and the first tank in the series. This model, depicted in Figure 1.14, requires four parameters: circulatory volume flow, exchange volume flow, dead zone volume and number of tanks.[148]

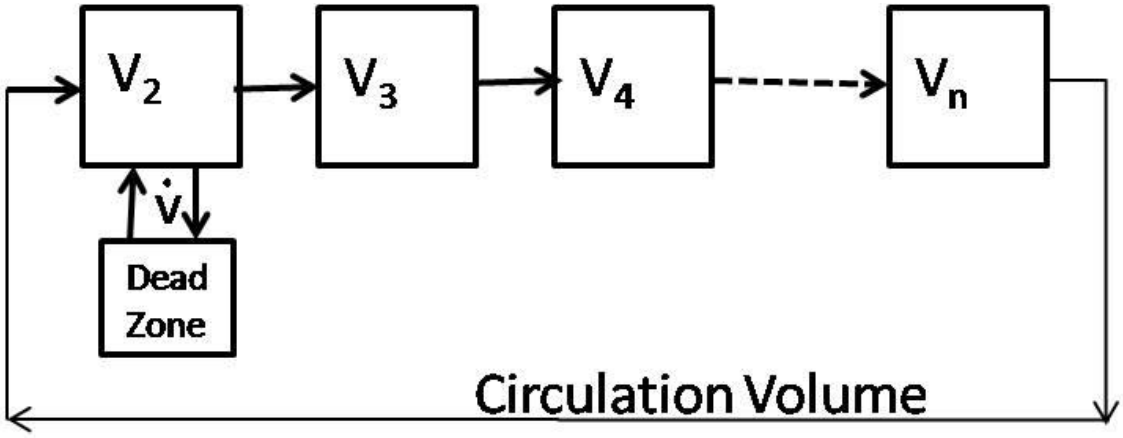

Figure 1.14. Schematic of Combined Two-Tank and Recirculation Model, Showing Tank in Series with Recirculation and Exchange between Dead Zone and Mixing Volume[149]

1.9. APPLICATION OF LITERATURE

The current research is focused on defining limitations and design parameters for making bulk alloy additions in the continuous steel making process. Defining the optimal alloy size reduces the prospect of producing unhomogenized steel, while potentially avoiding or reducing the cost of obtaining and handling fine alloys or wire.

A 45 kg capacity argon stirred ladle was used to study bulk alloy additions (Section 2.2). Experimental results from this ladle were modeled using a combination of CFD (Section 2.3) and a spreadsheet based numerical model (Section 2.4). Basic steel motion was established using CFD. The magnitude of the average steel velocity was then passed to a numerical model which calculated shell thickness, length of steel shell period, and alloy mixing/dissolution. This model uses heat and mass transfer described by Zhang and Oeters in Section 1.6, as well as a modified two tank model developed by Oeters (Section 1.8.3.2). [150,151,152]

In addition to Zhang and Oeters work, the drag coefficients of Aboutalebi and Khaki were utilized (Section 1.3.2) [153] and the assimilation routes of Argyropoulus and Guthrie (Section 1.5.4).[154] Routes 1 and 5 were assumed when preparing the numerical models used to describe the experimental work. Under some experimental conditions, for Class I alloys, the numerical steel-shell model predicts behavior resembling either route 3 or a cross between route 2 and 3, where the alloy partially melts, but a second steel shell does not form. Finally, Mazumdar and Guthries work on addition and sampling location (Section 1.8.1) was considered in modeling. [155]

2. EXPERIMENTAL AND MODELING PROCEDURES

2.1. INTRODUCTION

This research was undertaken to understand bulk alloying limits and parameters in ladle metallurgy and the continuous steelmaking process. The proposed continuous steelmaking design employs an argon stirred 27 ton finisher vessel for alloying.[156] To reduce the cost associated with pilot plant testing, an argon stirred laboratory scale ladle was constructed to evaluate alloy dissolution. This 45 kg capacity laboratory scale ladle, shown in Figure 2.1 is also applicable to general ladle metallurgy applications.

Figure 2.1. Experimental Ladle Filled with Liquid Steel (Crane Attached)

2.2. RESEARCH PLAN

Three Class I (low carbon ferromanganese, nickel and tin) and one Class II alloy (ferroniobium) were chosen to provide both elemental and ferroalloy additions with a range of melting temperatures. These alloys ranged in size from granular to 30 mm diameter with the size based on industrial use and literature recommendations. Based on the initial literature review, the Class I alloys were expected to follow route 1 (Figure 1.5) where the alloy would completely melt under the steel shell prior to the steel shell melting. Class II ferroniobium was expected follow route 5 where the alloy would be solid when the steel shell melted.

Dissolution was evaluated at two argon flow rates to provide industrially relevant stirring powers and for natural convection of Class I alloys to provide a baseline for comparison. Furnace tap temperatures of 1670 and 1710°C were chosen to provide adequate working time in the experimental ladle. Experimental conditions are shown in Table 2.1.

In the second phase of the research, modeling was performed to help understand experimental behavior. This modeling consisted of a CFD model of the ladle to provide steel velocities and a theoretically based spreadsheet model for steel shell period and either Class I alloy mixing or Class II alloy dissolution.

Table 2.1.Experimental Conditions

Experiment	Alloy	Alloy Form	Alloy Diameter - mm*	Nominal Tap Temperature -°C	Stirring Power
1	Ferromanganese	Lump	20	1670	High
2	Ferromanganese	Lump	30	1670	High
3	Ferromanganese	Lump	20	1670	Low
4	Ferromanganese	Lump	30	1670	Low
5	Ferromanganese	Lump	20	1670	None
6	Ferromanganese	Lump	20	1670	Low
7	Ferromanganese	Lump	20	1670	High
8	Ferromanganese	Lump	20	1670	None
9	Nickel	Pellet	13.5	1670	Low
10	Nickel	Pellet	13.5	1670	High
11	Nickel	Cathode	22/24	1670	Low
12	Nickel	Cathode	22/24	1670	High
13	Nickel	Pellet	13.5	1710	Low
14	Nickel	Pellet	13.5	1710	High
15	Nickel	Cathode	22/24	1710	Low
16	Nickel	Cathode	22/24	1710	High
17	Nickel	Cathode	22/24	1710	None
18	Tin	Liquid	-	1670	Low
19	Tin	Liquid	-	1670	Low
20	Tin	Liquid	-	1670	None
21	Tin	prism	20/24	1670	Low
22	Ferroniobium	Granular	-	1670	High
23	Ferroniobium	Granular	-	1670	High
24	Ferroniobium	Granular	-	1670	Low
25	Ferroniobium	Lump	10	1670	Low
26	Ferroniobium	Lump	10	1670	High
27	Ferroniobium	Lump	15	1670	Low
28	Ferroniobium	Lump	15	1670	High
29	Ferroniobium	Lump	20	1670	Low
30	Ferroniobium	Lump	20	1670	High

*mass equivalent sphere/surface area equivalent sphere

2.3. EXPERIMENTAL EQUIPMENT, MATERIALS AND PROCEDURE

The experimental equipment consisted of a 45 kg capacity argon stirred ladle. The ladle was filled with liquid steel from an induction furnace. An alloy addition was made and timed samples obtained for chemical analysis using an arc-spectrometer.

2.3.1. Ladle. The ladle vessel was composed of an inner refractory lining with sand backup and steel support structure (shown schematically in Figure 2.2). Sand provided physical support for the liner and protected the steel shell if the inner liner failed. The steel support structure consisted of a shell with provisions for crane attachment, tilt pouring, and gas system attachment.

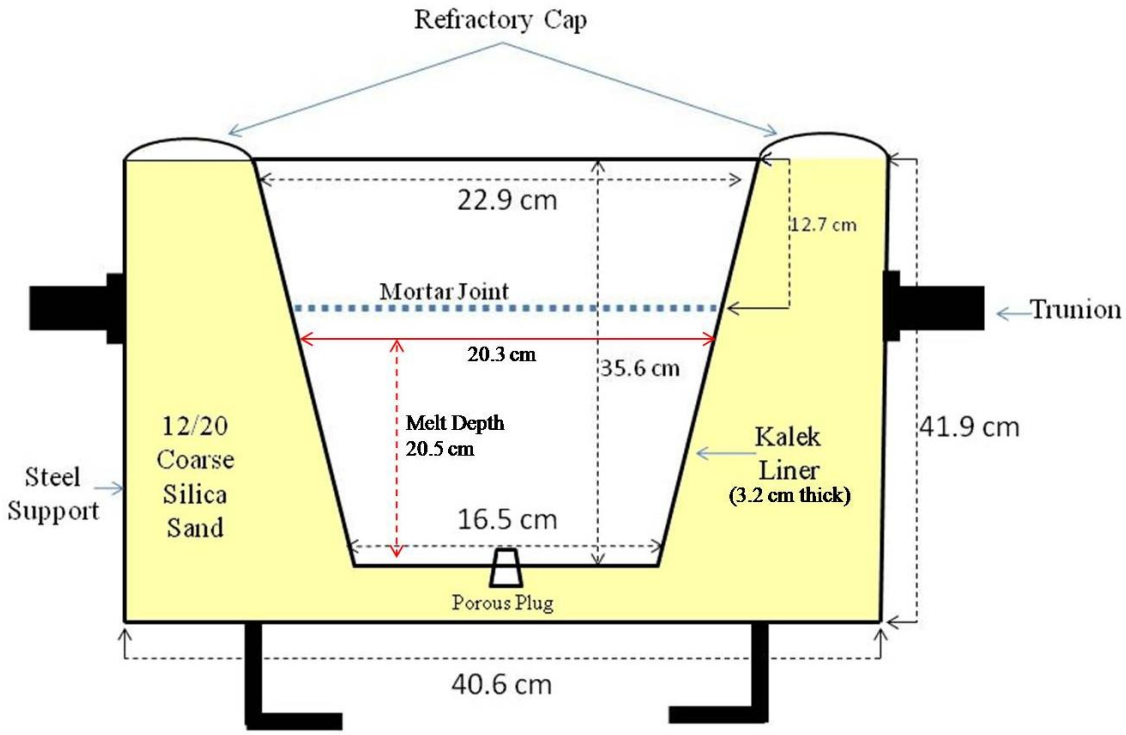

Figure 2.2. Kaltek Liner and Steel Shell Schematic

Foseco Kaltek liners (4000 series) were used for the ladle refractory. Kaltek liners are low density, insulating, and are made of magnesium oxide (>85%), magnesite, and an organic binder. Foseco supplied data is shown in Table 2.2. The total heat loss after one hour is based on a cold practice (no preheating the lining).

Table 2.2. Data for Kaltek Liners[157]

	Kaltek 4000 Series Liner
Composition (%): Al_2O_3 SiO_2 MgO	 - 5 >85
Bulk Density (g/cm^3)	1.3
Loss on Ignition at 1000°C (%)	7
Steady State Heat Loss at 700°C ($J/cm^2 \cdot minute$)	215
Total Heat Loss After 1 Hour (kJ/cm^2)	15.5

Two Kaltek liners were used to obtain the desired ladle geometry and freeboard. The upper 12.7 cm of a Kaltek S-150 was cemented to a smaller Kaltek S-100 liner using an alumina-graphite mortar (Morco Aligraph 2). This mortar was also applied as a protective coating on interior surfaces not in melt contact. The Kaltek liners were 3.2 cm thick. Overall inside depth was 35.6 cm with a tapered diameter of approximately 16.5 cm at the bottom, 20.3 cm at the melt surface and 22.9 cm at the top. A mortared Kaltek liner and steel shell are shown in Figure 2.3.

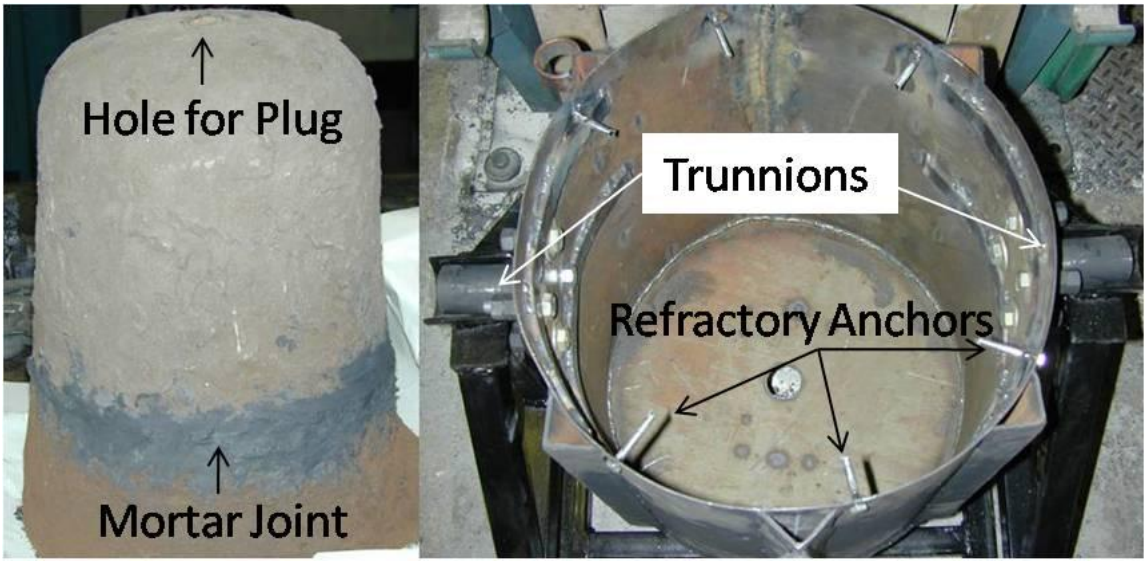

Figure 2.3. Inverted Kaltek Refractory Liner (left) and Steel Shell

A hole with three diameters was drilled on center in the Kaltek liner bottom to accept the porous plug assembly (Figure 2.4). The smallest diameter was on the melt side of the liner. This smallest diameter hole (approximately 2 cm) provided a tight seal between outlet end of the porous plug material and Kaltek liner. This hole was drilled slightly undersized and reamed to final dimension using the porous plug. The next diameter was designed to prevent the porous plug material from floating if it detached from the plug assembly. The largest diameter was drilled to match the steel pipe holding the porous plug material. This hole established the vertical position of the porous plug. Porous plug details are presented in Section 2.3.2.

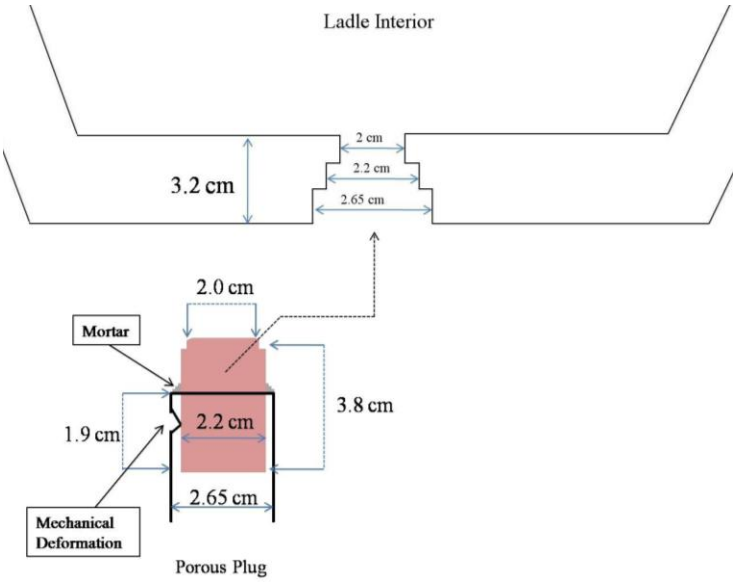

Figure 2.4. Schematic of Kaltek Liner Showing Porous Plug and Plug Interface Dimensions

Fairmount Minerals 12/20 course high-purity silica sand supported the Kaltek liner. Coarse sand was used to vent binder gases from the Kaltek liner through openings in a refractory cap. The sand also insulated the steel shell, which never exceeded 50°C during experiments. Morco phosphate-bonded magnesium oxide plastic refractory was used to construct the cap, which retained the Kaltek liner and sand when pouring. Bolts

anchored the refractory cap to the steel shell to retain the refractory cap when pouring. Sand and anchors (left) are shown in Figure 2.5, along with the vented refractory cap (right). Also visible is the mortar joint in the Kaltek liner and porous plug (right).

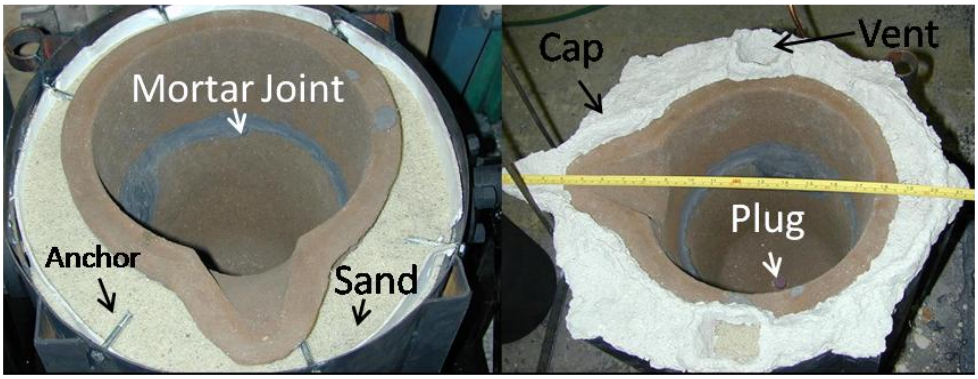

Figure 2.5. Experimental Ladle during Assembly, before Refractory Cap (left) and after (right) Refractory Cap (porous plug visible in right photograph)

The 1.5 mm thick steel ladle shell had a centered 5 cm hole in the bottom plate to accommodate the porous plug assembly. Trunnions on the side allowed the vessel to be moved by crane and tilted for pouring while suspended from the crane. The trunnions were made using 5 cm diameter pipe, 15 cm long, welded into socket weld flanges (15.25 cm outside diameter by 2 cm thick). L-shaped steel (8 cm x 8 cm x 30 cm) welded to the bottom plate supported the ladle during experiments.

2.3.2. Gas System. The porous plug was a key element in the gas system. A 3.8 cm thick slice was taken from the outlet end of an industrial porous plug. A diamond core drill was then used to make 2.2 cm diameter plugs for the ladle. This is shown schematically in Figure 2.6. Plug material was Harbison Walker Nargon A-94, which is 95% alumina.

Proof of concept testing was performed prior to use in liquid steel. A porous plug was evaluated in water to verify that discrete argon bubbles would form, as shown in Figure 2.7. A porous plug was then tested in the laboratory scale ladle using cast iron to insure that liquid metal would not leak around the plug assembly and that the heat loss

rate would not preclude experiments with steel. A porous plug failure with cast iron led to the stepped hole design for porous plug retention.

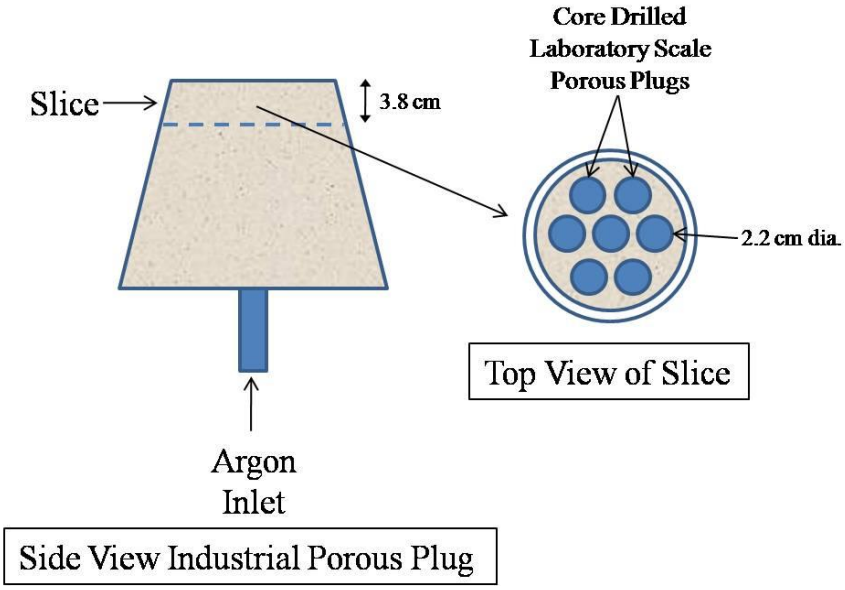

Figure 2.6. Schematic of Industrial Porous Plug Showing where the End Was Sliced and Core Drilled to Obtain Laboratory Scale Porous Plug Material

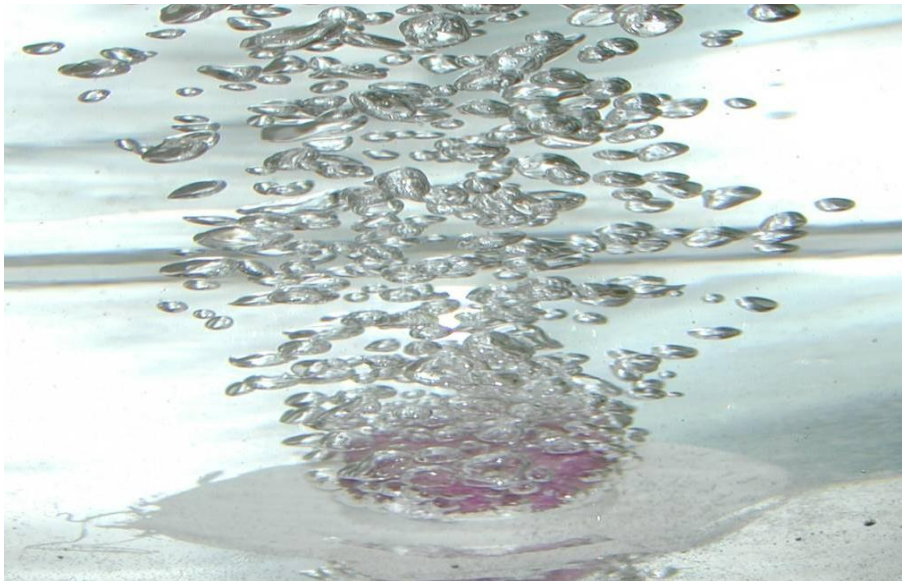

Figure 2.7. Argon Bubbles Rise from Core Drilled Porous Plug Being Tested in Water

The core-drilled plugs were inserted 1.9 cm into a steel pipe and retained by a combination of mortar and mechanical deformation of the pipe (shown in Figure 2.8 and schematically in Figure 2.4). Sand paper was used to slightly reduce the diameter of the porous plug to create a step. The porous plug – tubing assembly was retained in the bottom of the ladle using a steel plate driven over a machined steel wedge welded to the bottom of the vessel. Alumina-graphite mortar was used to seal the plug to the Kaltek liner and to resize the Kaltek liner hole after plug maintenance.

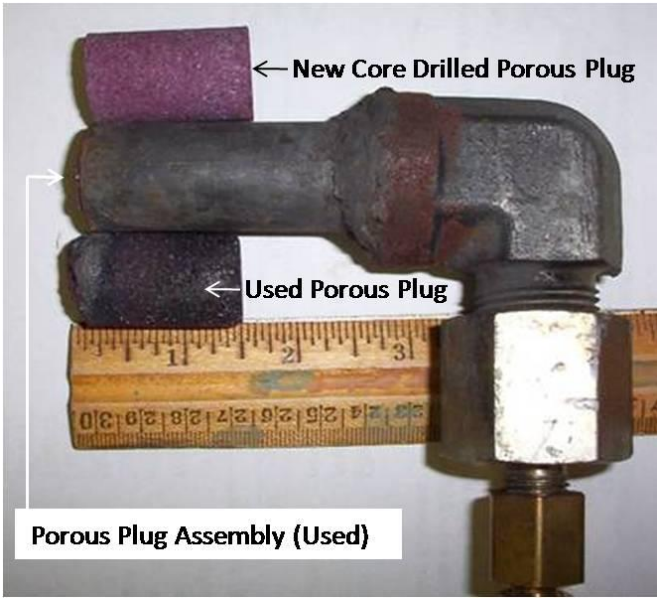

Figure 2.8. Photograph of Core Drilled Porous Plug Material (top) above a Used Porous Plug Assembly (middle) and Used Core Porous Plug Material (bottom)

The porous plug pipe was welded to a high-pressure steel elbow which was connected to 3/8" copper tubing (¼" ID by 3 feet long) using a high pressure-steel pipe fitting and a brass adapter.

The gas supply system is shown schematically in Figure 2.9. Argon was supplied from a cylinder using a standard duty-single stage regulator. Argon flowed from the regulator to a variable area flow meter (correlated rotameter). A needle valve at the inlet of the flow meter controlled the argon flow rate. A pressure meter at the flow meter outlet was used to correct the flow meter reading.

The regulator and flow meter were connected to the porous plug copper tubing using high temperature rubber hose (2-12.5’ hoses and adapters). The hoses allowed the ladle to be moved with gas flowing. The high temperature hose was chosen primarily because it would not sustain combustion after the ignition source was removed. This was tested when a porous plug failed while working with cast iron.

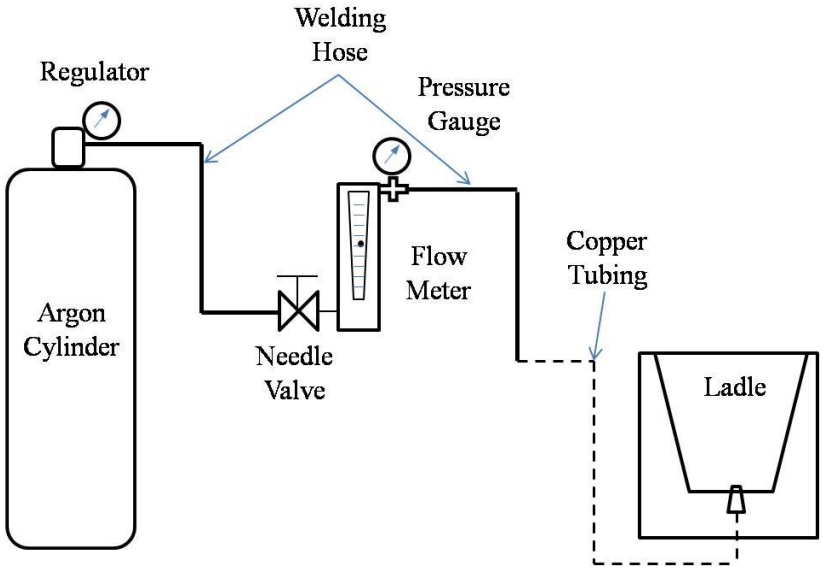

Figure 2.9. Gas System Schematic

2.3.3. Sampling System. A tundish vacuum sampler was chosen for taking samples. The sampler (Heraeus Electro-Nite Quik-Spec) consisted of a foil lined cardboard tube, wrapped in a 15 cm refractory sleeve, which contains a steel mold (see Figure 2.10); this mold filled through a quartz glass tube when vacuum was pulled on the cardboard tube. Vacuum was supplied by a Vaccon venturi which attached to the cardboard tube via a tapered fitting. The sampler was retained on the tapered fitting by friction.

Prior to use, the upper portion of each sample tube was numbered with a marker in two locations. Samples were obtained by squeezing a valve on the inlet of the venturi allowing compressed air to flow through the venturi. This was followed by lowering the

sample tube into the steel. After the mold was filled, the valve was released and the tube removed from the melt. The used tube was then pulled from the venturi assembly and quenched in water. A new tube was then attached and the process repeated until the prescribed number of samples was obtained. Occasionally, a sample was obtained too close to the bubble-plume, resulting in incomplete filling. The venturi assembly and an unused sample tube are shown in Figure 2.10. A sanded specimen taken from the steel mold is shown in Figure 2.11.

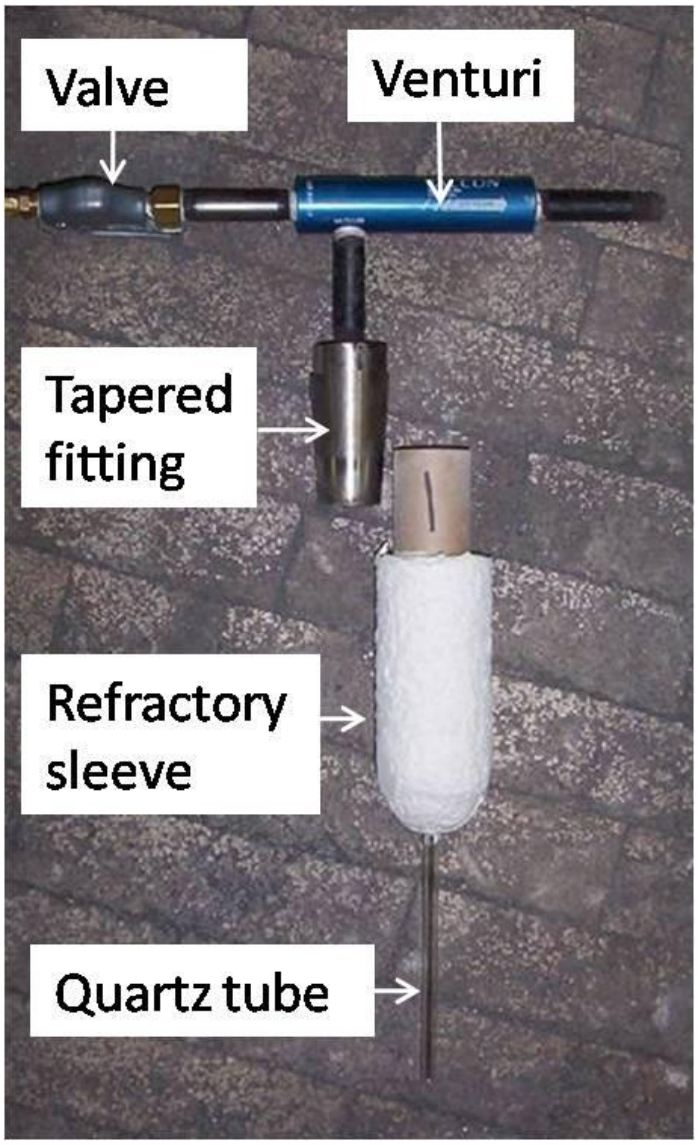

Figure 2.10. Photograph of Sampler Tube (bottom) and Venturi with Tapered Fitting Attached to a Hand Actuated Valve to Control Compressed Air

Figure 2.11. Photograph of a Steel Specimen Obtained from a Tundish Sampler after Sanding and Chemical Analysis Using an Arc-spectrometer (note: scale in inches)

2.3.4. Support Equipment. The primary support equipment consisted of an induction furnace for melting steel, an electric ladle preheater, and an arc-spectrometer for chemical analysis. Other equipment included a data acquisition system for recording temperature, video cameras, and an oxygen analyzer.

A 45 kilogram tilt pour induction furnace with a 75-kilowatt power supply (Inductotherm Power-Trak) was used to melt steel. Magnesium oxide based refractories were used for all heats.

Tapping losses from the induction furnace into a cold ladle averaged 50°C from 1670°C and 59°C from 1710°C. Most of this loss was due to radiation/convection from the pour stream with minor losses in heating the ladle refractory. A preheater was constructed to reduce refractory heating losses at tap and to reduce heat loss through the Kaltek liner during experiments. Tapping losses with the preheater averaged 44°C at 1670°C and 52°C at 1710°C.

The preheater (Figure 2.12) was constructed using a variable transformer (120-volt) connected to a silicon carbide heating element. The heating element extended through a lid into the ladle. The preheater lid was constructed from the inverted bottom section of a Kaltek S-150 (left over from ladle construction). Refractory blanket in the lid reduced heat loss. This blanket also protected preheater wiring from overheating. The preheater extended working time from approximately 90 seconds to 150 seconds (1670ºC tap and 10.2 liter per minute argon flow rate).

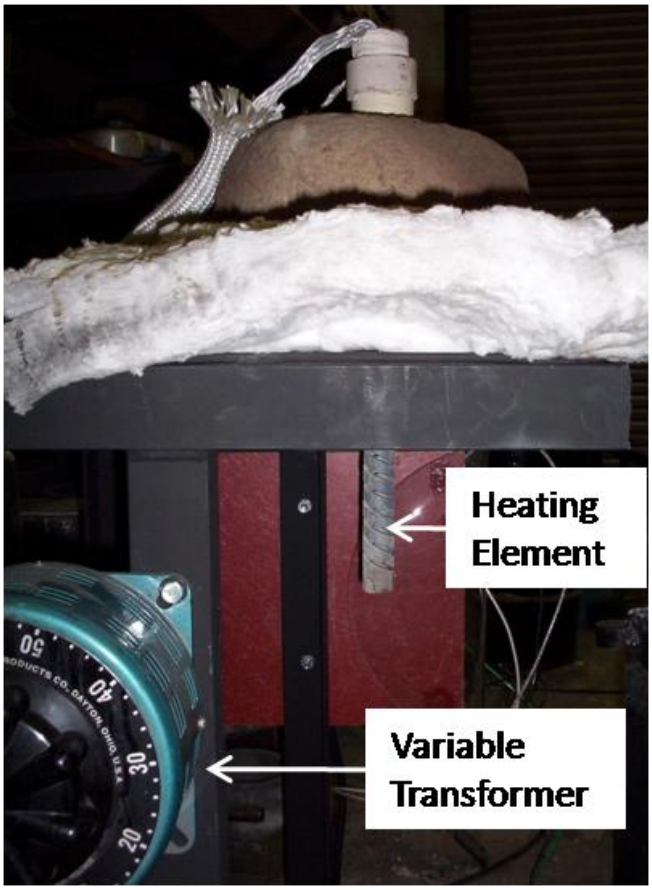

Figure 2.12. Photograph of Electric Ladle Preheater Showing the Variable Transformer and Silicon Carbide Heating Element. The Bottom of a Kaltek Liner (brown) can be seen on top of Refractory Blanket (white)

Temperature measurements of the Kaltek liner were taken with and without preheating. A type k thermocouple was attached to the sand side of the Kaltek liner and a type b to the melt side of the Kaltek liner. Temperature-time plots with and without preheat are shown in Figure 2.13 and Figure 2.14. The plot without preheat, starts at ~85°C because a 250 watt light bulb was used to keep the ladle refractory dry. Without preheat, the sand side surface reached 156°C during the 152 seconds that steel was in the ladle. With preheat the sand side surface (exterior) started at 695°C and the melt side (interior) at 560°C when steel is poured into the ladle. Sand side temperature continued to drop for 118 seconds reaching a minimum of 556°C. After 152 seconds the steel was poured out with the sand side of the Kaltek liner at 560°C. The type b thermocouple on the melt side failed in 14 seconds.

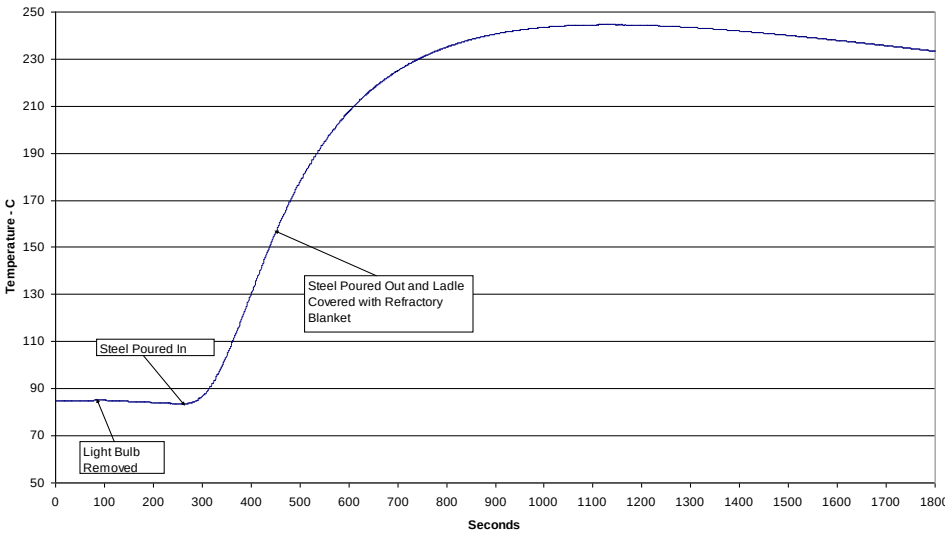

Figure 2.13. Surface Temperature of the Kaltek Ladle, Measured on the Sand Side Using a Type K Thermocouple, During an Experiment without Preheat

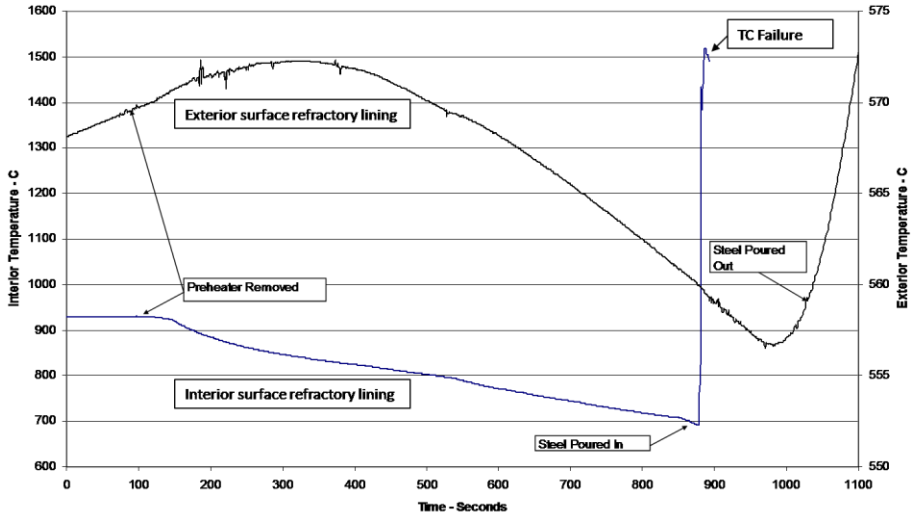

Figure 2.14. Surface Temperature of the Kaltek Ladle during a Preheated Experiment. (Exterior is the sand side of the Kaltek liner - right scale. Interior surface is the melt side - left scale)

Primary chemical analysis was obtained by arc-spectrometry, performed at two steel mills and at MS&T (SPECTRO Jr.). Specimens were removed from the steel mold and labeled. A belt sander with 80 grit aluminum oxide abrasive was used to create a flat surface on which to strike the arc. An arc-spectrometry specimen is shown in Figure 2.11.

2.3.5. Materials. Steel charge materials were selected to provide a consistent base chemistry. Low manganese pig iron was purchased for the steel so that manganese could be studied as an alloying addition. Alloying elements were chosen to represent Class I and II alloys.

Feed materials for the steel included AISI 1005 steel bars (Induction Iron HP-1001) as the primary iron source and high-purity pig iron (Sorelmetal) for carbon. Silicomanganese, low carbon ferromanganese and standard foundry grade 75% ferrosilicon were used to obtain the desired manganese and silicon levels. Base steel chemistry was nominally 0.4wt% Carbon, 0.25wt% silicon and 0.5wt% manganese, except for experiments which measured manganese dissolution. Early experiments were conducted with 0.8% carbon to extend working time. Table 2.3 gives the supplier certified chemical composition for the materials used.

Table 2.3. Composition of Charge Materials in Weight Percent.

	AISI 1005 Steel Bar	Silicomanganese	High Purity Pig Iron	75% Ferrosilicon	Low Carbon Ferromanganese
C	0.004	1.9	4.1		0.11
Mn	0.05	71.8	0.015 max		91.21
P	0.005	0.45	0.01	0.02	0.037
S	0.003	0.007	0.006	0.01	0.008
Si	0.01	16.3	0.2	74 to 79	0.30
Cu	0.01				
Cr	0.01				
Ni	0.01				
Mo	0.01				
Ti	0.005				
Al	0.002			1.5	
O	0.039				
N	0.004				
Sn	0.002				
Fe	Balance	Balance	Balance	Balance	Balance

Low carbon ferromanganese, nickel and tin were used for Class I alloys (see Section 1.4.3) and were expected to follow dissolution route 1 (Section 1.5.4). Tin was chosen to represent low melting additions like lead or sulfur. In addition, tin could be

added as a liquid, where calculations suggested that there would be no steel shell period. Ferroniobium was used for Class II dissolution experiments and was expected to follow dissolution route 5 (Section 1.5.4). These alloys are shown in Figure 2.15. Supplier provided chemistries for these alloys are provided in Table 2.4.

Figure 2.15. Photograph of Alloys Used to Study Dissolution. Left to Right: Low Carbon Ferromanganese Lump, Nickel Pellet, Nickel Cathode, Ferroniobium(granular above lump), Tin Cut from Triangular Bar (note: scale in centimeters)

Table 2.4. Chemical Composition (weight percent) of Dissolution Alloys

	Low Carbon Ferromanganese	Nickel Pellet	Nickel Cathode	Ferroniobium	Tin
C	0.11	<0.01		0.200 max	
Mn	91.21				
P	0.037			0.200 max	
S	0.008	<0.0002		0.100 max	
Si	0.30			3.00 max	
Nb				66.5 (63 min)	
Cu		<0.00005	<0.0035		
Sn					99.92
Ni		99.99	99.98		
Ti				Si+Al+Ti < 5.5	
Ta				0.20 max	
Al				2.00 max	
Fe	balance	<0.002	<0.0008	balance	

Low carbon ferromanganese spheroids were approximated by breaking larger alloy pieces using a hammer, followed by limited grinding to obtain a uniform shape. Sorting was then performed using gauges with nominal dimensions of 20 and 30 mm diameter.

Nickel, supplied as pellets and cathode pieces, was sorted to obtain spheres with an average diameter of 13.5 mm (standard deviation 1.4 mm) and rectangular pieces with average dimensions of 23.1 by 26.9 by 10.3mm (standard deviation of 1.3, 1.5, and 1.3 mm, respectively). No effort was made to shape the cathode pieces.

Tin was supplied as triangular bars. These bars were sectioned to provide pieces with a mass equivalent to a 20 mm sphere. Tin was primarily used as a liquid tracer addition.

Ferroniobium was obtained in both lump and granular form. Lumps were sorted and turned into approximate spheroids in the same manner as the low carbon ferromanganese. Granular material was sieved (see Table 2.5 for sieve analysis) and representative samples prepared for experiments.

Table 2.5. Granular Ferroniobium Size Fractions

Mesh Number	Mesh Number	Weight Percent
-6	+10	18.5%
-10	+16	16.8%
-16	+20	14.9%
-20	+30	13.7%
-30		36.1%

2.3.6. Experimental Procedure. Prior to beginning an experiment, AISI 1005 bars and Sorelmetal were cleaned by sand blasting and cut to proper size, the induction furnace and ladle refractory were inspected and patched as required, and the gas system (regulator set to 15 psig) and porous plug were inspected. All sample tubes were numbered and placed into a rack, in order.

Four hours prior to melting, the 250 watt heat lamps used to keep the ladle and furnace refractory from absorbing moisture were removed and the preheater was inserted

in the ladle. Power to the preheater was then ramped to approximately 1900 watts over a five minute period. Argon flow was then initiated at 0.5 liters per minute to prevent overheating the porous plug connections.

11.4 kg of sandblasted high-purity pig iron and 2 kg of AISI 1005 bars were charged into the magnesia crucible of the induction furnace. Argon purging of the furnace through an insulating lid was started. Furnace power was then ramped to 40 kilowatts over 25 minutes. Once the initial material melted, silicomanganese (except for ferromanganese experiments) was added. An AISI 1005 bar was then added and allowed to melt before adding another. This was repeated until all 34 kilograms of AISI 1005 were charged. Ferrosilicon and one fifth of the aluminum (specific melt chemistry is discussed with results) were added with the last AISI 1005 bar. The preheater was then removed and the experimental vessel moved into position in front of the induction furnace with a refractory blanket cover to retain heat.

Two temperatures were chosen to evaluate the influence of temperature on dissolution, 1670 and 1710ºC. When the melt reached 1630°C (1680ºC for a 1710ºC tap), gas flow to the porous plug was adjusted to the target flow rate and video recording was started. Stainless steel foil (≈75mm by 75 mm – grade 304) was placed over the porous plug and aluminum wrapped in steel shim stock (AISI 1008 – 0.025 mm thickness) placed on the foil. Upon reaching 1670°C (or 1710ºC), a sample was taken from the furnace and melt power turned off.

Liquid steel was tapped into the ladle, after which, the pressure at the outlet of the flow meter was recorded (on paper and continuously on video tape) for flow rate correction. Another sample was obtained (from ladle) while the ladle melt temperature and dissolved oxygen were measured. The alloy addition was made gravimetrically, on center from approximately 20.3 cm above the melt surface. Five samples were taken, midway between the wall and center (immediately adjacent to the plume) near the bottom of the ladle. Time for each sample was recorded using a stopwatch with video tape confirmation.

The first two samples after the alloy addition were taken as rapidly as possible (about one sample every six seconds). The final three samples were taken at specified times relative to tapping the furnace (60, 75, and 105 seconds). Ladle melt temperature

was measured as the last sample was taken. The vessel was raised and the steel poured into a graphite mold.

Variable area flow meters for gases are typically designed to operate at one atmosphere outlet pressure. The flow meter reading from the gas system needed to be corrected using equation 2.1, to obtain the actual flow rate for an experiment. [158] The compressible nature of argon would cause the gas system pressure to oscillate as the steel was transferred to the ladle. Precise adjustment of flow rate could not be made under these non-steady state conditions due to the short experimental window. Thus no effort was made to adjust the gas flow rate during the experiment. Instead, the pressure and flow meter readings were recorded for post experiment correction. This lack of adjustment resulted in some departure from the target argon flow rate. Actual low flow rate was between 3.9 and 5.1 lpm with 8.1 to 10.5 lpm for high flow rate.

$$Q_{corrected} = Q_{indicated}\sqrt{\frac{P_{measured}}{14.7\,psi}} \tag{2.1}$$

Q – flow rate; P – pressure, psi

2.4. CFD MODEL

Utilizing the experimental ladle geometry, a CFD model was created to evaluate steel flow patterns and velocity. Techniques described by Aoki, et al.[159] and Zhang, et al.[160] were used to calculate the interaction between the steel and a discrete argon phase. Fluent 6.2.16 software was used to solve the continuity equation 2.2 and momentum equation 2.3for the liquid steel phase and a discrete argon phase. [161]

$$\frac{\partial}{\partial t}\left(\alpha_{liquid}\rho_{liquid}\right) + \nabla\left(\alpha_{liquid}\rho_{liquid}\vec{u}_{liquid}\right) = 0 \tag{2.2}$$

α – volume fraction; ρ – density; $\vec{u}$ - velocity

$$\frac{\partial}{\partial t}\left(\alpha_{liquid}\rho_{liquid}\vec{u}_{liquid}\right) + \vec{u}_{liquid}\nabla\left(\alpha_{liquid}\rho_{liquid}\vec{u}_{liquid}\right) = -\nabla p + \nabla\left[\alpha_{liquid}\left(\mu_{liquid} + \mu_{turbulent}\right)\nabla\vec{u}_{liquid}\right] + F_b \tag{2.3}$$

p – pressure; μ – viscosity; F_b – bubble momentum exchange

The equations governing bubble motion used in the Euler-Lagrange calculation were summarized by Aoki, Thomas, Peaslee, and Peter.[162] First a particle Reynolds number is calculated (equation 2.4) using the melt density, particle diameter, slip velocity, and melt viscosity (the subscript 'p' refers to particle, which in this case is the discrete argon bubble). From the particle Reynolds number a coefficient of drag can be obtained using equation 2.5. The 'b' terms in the drag coefficient equation are parameters for non-spherical particles from a model by Haider and Levenspiel. Using the drag coefficient, a drag force may be calculated with equation 2.6. A force balance, equation 2.7, can then be performed to find the bubble acceleration. Finally, the bubble position, x_p, can be found using equation 2.8. The position equation contains a turbulent velocity term, which introduces a random element to the bubble motion.

$$\mathrm{Re}_p = \frac{\rho d_p \left| u - u_p \right|}{\mu} \tag{2.4}$$

ρ - fluid density; d_p - particle diameter; u - fluid velocity; u_p -particle velocity; μ -fluid viscosity

$$C_D = \frac{24}{\mathrm{Re}_p}(1 + b_1 \mathrm{Re}^{b_2}) + \frac{b_3 \mathrm{Re}_p}{b_4 + \mathrm{Re}_p} \tag{2.5}$$

$$F_D = \frac{18 \mu C_D \mathrm{Re}_p}{24 \rho_p d_p^2} \tag{2.6}$$

ρ_p - particle density

$$\frac{\partial u_p}{\partial t} = F_D (u - u_p) - \frac{(\rho - \rho_p)}{\rho_p} g \tag{2.7}$$

$$x_p = \int (u_p + u_p^{'}) dt \tag{2.8}$$

$u_p^{'}$ - fluctuation velocity due to turbulence

2.4.1. Model Geometry and Boundary Conditions. The 3D-model geometry was broken into five regions: interior, shell, bottom, porous plug and top. The interior was defined as the liquid steel domain. The shell and bottom were configured as standard

walls. Standard walls are impermeable (zero flux) and exhibit a no slip condition. The top was set as a pressure outlet and the porous plug as a velocity inlet (fixed velocity). Discrete argon particles (bubbles) were introduced through the porous plug. The meshed ladle is shown in Figure 2.16 and material properties are given in Table 2.6.

General settings included the pressure type solver, absolute velocity formation, and transient time. Gravity was set to 9.81 m/s^2 in the negative z-direction. The standard k-epsilon turbulence model was selected. Finally, the unsteady solver was set to 1st-order implicit.

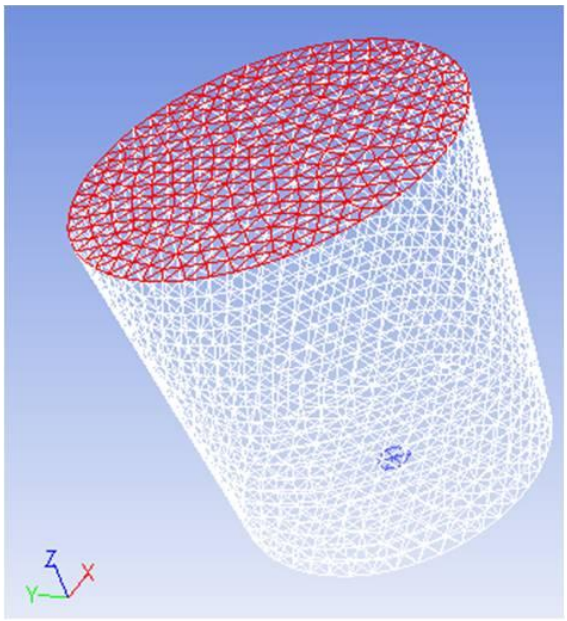

Figure 2.16. Meshed Ladle from the CFD Model Showing Top (red), Porous Plug (blue), Shell (white) and Bottom (white)

Table 2.6. Steel and Argon Properties for CFD Model at 1600°C

Property	Units	Steel	Argon
Density	kg/m^3	7000	1.6228
Specific Heat	j/kg·K	820	520.64
Thermal Conductivity	w/m·K	40.3	0.0158
Molecular Weight	kg/kg·mol	56	39.95
Viscosity	kg/m·s	0.0067	$2.125x10^{-5}$
Thermal Expansion Coefficient	1/K	0.00012	-

2.4.2. Model Operation. This model employed an alternating two-step process to reduce the required computational time. An Euler-Lagrange calculation for argon bubble motion was applied. This was followed by an Euler-Euler calculation for the liquid steel flow. The Euler-Euler model requires more computational resources than the Euler-Lagrange model. These Euler-Lagrange and Euler-Euler calculations were then repeated.

The molten steel was initially at rest at 1600°C. Argon bubbles were injected into the steel domain through the porous plug for one time step (0.001 seconds). The forces on the bubble were solved using the Fluent Lagrangian model (Euler-Lagrange) to obtain the bubble trajectory. The Lagrangian model treats the fluid phase as a continuum, solving the time-averaged Navier-Stokes equations. The dispersed phase is solved by tracking a large number of bubbles through the calculated flow field. The dispersed phase exchanges mass, momentum and energy with the continuum. Mass, momentum, and energy gained or lost by the bubbles is stored in the domain cells.[163]

In the next step, the liquid phase was set in motion for one time step. This motion is calculated from the momentum stored in the domain cells using an Euler-Euler approach. Each phase is assigned a volume fraction and the phases behave as interpenetrating continua. Conservation equations are required for each phase.[164]

After the liquid phase motion was calculated for a one time step, the bubble trajectory calculation was repeated for one time step. This alternating approach was continued until the average steel velocity approached steady state.

Steel velocities were generated for a range of argon flow rates. Example CFD model output showing velocity contours for a cross-section of the ladle is shown in Figure 2.17. The ladle average and maximum velocities were tabulated and plotted. Curves were fit through the plots to obtain equations for maximum steel velocity and average steel velocity versus argon flow rate, equations 2.9 and 2.10. These equations were then used in the spreadsheet based model.

$$V_{\max} = -0.0025Q^2 + 0.0675Q + 0.01 \tag{2.9}$$

$$V_{average} = -0.0004Q^2 + 0.0172Q - 0.0257 \tag{2.10}$$

V - velocity m/s; Q – argon flow rate liters per minute

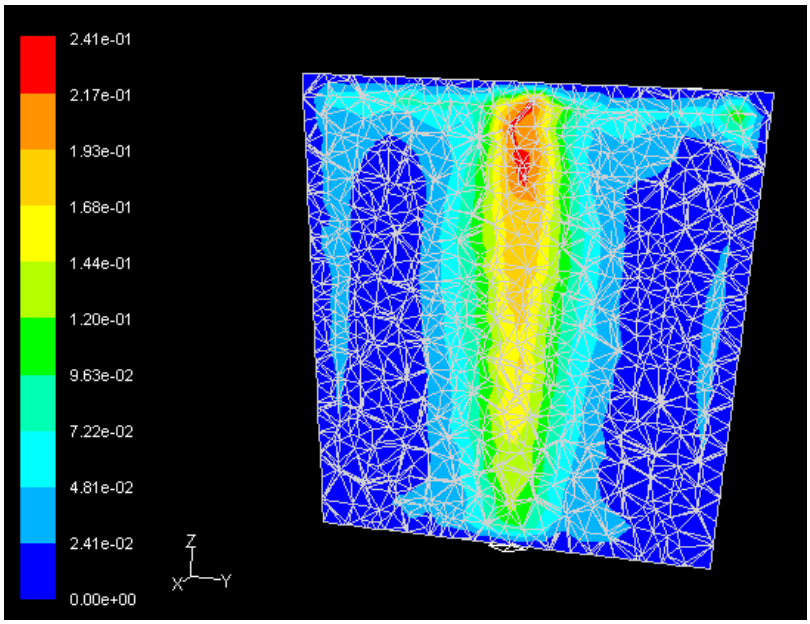

Figure 2.17. Cross Sectional View of the Ladle Showing Melt Velocity Contours (0 to 0.241 m/s) from the CFD Model for an Argon Flow Rate of 4 Liters per Minute

2.5. SPREADSHEET MODEL

A two-part numerical model was constructed in Microsoft Excel (97-2003 compatible) with Visual Basic for Applications (VBA) to simulate the dissolution of alloys. First, the steel shell formation and melting is computed and then alloy mixing (Class I alloys) or dissolution (Class II alloys) is evaluated.

The transition from the steel shell model to the mixing or dissolution model occurs when the steel shell has completely melted. Class I alloys were assumed to be fully melted at the end of the steel shell period. Class II alloys were assumed to be preheated to the solidification temperature of the steel bath at the end of the steel shell period. Source code for the spreadsheet model is included in Appendix A.

Model initialization required inputting alloy diameter, number of alloy particles, melt temperature, melt velocity (from CFD model), and material properties for the alloy and the steel melt. These properties include density, thermal conductivity, heat capacity, melting temperature, heat of fusion, and viscosity for the melt. These material properties are assumed to be constant. The material properties are then used to calculate thermal diffusivity, α (equation 2.11) and Prandtl number, Pr (equation 2.12), so that the steel shell can be modeled.

$$\alpha = \frac{k}{\rho C_p} \tag{2.11}$$

k – thermal conductivity; ρ – density; C_p – heat capacity

$$\mathrm{Pr} = \frac{\nu}{\alpha} \tag{2.12}$$

ν - kinematic viscosity

2.5.1. Steel Shell Model. The formation and melting of the steel shell on the alloy particle was numerically approximated using energy-balance calculations. By making simplifying assumptions, the heat transferred from the melt to the shell and shell to alloy particle can be readily estimated. The difference between the two results in the growth and then disappearance of the shell. Estimating heat transfer coefficient from melt to the shell requires knowledge of the alloy particle velocity relative to the steel bath.

After establishing initial conditions, like melt temperature and alloy particle entry velocity, the steel shell model follows a sequence of steps which can be broken into two categories, alloy particle velocity and position (Section 2.5.2) and heat transfer (Section 2.5.3). Additional details can be found in Table A.1 in Appendix.

2.5.2. Velocity and Position. Alloy particles could enter the melt near the rapidly rising plume or in a region near the wall where there is a downward velocity. The velocity-position portion of the spreadsheet model was setup to allow the evaluation of multiple scenarios, but had to be simplified to keep computational times reasonable (less than four hours). The primary simplification was to only evaluate melt velocity in the z-direction. The second significant simplification was that the melt velocity was constant. This z-directed velocity was the magnitude of the average melt velocity for the entire ladle. The average melt velocity was taken from the CFD model for the chosen argon flow rate.

Alloy particle entry into the steel bath is taken as time zero. Just prior to entry, the particles are assumed to be at room temperature (300 K) and be traveling with a velocity of 1.98 meters per second, due to falling from a height of 0.2 meters. The entry velocity assumes a perfectly smooth entry into the liquid steel and neglects air resistance during the fall. The initial temperature and velocity can be specified in the model.

Alloy velocity in the melt is determined by summing weight, buoyancy, and drag forces on the alloy particle at each time step. Newton's second law (F=m·a) can then be employed to determine change in velocity over the time interval. Knowing velocity, the particle position can be determined relative to the bottom of the ladle or the melt surface. The forces considered are weight, buoyancy, and drag, all of which vary as the steel shell grows and then melts.

Particle weight, F_w (equation 2.14), is the sum of the weight of the alloy particle and steel shell. Alloy particle mass does not change and is computed from the initial diameter and alloy density. Steel shell volume is computed at each step and then multiplied by density of solid steel to obtain mass. These masses are multiplied by the acceleration due to gravity to obtain weight.

Buoyancy, F_b, is computed by determining the volume of liquid being displaced by the composite alloy-steel shell particle; this volume is then multiplied by the liquid density and acceleration due to gravity (equation 2.15).

Finally, the velocity of the particle relative to the moving liquid is used to compute Reynolds number (equation 2.13), which is used to determine the coefficient of drag, C_d (see Section 1.2.2 and Table 2.1). The drag force (equation 2.16) is the product of a fluid kinetic energy term (½ ρv^2), the coefficient of drag, and the projected area of the particle ($A=\pi \cdot R^2$). With the slip velocity established, heat transfer can be evaluated.

$$\mathrm{Re} = \frac{vD}{\nu} \qquad (2.13)$$

D- particle diameter; v – velocity

$$F_w = (\frac{4}{3}\pi(R_{shell}^3 - R_{alloy}^3)\rho_{shell} + \frac{4}{3}\pi R_{alloy}^3 \rho_{alloy})g \qquad (2.14)$$

$$F_B = \frac{4}{3}\pi R^3 \rho_{melt} g \qquad (2.15)$$

$$F_d = \frac{1}{2}\rho_{melt} V^2 C_d A \qquad (2.16)$$

2.5.3. Heat Transfer. The initial shell layer is established by determining the difference between the heat transferred to the alloy particle surface and the heat conducted into the particle during the first time interval. The driving force for heat transfer is initially very large, as the alloy is at room temperature (300 K) and the melt is in excess 1873 K. After the first time interval, calculations are performed on the composite particle, assuming that the shell has negligible conduction resistance and is at the melt solidification temperature. For both cases, convective heat transfer and transient conduction must be evaluated.

2.5.3.1 Convection melt to shell. The convective portion of the model was developed using Nusselt number correlations used by Zhang and Oeters (equation 2.17) and Aoki, et al. (equation 2.18) in modeling alloy dissolution (see Section 1.5.1.4).[165, 166] Unfortunately, experimental conditions in the current study were outside the valid range for these correlations, so equation (2.19), suggested by Guthrie specifically for liquid metals was substituted into the model.[167] With the Nusselt number calculated, the convection coefficient, h, is determined using equation (2.20).

$$Nu = 0.62\,\mathrm{Re}^{1/2}\,\mathrm{Pr}^{1/3} \tag{2.17}$$

$$Nu = 2 + (0.4\,\mathrm{Re}^{\frac{1}{2}} + 0.06\,\mathrm{Re}^{\frac{2}{3}})\,\mathrm{Pr}^{0.4} \tag{2.18}$$

$$Nu = 2 + 0.38(\mathrm{Re}\cdot\mathrm{Pr})^{\frac{1}{2}} \tag{2.19}$$

$$h = \frac{Nu\,k_{melt}}{d_{alloy}} \tag{2.20}$$

The driving force for heat transfer is the temperature difference between melt and shell. The melt temperature cooled during the experiments and this is accounted for in the model using a curve fit of experimental data. Shell temperature is assumed to remain at the melt solidification temperature. This assumption is based on the need to reject/absorb the latent heat of fusion, as the shell solidifies or re-melts, prior to the shell changing temperature. The melt solidification temperature was on the order of 1750 K, but varied

slightly throughout the experimental campaign due to changes in the base steel chemistry, which is also accounted for in the model.

Using the heat transfer coefficient, temperature difference, and length of time step, the energy transferred within the period of interest can be assessed. The convective heat flux, Q'_{conv}, is calculated using equation 2.21, where A_{shell} is the surface area of the shell. The flux is multiplied by the time step to determine the energy transferred, which is a component of the energy balance on the shell. The other component requires evaluation of the transient conduction that occurs between the shell and alloy particle.

$$Q'_{conv} = hA_{shell}\Delta T \tag{2.21}$$

2.5.3.2 Transient conduction shell to alloy particle. Incropera and De Witt describe an exact solution for transient conduction within a sphere that is initially at a uniform temperature and then subjected to immersion in a fluid.[168] The solution requires solving an infinite series, equation 2.24, to obtain a dimensionless temperature, Θ^* and total energy transfer. Fourier number, Fo (equation 2.22), representing dimensionless time, and Biot number, Bi (equation 2.23), are integral to the solution. Typically, the characteristic length, L, for Biot number is one-third the radius of the sphere, but for this exact solution, L is just the radius.

$$Fo = \frac{\alpha t}{R^2} \tag{2.22}$$

$$Bi = \frac{hL}{k_{solid}} \tag{2.23}$$

Dimensionless temperature is defined in equation 2.25, where T_i is the initial temperature of the solid, T_∞ is the fluid (melt) temperature and T represents the temperature at a position and time of interest. ξ_n appears in both the infinite series

solution and equation 2.26, which is used to compute the coefficient C_n. ξ_n is obtained from the positive roots of equation 2.27. The final component of the infinite series equation is a dimensionless spatial coordinate, r^*, which is the position of interest, r, within the sphere, divided by the radius of the sphere (alloy particle). The dimensionless coordinate is illustrated in Figure 2.18. In the interest of reducing computing time an approximation for the infinite series was required.

$$\Theta^* = \sum_{n=1}^{\infty} C_n e^{-\xi_n^2 Fo} \left(\frac{1}{\xi_n r^*}\right) \sin(\xi_n r^*) \tag{2.24}$$

$$\Theta^* = \frac{T - T_\infty}{T_i - T_\infty} \tag{2.25}$$

$$C_n = \frac{4[\sin(\xi_n) - \xi_n \cos(\xi_n)]}{2\xi_n - \sin(2\xi_n)} \tag{2.26}$$

$$1 - \xi_n \cot \xi_n = Bi \tag{2.27}$$

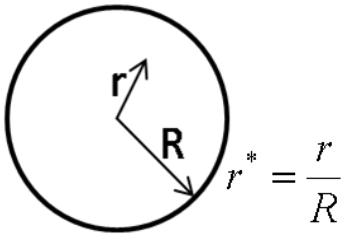

Figure 2.18. Illustration of Dimensionless Spatial Coordinate, r^*, Defined as the Quotient of Position, r, Divided by Original Radius, R.[169]

Heisler proposed a single term approximation for dimensionless temperature (equation 2.28), valid when $Fo \geq 0.2$. Heisler also approximated the temperature at the center of the alloy, Θ_o (corresponding to $r^* = 0$, equation 2.29, and fraction of heat transferred relative to total possible heat transfer, $\frac{Q}{Q_o}$ (equation 2.30).[170] The maximum energy that could be transferred, Q_o, is the energy required to raise the solid to its melting

temperature, at which time the solid would experience a thermal arrest, followed by melting.[171]

Unfortunately, under experimental conditions, the Fourier number can take several seconds to reach the required 0.2 value. Using several terms to approximate the series leads to an improvement in accuracy when Fo < 0.2. For example, with a Fourier number of 0.1 and a Biot number of 3.5, Heisler's one term solution would result in a surface temperature that is 24.5% less than a five term approximation.

In order to determine an appropriate number of terms for the approximation, $\frac{Q}{Q_o}$ was evaluated, until the result did not vary by more than 0.010%, for thirty combinations of Fourier and Biot numbers. Based on this, an algorithm was written into the model to use *n* terms to approximate the infinite series, where *n* is calculated by rounding equation 2.31 to the nearest integer.

At each time step, the model calls a VBA program to compute positive roots of equation 2.27, using the already calculated Biot number. The program utilizes an initial guess for ξ_n, and then iterates until the result is within ±0.001 of the Biot number, at which time ξ_n is stored in an array and the next root is found using an initial guess of ξ_n +3. If convergence does not occur within 2.5 million iterations, the program will store the final guess for ξ_n and then proceed to the next root or until n roots have been found. Using the array values for ξ_n, equations 2.32, 2.33, and 2.34 are used to compute dimensionless temperatures and fraction of energy transferred.[172] These values are then sent back to the spreadsheet.

$$\Theta^* = C_1 e^{(-\xi_1^2 Fo)} \left(\frac{1}{\xi_1 r^*}\right) \sin(\xi_1 r^*) \tag{2.28}$$

$$\Theta_o^* = C_1 e^{(-\xi_1^2 Fo)} \tag{2.29}$$

$$\frac{Q}{Q_o} = 1 - \frac{3\Theta^*}{\xi_1^3} \left[\sin(\xi_1) - \xi_1 \cos(\xi_1)\right] \tag{2.30}$$

$$n = -2.3\ln(Fo) + 4 \tag{2.31}$$

$$\Theta^* = \sum_{n=1}^{x} C_n e^{-\xi_n^2 Fo} \left(\frac{1}{\xi_n r^*}\right) \sin(\xi_n r^*) \tag{2.32}$$

$$\Theta_o^* = \sum_{n=1}^{x} C_n e^{-\xi_n^2 Fo} \tag{2.33}$$

$$\frac{Q}{Q_o} = 1 - \sum_{n=1}^{x} \frac{3\Theta^*}{\xi_n^3} \left[\sin(\xi_n) - \xi_n \cos(\xi_n)\right] \tag{2.34}$$

2.5.3.3 Shell growth and melting. Having computed the energy transfer from the melt (convection) and conduction to the alloy particle, an energy balance can be applied to determine how much steel would be added to or removed from the steel shell within the time step. In this calculation, the heat conducted into the alloy is subtracted from the heat transferred by convection to the alloy to determine the net heat transferred, Q_{net}. Utilizing the latent heat of fusion for the melt, ΔH_f, the specific heat for the melt, Cp, and the temperature difference between the melt and shell (which is assumed to be the solidification temperature of the melt), equation 2.35 is used to determine the change in mass. The total mass of the shell is then converted to a volume, which is added to the volume of the original alloy. Neglecting thermal expansion and assuming a spherical composite particle, the radius is computed using equation 2.36. The steel shell model moves to the mixing model when the steel shell has disappeared ($R=R_o$).

$$\text{Mass change} = \frac{Q_{net}}{\Delta H_f + Cp(T_{melt} - T_{solidificaiton})} \tag{2.35}$$

$$R = \left(\frac{3V}{4\pi}\right)^{\frac{1}{3}} \tag{2.36}$$

2.5.4. Steel Shell Model Performance. The steel shell model calculation rate is Fourier number dependent, requiring longer calculation times for low Fourier numbers. For example, with a time step of 0.01 seconds, the initial calculation (Fo=0.00252) requires 68 seconds, while the one hundredth time step (Fo=0.2230) of the same model

required 20 seconds (Intel Xeon 3.0 GHz, Windows XP, Excel 2007 in 97-2003 compatibility mode). For the same model run with a smaller time step, 0.001 seconds, the three thousandth calculation (Fo=0.6757) requires 15 seconds. Properties listed in Table 2.7 were used to generate Figure 2.19, which shows composite particle diameter versus time (20 mm nickel particle) from the steel shell model. At around 3 seconds, when the shell has melted, there is almost no discernible difference between a time step of 0.01 and 0.001 seconds, but the 0.01 step required about one hour and 40 minutes to compute, while the 0.001 step required around 12 hours. Large time increments produce unrealistic output, as illustrated by the 0.05 second time step line in Figure 2.19.

Table 2.7. Shell Model Melt Properties Used to Generate Figure 2.19.

T_{Melt}	1600°C	K_{melt} [173]	40.3 W/m·K
$T_{solidification}$	1535°C	ρ_{Melt} [174]	7020 kg/m^3
$C_{p,melt}$ [15]	820 J/kg·K	$\rho_{solid,melt}$ [176]	7257 kg/m^3
ν_{melt} [177]	8.57X10^{-7} m^2/s	$\Delta H_{f,melt}$ [178]	277 kJ/kg
α_{melt}	7.0X10^{-6} m^2/s		

The size of the initial shell is affected by the time step, which is demonstrated by the plot in the upper corner of Figure 2.19. Shorter increments result in a larger composite particle, but this has little impact on the overall shell melting time. The model does not account for the kinetics of shell formation, which results in the model overestimating the initial size and growth rate of the shell.

When modeling actual experiments, a variable time step was employed, with a small increment initially (0.001 seconds), followed by a larger time step (0.01 seconds beginning at 0.1 seconds) to provide a balance between resolution and computing time.

The mixing model for Class I alloys was developed assuming that the alloy particle would be entirely melted when the steel shell disappeared (Route 1 in Figure 1.5, Section 1.5.4, p. 19) This is not the case for the example plotted in Figure 2.19. When the steel shell melts at 3.01 seconds, the shell model predicts that the center of the alloy particle would be at the alloy melting temperature but would not have received enough

heat to melt (Route 2 in Figure 1.5). The remaining solid is treated as liquid in the Class I mixing model. Class II alloys should not need a mixing model, where diffusion dominates mixing, however the numerical mixing model described in the next section, could be applied if the reactor is not well mixed.

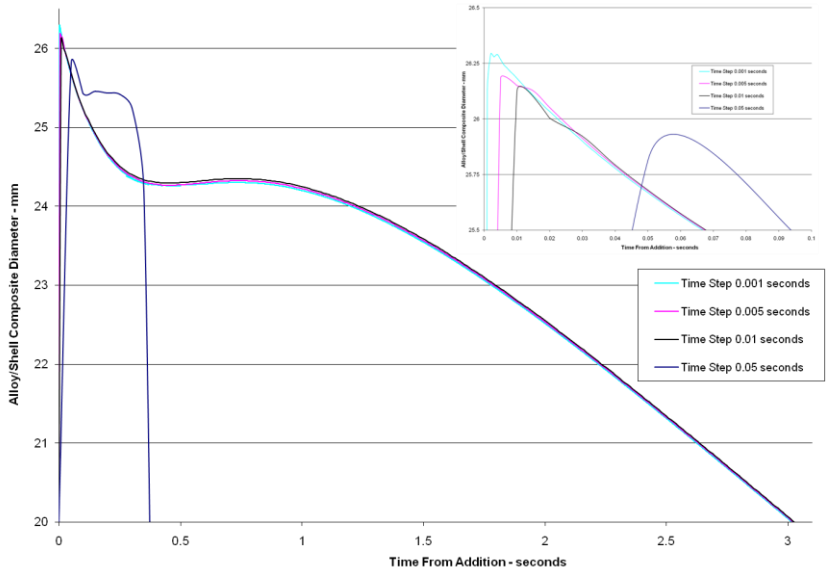

Figure 2.19. Steel Shell Model Output for a 20mm Diameter Nickel Alloy Particle Showing the Effect of Time Step on the Maximum Computed Alloy/Shell Composite Particle Diameter and Time to Reach Original Alloy Particle Diameter. (Inset at top right of figure magnifies difference in maximum diameter)

2.6. MIXING MODEL

The two tank model equations developed by Oeters (Section 1.7.3.2), were adapted to function within the spreadsheet model. An additional tank in series was added to better match experimental results. This three tank model is, illustrated in Figure 2.20.[179] After the steel shell melts, alloy mass (solute) associated with the alloy particles is entered into the alloy tank, with volume, V_a. The alloy tank exchanges mass with the dead zone, with a volume exchange rate of $\dot{V}_a$. The dead zone represents the recirculating alloy rich region seen in the experimental work and described by Mazumdar and Guthrie (Section 1.7.1.1).[180] The dead zone has a volume, V_1.

The mixing volume, V_2, then exchanges mass with the dead zone at a rate, $\dot{V}$, until equilibrium is achieved. Each zone is considered to be well mixed. Oeters cites several references where this method was successfully applied to modeling steel ladles and torpedo ladles.

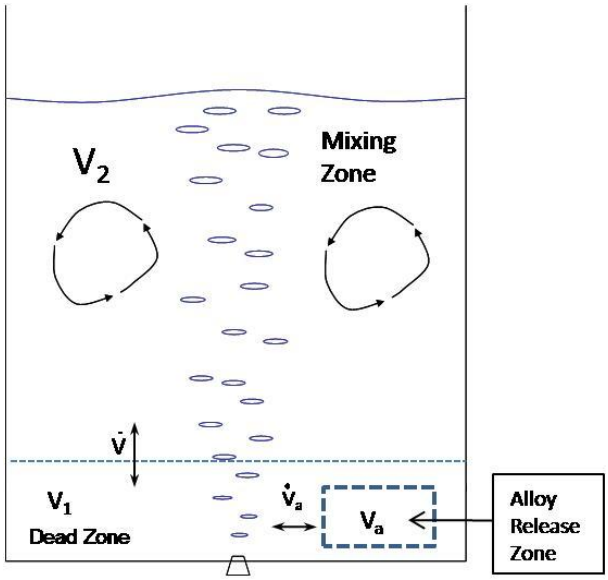

Figure 2.20. Illustration of Three Tank Model Showing Alloy Zone, Dead Zone, and Mixing Zone. The Alloy Zone Exchanges Solute with Dead Zone Which then Exchanges Solute with the Mixing Zone. (The dead zone is the alloy rich region which circulates through the ladle prior to alloy homogenization)[181]

In the simplest case, two tanks and a negligible initial alloy concentration, the alloy concentration in V_1 and V_2 are given by the analytical solutions in equations 2.37 and 2.38, where C_1 and C_2 are the concentrations in the dead zone and mixing zone.[182] In both equations, C_∞, represents the final alloy composition after mixing. Prior to output, the volume concentration is converted to weight percent to match the data collected in the experimental program.

$$C_1 = [1 + \frac{V_2}{V_1} e^{(-\dot{V}(\frac{1}{V_1}+\frac{1}{V_2})t)}]C_\infty \quad (2.37)$$

$$C_2 = [1 - e^{(-\dot{V}(\frac{1}{V_1}+\frac{1}{V_2})t)}]C_\infty \quad (2.38)$$

For more complicated conditions, like, alloy particles melting (or dissolving) at different times due to variation in local steel velocity, several steel shell models may be run in parallel and the results manually passed to a numerical mixing model (adding alloy mass to V_1 at the appropriate time step and modifying C_∞ accordingly), so that new equations do not have to be derived for every case. This variable shell period condition is more likely in the experimental ladle, where the low velocity at the wall is only 8 to 10 centimeters from the high velocity region near the plume. The other complication likely to arise is a non-negligible initial alloy concentration, which is easily accommodated using a numerical version of the analytical model.

Prior to running either an analytical or numerical version of the model, initial conditions have to be established; this includes total volume of steel melt, fraction of the total that represents the alloy zone and dead zone, along with the volume exchange rates. The volume exchange rates should be proportional to the argon flow rate, while the dead zone fraction should be inversely related to the argon flow rate. Oeters found that in gas stirred water models the exchange with the dead zone is slow and hardly affected by stirring intensity.[183]

The mixing models follow these steps:

1) Input mass of steel melt, alloy, and their densities
2) Compute total volume based on mass and density
3) Input percent of alloy element in alloy particle (example: 91.2wt% for ferromanganese)
4) Calculate mass of alloy element added to alloy zone (dead zone for two-tank)
5) Input dead zone and alloy zone volume fractions and volume exchange rates $\dot{V}_a$, $\dot{V}$
6) Compute volume of alloy zone (V_a), dead zone (V_1) and remainder of vessel (V_2)
7) Calculate initial alloy concentration in alloy zone (C_a) and final concentration (C_∞) in V_1 and V_2
8) Simple (analytical) case (two tank only): solve equations 2.37 and 2.38, convert to weight percent and plot concentration versus time or numerical case: solve for concentration change (equations 2.39 and 2.40) and update concentration at each time step, convert to weight percent and plot concentration versus time (repeat)

For the numerical case, the change in concentration in the alloy zone, ΔC_a, is calculated for each time interval, Δt, using equation 2.39.

$$\Delta C_a = -(C_a - C_{\infty,1})\left[\dot{V}_a\left(\frac{1}{V_a}+\frac{1}{V_1}\right)\right]\Delta t \tag{2.39}$$

$$\Delta C_1 = -(C_1 - C_{\infty})\left[\dot{V}\left(\frac{1}{V_1}+\frac{1}{V_2}\right)\right]\Delta t \tag{2.40}$$

In equation 2.39, C_a, represents the alloy concentration in the alloy zone in the previous step, which is then calculated for the current step by summing C_a and ΔC_a. Alloy concentration in the dead zone is determined via a mass balance calculation (any alloy solute leaving the dead zone has to appear in the mixing zone). Equation 2.40 is then employed to find the mass transferred into the mixing zone from the dead zone.

The numerical and analytical models differ by less than 0.05wt%, when a time step of 0.1 seconds is chosen. This is illustrated in Figure 2.21. Unlike the steel shell model, calculation time for mixing is insignificant thus a small time step was chosen (0.01 seconds).

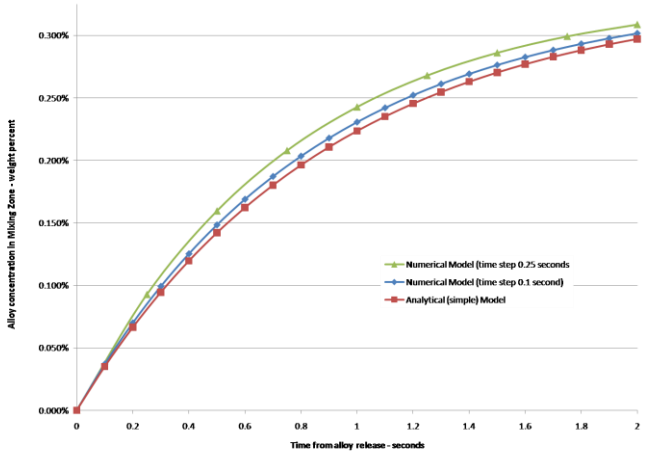

Figure 2.21. Two Tank Mixing Model Output Showing Change in Alloy Concentration for Both the Simple Case Which Has an Analytical Solution and the Numerical Model with Two Different Time Steps, with the Same Input Conditions, to Illustrate the Departure from the Analytical Model

2.7. CLASS II DISSOLUTION MODEL

The steel shell period for Class II alloys is identical to Class I, only the material properties of the alloy are different. If the dissolution of Class II alloys is dominated by diffusion of the alloy species across a boundary layer and the ladle is well mixed, then a simple numerical model (ignoring mixing) can be constructed using equations used by Zhang and Oeters (in modeling total melting time of spherical chromium and 70% ferromolybdenum particles).[184] These equations were introduced in Section 1.5.2. If the ladle is not well mixed then the numerical version of the mixing model may be utilized in conjunction with the dissolution model to better predict alloying behavior.

2.7.1. Simplifying Assumptions. Zhang and Oeters suggest that mass transfer is the rate limiting factor in alloying with high-melting substances[185] Thus the dissolution model was developed so that mass leaving the alloy particle, in any given time step, would be immediately dispersed throughout the steel melt.

Even though slip velocity is a function of alloy radius, Zhang and Oeters suggest that this has little effect on total dissolution time, thus their model was further simplified by assuming a constant slip velocity.[186] This assumption was tested with the spreadsheet model. Unfortunately, this resulted in the model over estimating dissolution for samples obtained late in experiments. Unlike Zhang and Oeters model, the spreadsheet dissolution model updates the slip velocity as the radius changes.

Other assumptions include that the alloy particle is uniformly heated to the solidification temperature of the melt when the steel shell disappears, material properties (diffusivity, steel viscosity, etc.) are constant and that the alloy particle is at terminal velocity or in a region of low steel velocity. Ferroniobium was expected to sink to the bottom of the experimental ladle during the steel shell period, where there is a low steel velocity.

2.7.2. Model Details. Mathematically, the change in radius of the alloy particle with time (dR/dt) can be calculated using a heat transfer equation (2.41) and a mass transfer equation (2.43). From a physical standpoint the rates of both equations must be equal to one another.

In order to solve both equations, the solid-liquid interface temperature and concentration have to be obtained from curve- fit equations for the liquidus line of the

appropriate phase diagram (iron-niobium for the present work).

$$\frac{dR}{dt} = -\frac{h}{C_{P,Melt}\rho_{Melt}} \ln\left(1 + \frac{C_{P,Melt}\rho_{Melt}(T_{Melt} - T_{Interface})}{\rho_{alloy}\Delta H_{sl}}\right) \quad (2.41)$$

Where h is the heat transfer coefficient, $C_{p,melt}$ is melt heat capacity, ρ_{Melt} is the melt density, T_{Melt} is the melt temperature, $T_{Interface}$ is the solid/liquid interface temperature, and ΔH_{sl} is the sum of heat of mixing and latent heat of fusion

$$\frac{dR}{dt} = -k \ln\left(\frac{c_P - c_M}{c_P - c_l}\right) \quad (2.42)$$

Where k is the mass transfer coefficient, c_P is the alloy concentration in the alloy particle, c_M is the melt alloy concentration, and cl is the solid/liquid interface alloy concentration.

Equations for the niobium liquidus line were obtained by measuring the coordinates of the liquidus line from an iron-niobium phase diagram.[187] These coordinates were then fit with a series of linear or second order polynomial equations, which are presented in Table 2.8, where %Nb refers to c_l (weight percent) and $T_{Interface}$ is in Kelvin. The equations in Table 2.8 provided a starting point for the model. Unfortunately, their resolution was not sufficient to obtain agreement between the heat transfer and mass transfer equations without temperature adjustments of up to 5 degrees.

Table 2.8. Liquidus Line Equations for Iron-Niobium.

Concentration Range (weight percent)	Equation
$0 \leq \%Nb \leq 18.6$	$T_{Interface} = -10.61(\%Nb) + 1538$
$18.6 \leq \%Nb \leq 31$	$T_{Interface} = -0.3022(\%Nb)^2+26.91(\%Nb)+1026$
$31 \leq \%Nb \leq 60.6$	$T_{Interface} = -1.173(\%Nb)^2+161.3(\%Nb)-2134$
$60.6 \leq \%Nb \leq 76.7$	$T_{Interface} = -1.137(\%Nb)^2+141.7(\%Nb)-2782$
$76.7 \leq \%Nb \leq 100$	$T_{Interface} = 45.81(\%Nb)-2112$

For calculation stability, an intermediate interface temperature-concentration combination was chosen. The ratio of melt temperature to initial interface temperature was then used to adjust the temperature and concentration difference for computing the heat and mass transfer.

After inputting the initial conditions and material properties, Reynolds, Prandtl, and Schmidt (Sc) numbers (equations 2.13, 2.12, and 2.43) are computed and the Nusselt, and Sherwood (Sh) numbers approximated using equations 2.17 and 2.44 (after evaluating the dissolution model and to better match the shell model, equation 2.19 and 2.45 were ultimately adopted).[188] From the dimensionless numbers (Nu and Sh), the heat and mass transfer coefficients (equations 2.20 and 2.46) were found and used to determine the change in radius, ΔR, over a time step, Δt. Based on the change in radius the mass of alloy released in the time step is calculated and translated into a bulk alloy concentration in the melt (c_m). Before repeating the calculations, melt temperature and slip velocity are updated. (Dissolution model steps are shown included in Appendix)

$$Sc = \frac{\nu_{melt}}{D_{alloy}} \tag{2.43}$$

D_{alloy} – mass diffusivity of alloy in melt; ν_{melt} – melt kinematic viscosity

$$Sh = 0.62\,\mathrm{Re}^{1/2}\,Sc^{1/3} \tag{2.44}$$

$$Sh = 2 + 0.38(\mathrm{Re}\cdot Sc)^{\frac{1}{2}} \tag{2.45}$$

$$k = \frac{Sh\,D_{alloy}}{d_{alloy}} \tag{2.46}$$

Ignoring buoyancy effects, terminal velocity, V_t, is given by equation (2.47).[189] The mass term, m, in the numerator (within the square root) is proportional to alloy radius cubed. The projected area, A, in the denominator is proportional to alloy radius squared. Based on this and the assumption that the alloy would be at or near terminal

velocity, the slip velocity was adjusted at each step by multiplying the initial slip velocity by the square root of the current radius divided by the square root of the initial radius.

$$V_t = \sqrt{\frac{2mg}{\rho A C_D}} \tag{2.47}$$

m – particle mass; g – acceleration due to gravity; ρ – particle density;

A – particle projected area; C_D – particle drag coefficient

3. RESULTS AND DISCUSSION

Results of alloying experiments are presented in Section 3.1. These experiments are organized by alloy class. Class I alloys which melt below the steel bath temperature are presented first, followed by Class II alloys, which have a melting temperature above the steel bath temperature. Experimental conditions for these experiments are shown in Table 3.1 and Table 3.2. Model results and verification follow in Section 3.2 (experiments with a model # in Table 3.1 are modeled in Section 3.2).

Table 3.1. List of Experiments and Experimental Conditions for Class I Alloys

Experiment # (model #)	Alloy	Alloy Form	Alloy Diameter –mm*	Nominal Tap Temperature – °C	Argon Flow Rate – liters per minute	Stirring Power – watts per ton**
1	Ferromanganese	Lump	20	1670	9.2	655
2	Ferromanganese	Lump	30	1670	8.6	610
3	Ferromanganese	Lump	20	1670	4.1	290
4	Ferromanganese	Lump	30	1670	4.2	300
5	Ferromanganese	Lump	20	1670	0	-
6 (Mn-1)	Ferromanganese	Lump	20	1670	4.7	336
7 (Mn-2)	Ferromanganese	Lump	20	1670	10	708
8	Ferromanganese	Lump	20	1670	0	-
9 (Ni-1)	Nickel	Pellet	13.5	1670	4.7	329
10 (Ni-2)	Nickel	Pellet	13.5	1670	10.2	720
11 (Ni-3)	Nickel	Cathode	22/24	1670	4.7	331
12 (Ni-4)	Nickel	Cathode	22/24	1670	10.5	741
13 (Ni-5)	Nickel	Pellet	13.5	1710	4.7	336
14 (Ni-6)	Nickel	Pellet	13.5	1710	9.6	686
15 (Ni-7)	Nickel	Cathode	22/24	1710	5.1	364
16 (Ni-8)	Nickel	Cathode	22/24	1710	10.5	758
17	Nickel	Cathode	22/24	1710	0	-
18 (Sn-1)	Tin	Liquid	-	1670	4.1	290
19 (Sn-2)	Tin	Liquid	-	1670	4.8	339
20 (Sn-3)	Tin	Liquid	-	1670	0	-
21	Tin	Triangular prism	20/24	1670	4.3	303

* diameter of equivalent sphere on mass basis/diameter of equivalent sphere on surface area basis;

** stirring power computed using initial ladle temperature

Table 3.2. List of Experiments and Experimental Conditions for Class II Ferroniobium

Experiment # (model #)	Alloy Form	Alloy Diameter – mm	Nominal Tap Temperature – °C	Argon Flow Rate – liters per minute	Stirring Power – watts per ton
22	Granular	-	1670	10.1	712
23	Granular	-	1670	9.0	634
24	Granular	-	1670	4.3	306
25 (Nb-1)	Lump	10	1670	4.4	313
26 (Nb-2)	Lump	10	1670	9.9	703
27 (Nb-3)	Lump	15	1670	4.5	319
28 (Nb-4)	Lump	15	1670	10.0	710
29 (Nb-5)	Lump	20	1670	5.1	362
30 (Nb-6)	Lump	20	1670	10.4	738

3.1. EXPERIMENTAL RESULTS

Class I ferromanganese, nickel and tin were expected to be liquid after the steel shell period. Class I alloys would then be homogenized by liquid-liquid mixing. Class II ferroniobium was expected to be solid after the steel shell period. Ferroniobium dissolution was expected to be diffusion limited and much slower than the Class I alloys. Chemical composition of the alloys is given in Table 2.3. Alloy properties were given in Table 1.4, with melting point and density reproduced in Table 3.3.

Table 3.3. Melting Points and Densities of Experimental Alloys

Alloy	Melting Temperature - °C	Density - kg/m^3
Low carbon ferromanganese	1200-1205	7230
Nickel	1455	8900
Tin	232	7300 solid 6990 liquid
Ferroniobium	1580-1630	8070

The initial two experimental series departed from the procedure outlined in Section 2.2.6. The ferromanganese and nickel cathode trials were conducted without

preheating the ladle, and with a nominal steel composition of 0.8wt% carbon. In addition, the initial ferromanganese experiments did not use aluminum deoxidation (i.e. the steel was unkilled). Results of these experiments were used to refine the experimental procedure.

The higher carbon content used in initial experiments provided a lower steel liquidus temperature (almost 30°C lower than the chemistry used in the final experiments) extending working times in the ladle by 15 to 25 seconds. The development of better ladle practices to reduce the time between tapping of the furnace and making the alloy addition along with the use of the electric preheater allowed for the change to a nominal 0.4wt% carbon in the later experiments.

3.1.1. Class I: Ferromanganese, Nickel, and Tin. Low carbon ferromanganese (T_{melt} 1200 to 1205°C), nickel (T_{melt} 1455°C), and tin (T_{melt} 232°C) all have melting temperatures below the molten steel temperature. Tin was chosen as a surrogate for low melting additions like sulfur (T_{melt} 119°C), selenium (T_{melt} 220°C), bismuth (T_{melt} 271°C), lead (327°C) or tellurium (T_{melt} 450°C).[190] Low carbon ferromanganese (7.23 g/cm^3) and tin (6.99 g/cm^3) have densities close to liquid steel (7.02 g/cm^3) and are likely to be entrained in the liquid steel flow. In contrast, nickel (8.9 g/cm^3) is denser than steel and would be expected to sink.

Alloys shapes ranged from spherical pellets to lumps. Nickel pellets had an average diameter of 13.5 mm (12.9 grams). Nickel cathode had a rectangular cross section which would approximate a sphere 22 mm in diameter on a mass basis (50 grams) or 24 mm on a surface area basis. Assuming spherical nickel cathodes would result in a surface area to volume ratio of 2.7 per cm rather than the actual nickel cathode ratio of 4.0 per cm. Nickel pellets have a surface area to volume ratio of 4.4 per cm. The cathode shape is also likely to tumble while passing through the steel. Ferromanganese consisted of lumpy spheroids which had been subjected to limited grinding to remove sharp corners. The grinding was primarily to bring the particle weight to a 20 or 30 mm equivalent sphere. Finally, the solid tin had a triangular prism shape (2.7 cm base by 1.4 cm high by 2.2 cm long) which was equivalent to a 20 mm sphere on a mass basis or a 24 mm sphere on a surface area basis.

For ferromanganese, a combination of smaller alloy size and a high stirring rate

(experiment 1: 20 mm-9.2 lpm-655 Watts/Ton) resulted in the rapid dissolution and entrainment of the alloy resulting in the first sample being taken from a manganese rich region (Figure 3.1). After 20 seconds, the manganese in the liquid steel appeared to approach a homogenized value just slightly above the aim of 0.30%. The 20-mm ferromanganese spheroids generally homogenized faster than the 30-mm spheroids. As discussed in Section 3.2.1, modeling indicates that for smaller alloy particles the steel shell period is substantially shorter and the alloy is more likely to be fully molten when the steel shell melts.

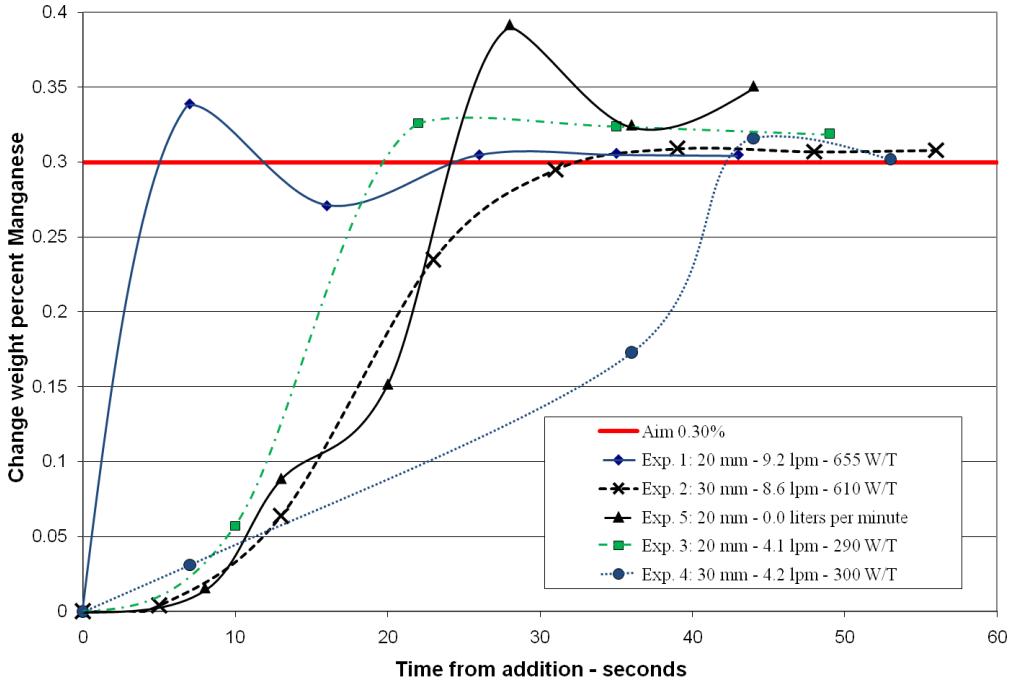

Figure 3.1. Change in Manganese Content in Liquid Steel after Making 0.30% Mn Addition of 20 and 30 mm Diameter Ferromanganese Spheroids with Argon Stirring of 0 to 9.2 lpm (1670 C tap temperature, without ladle preheat; lpm – liters per minute; W/T – watts per ton stirring power). (Curves for illustration)

Experiment 3 (20 mm-4.1 lpm-290 W/T) neared the aim composition at about 20 seconds while experiment 4 (30 mm-4.2 lpm-300 W/T) required 43 seconds to stabilize near the aim (Figure 3.1). Increasing the argon flow rate to 8.6 lpm (610 W/T) for the 30 mm alloy (experiment 2) reduced this time to 38 seconds. The experiment without argon

stirring (experiment 5) was still rich in manganese at the final sample, indicating that natural convection was insufficient to complete mixing within the sampling period.

Three ferromanganese experiments were repeated with preheat in aluminum killed steel with a nominal carbon content of 0.4wt%. Spheroids 20-mm in diameter were chosen so that the alloy would be homogenized within the experimental time. The most significant difference is that the first series homogenized slightly above the aim of 0.30%, while the second series homogenized slightly below the 0.30% aim (Figure 3.2).

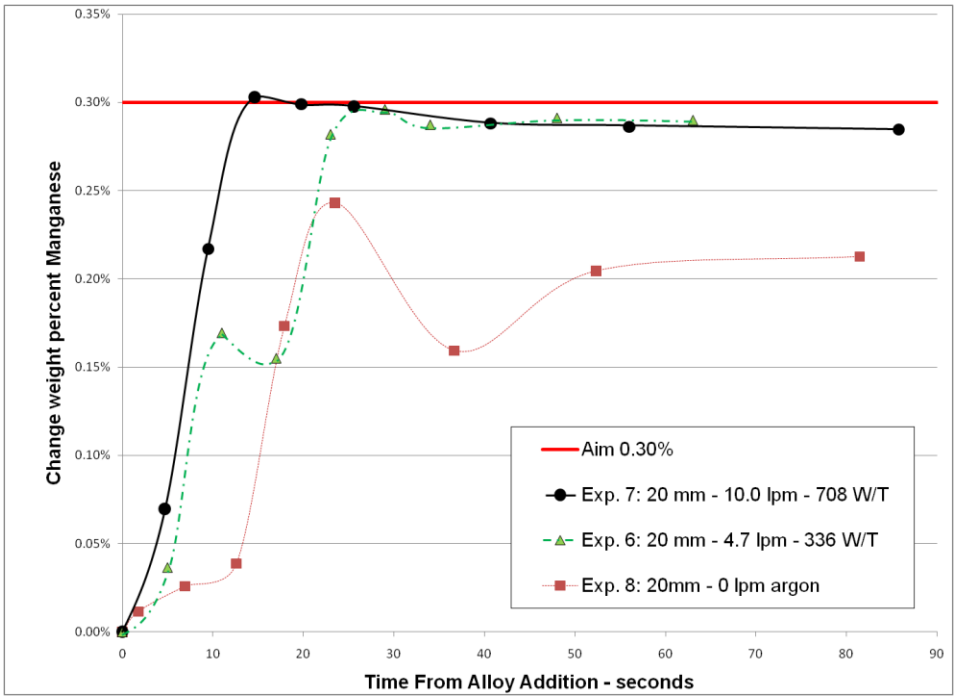

Figure 3.2. Change in Manganese Content in liquid Steel after Making 0.30% Mn Addition of 20 Diameter Ferromanganese Spheroids with Argon Stirring of 0 to 10 lpm (1670 C tap temperature). (Curves for illustration)

Experiment 7 (20 mm – 708 W/T) reached 95% mixed between 10 and 15 seconds, while experiment 1 from the first series (20mm - 655 W/T) reached 95% mixed between 16 and 26 seconds (Figure 3.2). Likewise, experiment 6 (20 mm – 336 W/T) was 95% mixed between 23 and 29 seconds, while experiment 3 (20 mm – 290 W/T) required between 35 to 49 seconds. These 95% mixing time values were determined by finding the samples just before and just after the alloy concentration stayed within 95% to 105% of

the alloy aim. Again the unstirred experiment failed to reach equilibrium within the experimental time.

The smaller diameter nickel pellets (~13.5 mm diameter) mixed more rapidly than the larger ferromanganese spheroids (20 mm and 30 mm), in spite of nickel's higher melting point. In all four nickel pellet experiments, the alloy content approached a constant value between 20 and 25 seconds (Figure 3.3). In the 1710°C tap temperature experiments 14 (9.6 lpm – 686 W/T) and 13 (4.7 lpm – 336 W/T) nickel appears in the melt sooner than the 1670°C experiments (9 and 10). In spite of this head start, the greater stirring power of experiment 10 (720 W/T) pushes the nickel concentration to

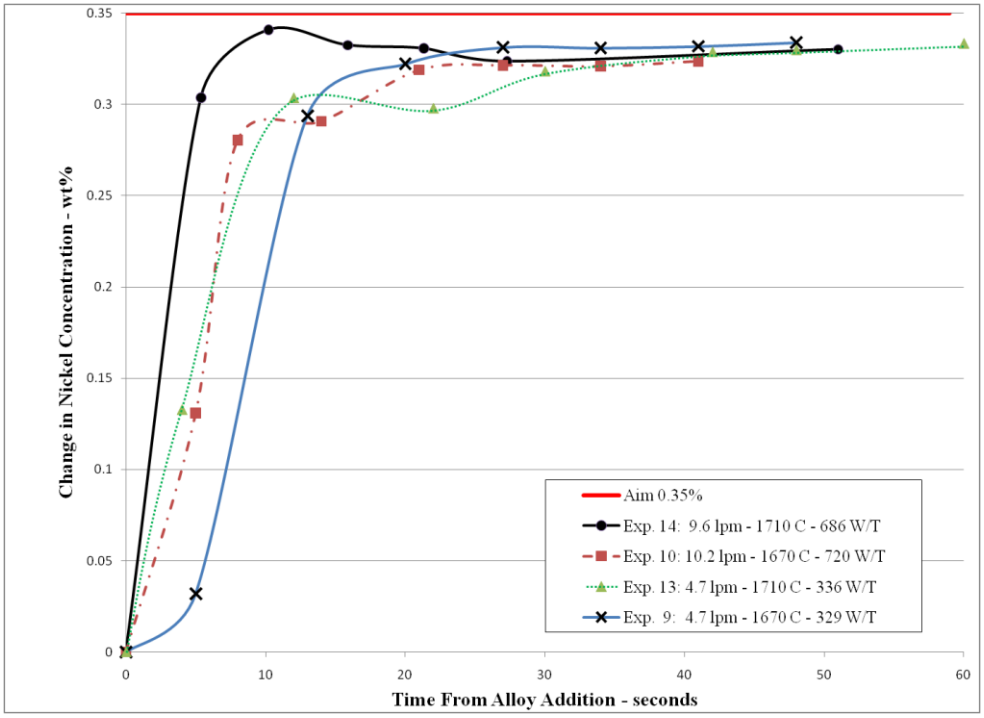

Figure 3.3. Change in Nickel Content in Liquid Steel after Making 0.35% Ni Addition of 13.5 mm Diameter Nickel Pellets with Argon Stirring of 4.7 to 10.2 lpm (1670 and 1710°C tap temperature). (Curves for illustration)

95% mixed sooner (14 to 21 seconds) than experiment 13 (22 to 30 seconds @ 336 W/T), but not as fast as experiment 14 (6 to 12 seconds @ 686 W/T). From this, temperature appears to play a greater role in the shell period than stirring rate, for the

temperatures and stirring rate range studied. Experiment 9 with low temperature and low stirring rate was not the slowest to reach 95% mixed at 13 to 20 seconds.

Nickel cathode without argon stirring (experiment 17) showed increasing nickel concentration during the experiment. This concentration only reached approximately 10% of the nickel in the stirred experiments (Figure 3.4). The initial peak for experiment 16 (10.1 lpm-1710°C-758 W/T) occurred 10 seconds earlier than experiment 12 (10.5 lpm-1670°C-741 W/T). Doubling the gas flow rate from 5.1 lpm to 10.1 lpm, at 1710°C, shortened homogenization time from 35 to 20 seconds. Increasing the melt temperature resulted in faster melting of the alloy, but alloy mixing appears to be the rate-limiting step.

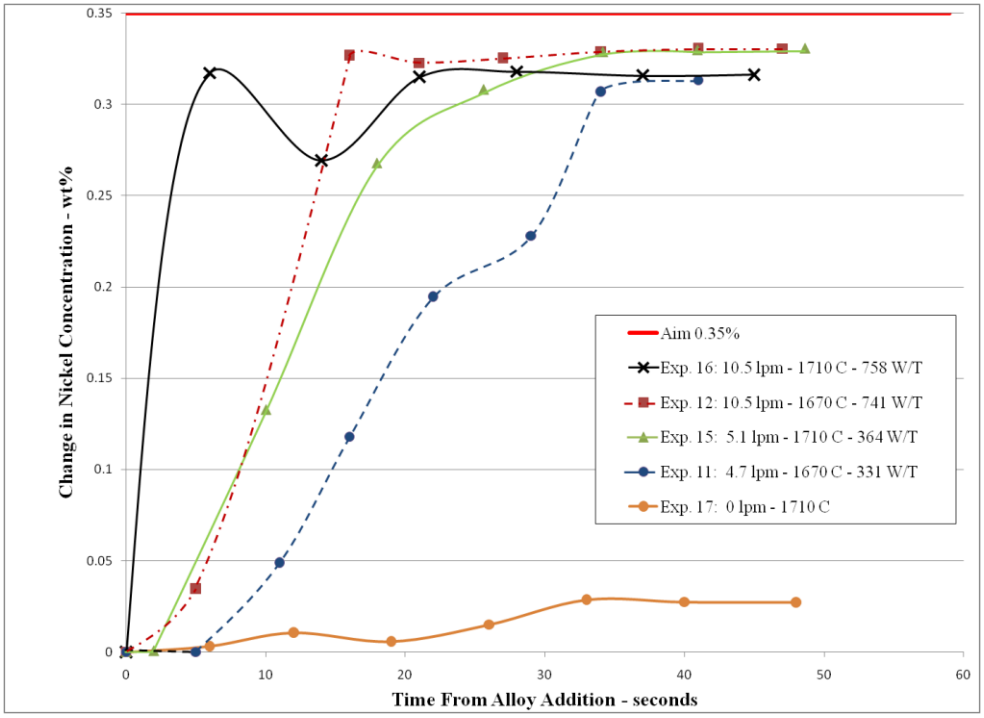

Figure 3.4. Change in Nickel Content in Liquid Steel after Making 0.35% Ni Addition of Nickel Cathode with Argon Stirring of 0 to 10.5 lpm (1670 and 1710°C tap temperature; cathode equivalent to 22 mm nickel sphere on mass basis or 24 mm nickel sphere on surface area basis). (Curves for illustration)

Comparing nickel pellets to cathodes dissolution rate is clearly influenced by alloy particle size/shape (Figure 3.3 and 3.4). Nickel pellets mixed faster than the nickel cathode pieces. The pellets have a surface area to volume ratio of 4.4 per cm compared to

cathode at 4.0 per cm. heat transferred to the pellet is proportional to surface area, while the mass absorbing the heat is proportional to volume. At approximately five seconds and 4.7 lpm argon flow rate, a measurable change in nickel concentration occurred for the pellets while the cathodes still measured at the background level indicating no appreciable melting; this difference was even more evident at the next sample point (13 and 11 seconds, pellet and cathode) where the nickel from the pellets was approximately 85% of the final nickel content while the cathode nickel was approaching 15% of the final nickel content.

Liquid tin additions give a better indication of mixing behavior in the experimental ladle by eliminating the complication of a steel shell period. Liquid tin, at 315°C, was added to the ladle. As was also seen with granular ferroniobium, argon stirring appeared to transport the alloy across the steel surface prior to mixing. A single experiment was conducted with solid tin (20 mm diameter equivalent).

Argon stirring rapidly homogenized the tin and improved recovery from 57% (no argon stirring – experiment 20) to more than 92% (experiments 18, 19 and 21 in Figure 3.5). Poor recovery, without argon stirring is likely due to poor mixing, as metallic tin should be thermodynamically stable in an iron-carbon melt, especially in the presence of aluminum. Even though tin has a short steel shell period, the solid addition required 8 seconds longer to reach 95% of the final concentration than the 7 seconds for the liquid tin addition. One other factor that led to some of the inconsistencies in results is sampling technique. Although the procedure established sampling at the same location in the ladle in each case, it was difficult to assure that each sample was taken at exactly the same location. A difference in sample location would lead to different results based on the differences in the flow fields in the ladle. Rapid mixing precluded the evaluation of tin at higher argon flow rates.

In the present work, alloy additions were made to the “eye” of the gas stirred ladle and sampling occurred near the bottom-center of the ladle but the resulting experimental plots of alloy concentration with time were generally a combination of curves A and B from Figure 1.12, rather than the sigmoidal curve suggested by Oeters in Section 1.8.1. Similar curves were observed by Peter et al. when taking samples from a 120 ton ladle.[191] An example dissolution curve for silicomanganese addition to the 120 ton ladle is shown

in Figure 3.6. The peak in the curve results from sampling from an alloy rich region which circulates through the ladle while the alloy is homogenized.

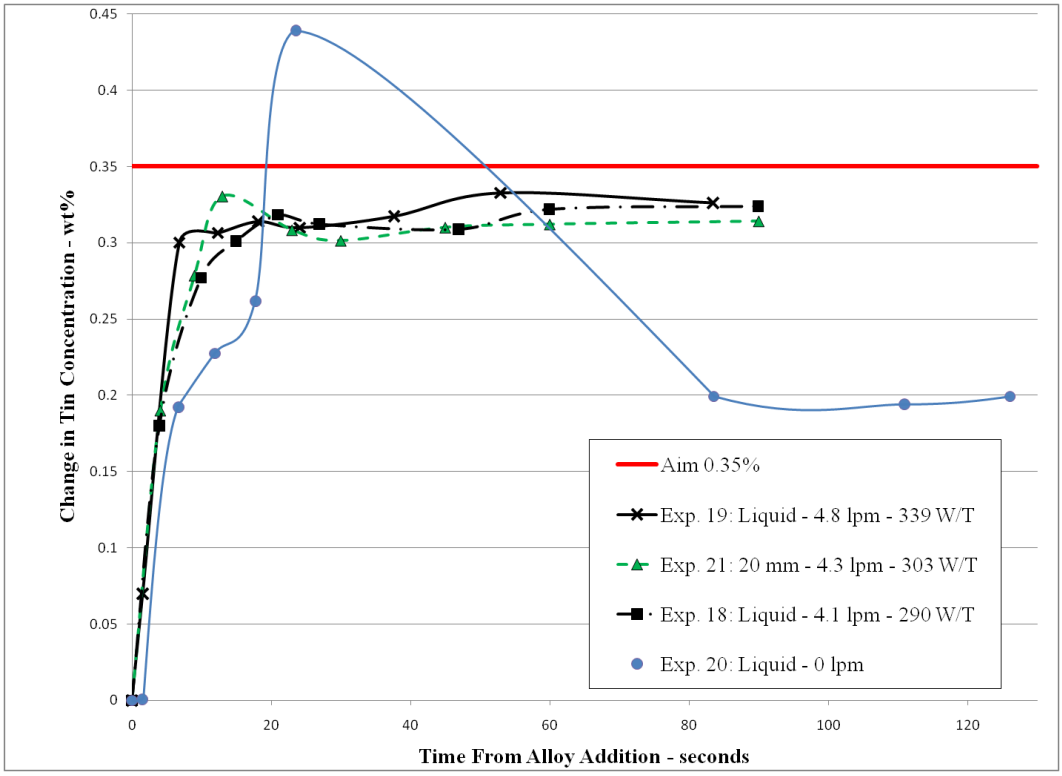

Figure 3.5. Change in Tin Content in Liquid Steel after Making 0.35% Sn Addition of Liquid or Solid Tin with Stirring of 0 to 4.8 lpm (1670°C tap temperature; solid tin equivalent to 20 mm sphere on mass basis or 24 mm sphere on surface area basis). (Curves for illustration)

In five cases (experiments 1, 4, 5, 7, and 20), the measured alloy concentration exceeds the final homogenized target concentration, mimicking the behavior seen in Figure 3.6. Similar behavior is seen in experiments 9, 16, and 21, but the peak concentration and homogenized alloy concentrations are below the final homogenized alloy aim. Peter's model indicates that the alloy rich region circulates in the ladle, moving past the sampling point.[193] This movement of the unhomogenized region may be evident in experiments 5, 6, and 8 where the concentration undulates, moving from a high concentration to a lower concentration and then to a higher value (Figure 3.1 and 3.2).

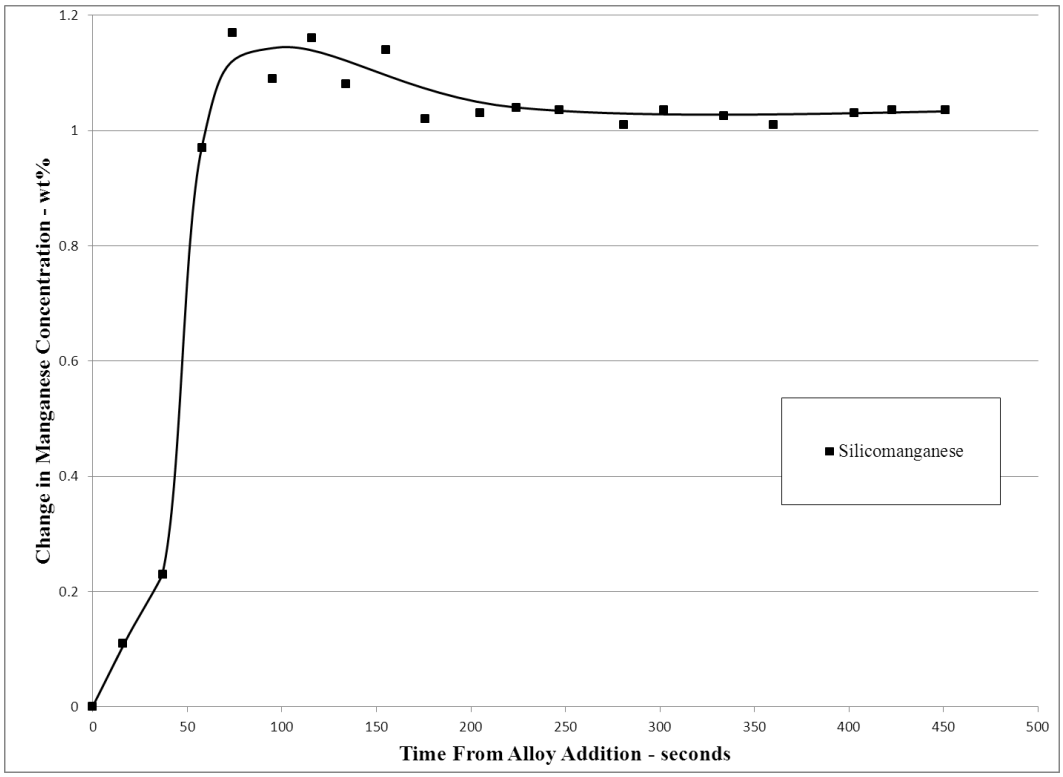

Figure 3.6. Change in the Manganese Content in Liquid Steel after a Silicomanganese Addition of 13 to 64 mm Spheroids to a 120-ton Ladle with Argon Stirring of 113 lpm[192]

3.1.2. Class II: Ferroniobium. Ferroniobium is a Class II alloy with a solidus temperature of 1580°C, liquidus of 1630°C and density of 8.07 g/cm^3. Initially, the steel temperature in the ladle would be high enough to melt the ferroniobium but heat transfer rates would preclude melting. Gourtsoyannis, Guthrie, and Ratz suggest that standard (66%) ferroniobium probably consist of two high melting point niobium-iron compounds at steel making temperatures and that intermediate eutectic liquid formation would be sluggish.[194] Ferroniobium dissolution was expected to be limited by diffusion through a boundary layer at the alloy surface.

Ferroniobium was used in two forms, lump and granular. The granular material was observed floating on the melt surface after addition and agglomerating at the ladle wall. Less agglomeration was noted in experiment 22 than 23. During stirred experiments, the particles were pushed against the edge of the vessel by the movement of steel, but during the unstirred experiments, the ferroniobium was visible on the surface for more than 30 seconds. In spite of the floating, the granular material approached the

alloy aim, well within the experimental time (Figure 3.7). Lump additions only approached one third to just over one half of the 0.30% aim (Figure 3.8). Homogenization time for granular material was around 60 seconds at 4.3 lpm and 40 seconds at 10.1 lpm; this is only about one third the rate of nickel pellets, which mixed to a similar degree by 21 seconds at 10.2 lpm.

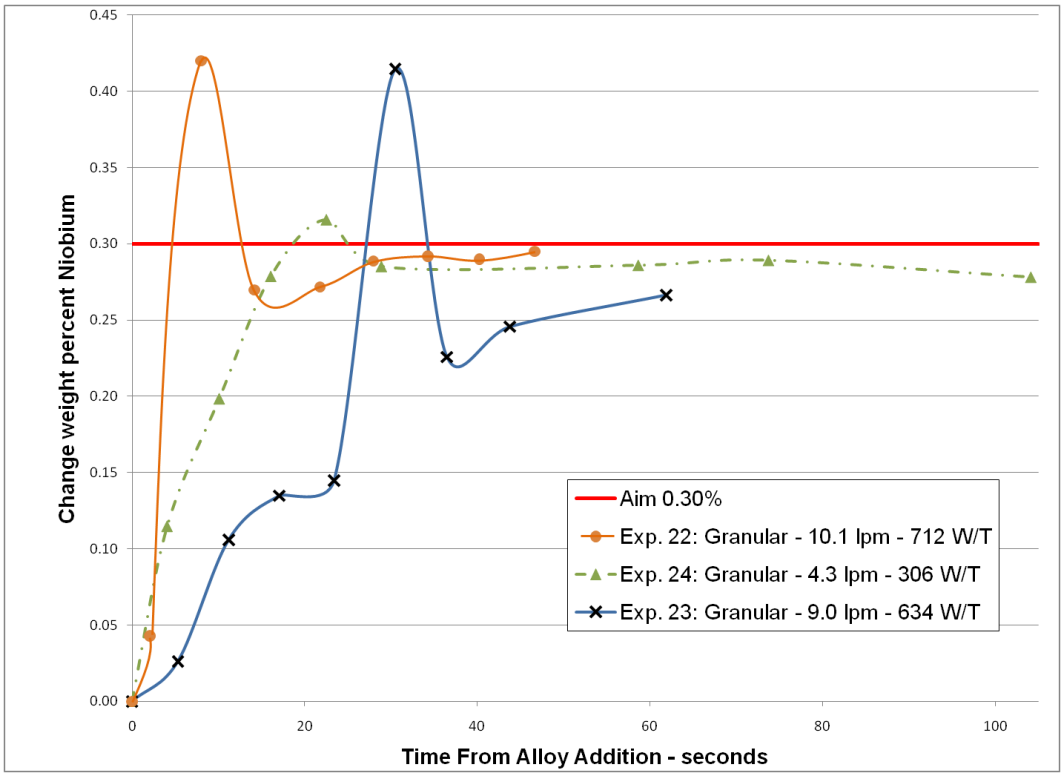

Figure 3.7. Change in Niobium Content in Liquid Steel after Making 0.30% Nb Addition of Granular Ferroniobium with Stirring of 4.3 to 10.1 lpm (1670 °C tap temperature). (Curves for illustration)

The ferroniobium lump additions dissolved slowly and only approached two thirds of the aim of 0.30%. As was the case for nickel and ferromanganese, higher stirring rates resulted in faster dissolution. Sismanis and Argyropoulos analyzed the dissolution of ferroniobium lumps in induction melts and concluded that the assimilation time should be proportional to lump diameter.[195] This was the case for the first 60 seconds at low stirring rates (experiments 25, 27 and 29 in Figure 3.8) where dissolution rate for 10 mm

was faster than 15 mm which was faster than 20 mm lumps. At 80 seconds experiment 29 (20 mm - 362 W/T) reached a niobium concentration higher than experiment 27 (15 mm – 319 W/T). This change in dissolution rate may be related to the substantially higher stirring power available to the larger particles. At high stirring rates (experiments 26, 28, and 30) the smaller lumps dissolved faster than the larger lumps for the first 20 seconds, at which time the dissolution rate of the 10 mm particles (703 W/T) fell below the 15 mm particles (710 W/T). At 40 seconds the 10 mm dissolution rate dropped below the 20 mm rate (738 W/T).

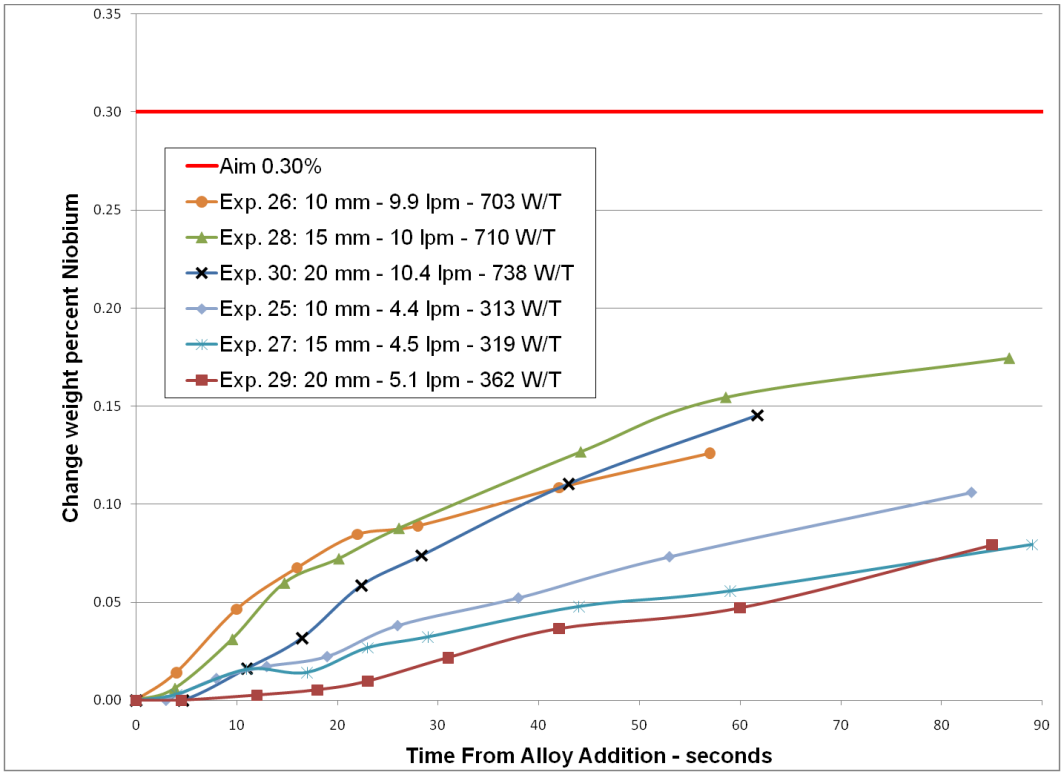

Figure 3.8. Change in Niobium Content in Liquid Steel after Making 0.30% Nb Addition of 10, 15, and 20 mm Ferroniobium Lumps with Stirring of 4.4 to 10.4 lpm (1670°C tap temperature). (Curves for illustration)

3.1.3. Experimental Evaluation Mixing Time, Alloy Transfer Rate, and Alloy Delay. Two simple methods to compare experimental results were used prior to computer modeling. First, a mixing time range was found from the experimental data. Second,

linear trend lines were fit to plots of alloy concentration change versus time from alloy addition. The slope of this line was used to determine the initial alloy transfer rate to the steel bath. These lines were extrapolated to find the time at which alloy first entered the steel bath. This delay accounts for the steel shell period and the time for alloy to reach the sample position. Mixing time, alloy transfer rate and the delay after addition could not be determined for all of the experiments. In some cases the alloy did not homogenize enough to determine a mixing time (e.g. experiment 20, Figure 3.5). In other experiments there was insufficient data prior to the alloy peak to fit the trend line (e.g. experiment 14, Figure 3.3) and in several cases the extrapolated slope would result in a negative time delay (e.g. experiment 8, Figure 3.2).

3.1.3.1 Mixing time range. Mixing time range in Table 3.4 was found by taking the sample time just before and just after reaching 95% mixed for Class I alloys and granular ferroniobium. The mixing time criterion had to be modified for experiment 5, 16, and 20. In experiment 16, the initial sample exceeded 95%, but the subsequent sample was less than 95% mixed. In experiments 5 and 20, the alloy concentrations stayed above 105% of the alloy aim indicating that the alloy was not homogenized by the end of the experiment.

For Class II alloy lumps, none of the spheroidal ferroniobium additions approached the 95% mixing level within the experimental period. The steel in the ladle would have been frozen long before reaching 95% mixed. A new mixing criterion of 33% was chosen for ferroniobium lumps (Table 3.5).

The midpoint of each mixing time range from Table 3.4 was found and the data plotted versus stirring power. Nickel cathode and 30-mm ferromanganese fall within a band which shows decreasing mixing time with increased stirring power in Figure 3.9. Five of six 20-mm experiments also fall within this band. Measured mixing time range is not very sensitive relative to alloy size in the 20 to 30 mm range for ferromanganese. Nickel pellets and tin reached the 95% mixing time faster than the larger nickel and ferromanganese particles.

Table 3.4. Mixing Times and Alloy Transfer Rates for Class I Alloys and Granular Ferroniobium

Exp. #	Alloy	Alloy Size – mm	Stirring Power – W/T	Measured 95% mixing time – s	Initial Alloy Transfer Rate – g/s	Area Specific Alloy Transfer Rate – $g/s \cdot cm^2$	Specific Alloy Transfer Rate divided by stirring power – $g \cdot T / s \cdot cm^2 \cdot W$
1	FeMn	20	655	16 to 26	-	-	-
2	FeMn	30	610	23 to 31	5.40	0.095	1.6×10^{-4}
3	FeMn	20	290	35 to 49	10.08	0.160	5.5×10^{-4}
4	FeMn	30	300	36 to 44	3.15	0.056	1.9×10^{-4}
5	FeMn	20	no argon	20 to 28*	8.15	0.130	-
6	FeMn	20	336	23 to 29	5.85	0.093	2.8×10^{-4}
7	FeMn	20	708	10 to 15	10.53	0.168	2.4×10^{-4}
8	FeMn	20	no argon	<95% mixed	0.01	0.0001	-
9	Nickel	13.5	329	13 to 20	14.72	0.184	5.6×10^{-4}
10	Nickel	13.5	720	14 to 21	22.41	0.280	3.9×10^{-4}
11	Nickel	22	331	34 to 41	5.94	0.109	3.3×10^{-4}
12	Nickel	22	741	5 to 16	11.97	0.219	3.0×10^{-4}
13	Nickel	13.5	336	22 to 30	9.59	0.120	3.6×10^{-4}
14	Nickel	13.5	686	6 to 12	-	-	-
15	Nickel	22	364	26 to 34	7.52	0.137	3.8×10^{-4}
16	Nickel	22	758	14 to 21	-	-	-
17	Nickel	22	no argon	<95% mixed	0.27	0.005	-
18	Tin	Liquid	290	15 to 21	5.49	-	-
19	Tin	Liquid	339	12 to 18	19.67	-	-
20	Tin	Liquid	no argon	23 to 29*	7.74	-	-
21	Tin	20	303	10 to 15	7.16	0.065	2.2×10^{-4}
22	FeNb	Granular	712	22 to 28	28.76	-	
23	FeNb	Granular	634	44 to 62	4.14	-	
24	FeNb	Granular	306	10 to 16	5.00	-	

*experiment stayed above 105% of alloy aim

Table 3.5. Mixing Times and Alloy Transfer Rates for Ferroniobium Lumps

Exp.	Alloy Size – mm	Stirring Power – W/T	Measured 33% mixing time – S	Initial Alloy Transfer Rate – g/s	Area Specific Alloy Transfer Rate – $g/s \cdot cm^2$	Specific Alloy Transfer Rate divided by stirring power – $g \cdot T / s \cdot cm^2 \cdot W$
25	10	313	53 to 83	0.45	0.003	0.95×10^{-5}
26	10	703	28 to 42	2.03	0.013	1.9×10^{-5}
27	15	319	>89	0.50	0.005	1.6×10^{-5}
28	15	710	26 to 44	1.89	0.019	2.7×10^{-5}
29	20	362	>85	0.27	0.004	0.99×10^{-5}
30	20	738	28 to 43	1.31	0.017	2.3×10^{-5}

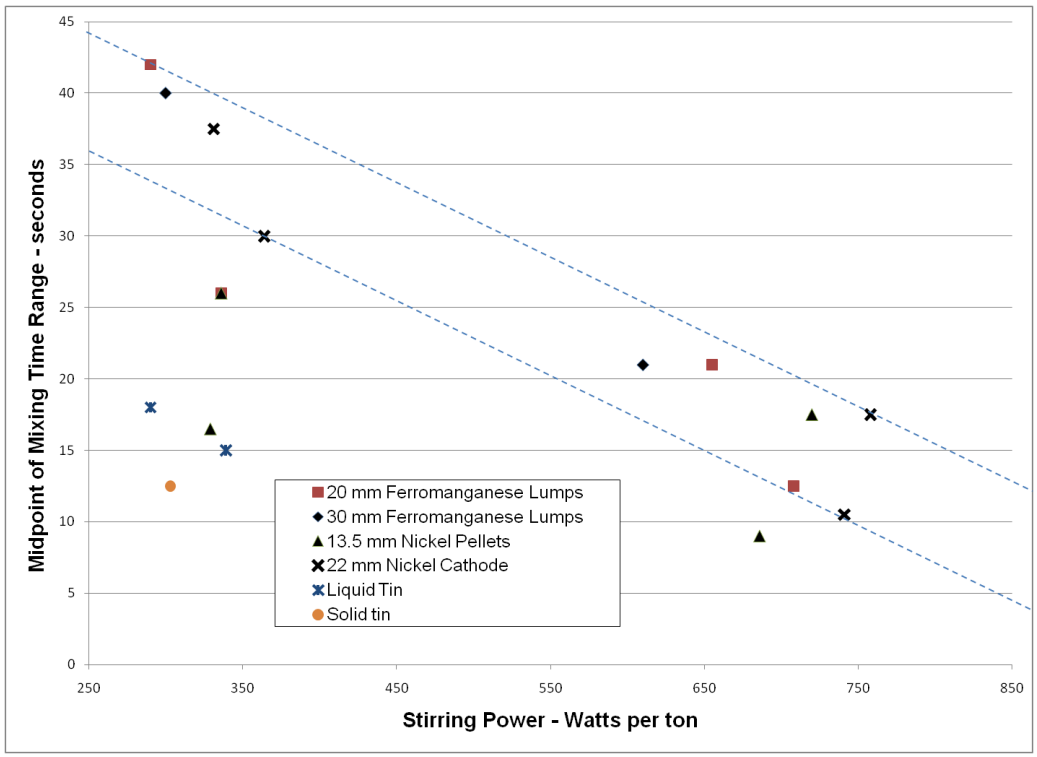

Figure 3.9. Midpoint of Measured 95% Mixing Time Range for Class I Alloys (from Table 3.4) versus Stirring Power, Showing Trend of Decreasing Mixing Time with Increased Stirring Power. (Dashed lines show boundaries for nickel cathode. 30 mm ferromanganese and 5 of 6 20-mm ferromanganese experiments fall within the same band)

Mixing time range is a relatively crude method of determining mixing time as samples are 5 to 18 seconds apart. Several experiments showed behavior where mixing time did not decrease with stirring power. Nickel pellet experiment 10 (720 W/T – 14 to 21 seconds) required slightly longer to reach 95% mixed compared to experiment 14 (686 W/T – 6 to 12 seconds). But, experiment 14 started at a higher temperature (1643 versus 1620ºC), which should have released the alloy from the steel shell sooner. This anomaly points to a possible issue with dissolution route assumptions at higher temperature

In addition, experiment 14 overshoots the final homogenized alloy concentration and then settles to a lower concentration, while experiment 10 rises to the homogenized value. In nickel cathode work, experiment 16 (758 W/T – 14 to 21 seconds) overshoots the final concentration, while experiment 12 (741 W/T – 5 to 16 seconds) rises

continuously to the 95% mixed value (Figure 3.4). This difference is likely an artifact of sampling.

Granular ferroniobium also showed mixed results for mixing time versus stirring power. Experiment 24 with the least stirring power (306 W/T) had the shortest mixing period, while experiment 23 (634 W/T) lagged experiment 22 (712 W/T) by nearly 30 seconds. This is likely due to the alloy agglomeration seen during these experiments.

Tin was somewhat surprising. Liquid tin (experiments 18 and 19) had similar mixing times at nearly the same stirring power as experiment 9 (nickel pellet), but the liquid would have been immediately available, while the nickel would have had a steel shell period. Tin and iron form two liquids between 48.8% and 85.5% at less than 1505°C. This lack of miscibility would decrease liquid-liquid mixing until the tin had warmed to liquid steel temperature. Although it is not evident in Figure 3.5, experiment 19 (liquid tin – Figure 3.5) most likely reached the 95% mixed level in a shorter time than experiment 20 because solid tin formed a shell (model shell period of 0.01 seconds). Samples in experiment 20 were taken at shorter intervals than in experiment 19 as the alloy concentrations reach 95% of the alloy aim. As a result experiment 20 has a shorter reported mixing time range than experiment 19.

Although 33% mixing times (Table 3.5) have no industrial value, they are useful for evaluating the dissolution model results presented in Section 3.2.4 where dissolution was very slow. For lump ferroniobium, mixing times decreased with increasing stirring power and decreasing alloy size.

In summary, mixing time decreased with increasing stirring power and as the alloy particle size decreased. Anomalous behavior was seen with ferromanganese and nickel at higher ladle temperatures, which was likely due to a change in dissolution route. This change is discussed in Section 3.2. Additionally, ferroniobium lump dissolution was too slow to use a 95% mixed criterion.

3.1.3.2 Initial alloy transfer rate. The second evaluation method involved determining an initial alloy transfer rate. Many experiments captured two or more data points before the alloy concentration peaked. A linear line was fit through these points to obtain an initial alloy transfer rate. The trend line was fit through as many data points, up to the concentration peak, as possible while maintaining an R^2 greater than or equal to

0.90. Slopes of the lines were then found and the change in alloy concentration with time converted to mass per unit time (grams per second). These values are given in Table 3.4 and 3.5. Unfortunately, experiments 1, 14, and 16 were at peak concentration on the first sample preventing a linear fit.

Alloy transfer rates ranged from 0.01 g/s for natural convection (experiment 8) to 28.76 g/s for granular ferroniobium (experiment 22). Natural convection (experiments 5, 8, 17, 20), did not result in vigorous enough stirring to bring the alloy concentration to the desired aim within the experimental time, but experiments 5 (20 mm ferromanganese) and 20 (liquid tin) showed moderate alloy transfer rates of 8.15 and 7.74 g/s, while experiments 8 (20 mm ferromanganese) and 17 (nickel cathode) were the lowest at 0.01 and 0.27 g/s.

Ferromanganese transfer rates for 30-mm lumps were lower than 20-mm lumps. Experiment 4 (30 mm - 300 W/T) and 2 (30 mm – 610 W/T) had transfer rates of 3.15 and 5.4 g/s, showing an increase with stirring power. Experiments 3 (290 W/T - 1626ºC), 6 (336 W/T – 1642ºC), and 7 (708 W/T - 1625 ºC) with 20 mm lumps had transfer rates of 10.08, 5.85, and 10.53 g/s.

Nickel cathode experiments 11 (331 W/T – 5.94 g/s), 15 (364 W/T – 7.52 g/s), 12 (741 – 11.97 g/s) and tin experiments 18 (290 W/T – 5.94 g/s), 21 (303 W/T – 7.16 g/s), and 19 (339 W/T – 19.67 g/s) all showed increasing alloy transfer rates with increasing stirring power. But the pattern of low alloy transfer rate at higher temperature, seen with ferromanganese, was also seen with nickel pellets. Nickel pellet experiments 9 (329 W/T - 1603ºC), 13 (336 W/T - 1642ºC), and 10 (720 W/T - 1620ºC) had transfer rates of 14.72, 9.59, and 22.41 g/s, respectively.

A possible explanation for poor alloy transfer rates at higher temperature and with larger alloy particles was seen with the steel shell model (Section 3.2). Ferromanganese likely follows dissolution route 3 (Figure 1.5), where the steel shell melts back prior to the alloy completely melting with a new thinner shell forming on the remaining solid. This second shell reduces the amount of liquid alloy available for mixing. The 30-mm ferromanganese particles would have a larger remaining solid core than 20-mm particles when the initial shell melts. For nickel, route 1 is more probable at lower experimental temperatures (~1600°C), with a transition to route 3 as the ladle temperature increases.

Alloy transfer rates were higher for the pure elements nickel and tin than for the ferroalloy (manganese). As with mixing time, tin transfer rates were surprisingly low, being very similar to nickel cathode (even though tin did not have a shell period for the liquid additions experiment 18 and 19). This again could be attributed to poor miscibility for tin and a second steel shell forming on ferromanganese.

Alloy transfer rate for Class II lump ferroniobium was about an order of magnitude lower than the Class I alloys. At higher stirring powers, alloy transfer rate increased with stirring power and decreased with alloy size. Experiments 26 (10 mm – 703 W/T), 28 (15 mm – 710 W/T), and 3 (20 mm – 738 W/T) had alloy transfer rates of 2.03, 1.89, and 1.31 g/s. At the lower stirring rate, the 15 mm rate was slightly elevated relative to the 10 mm value. Experiment 25 (10 mm – 313 W/T), 27 (15 mm – 319 W/T) and 29 (20 mm – 362 W/T) had alloy transfer rates of 0.45, 0.50, and 0.27 g/s.

Granular ferroniobium transfer rates did not appear to be directly related to stirring power. Again this is likely due to alloy agglomeration. Granular ferroniobium transfer rates were on the same order as Class I alloys with values ranging from 4.14 (634 W/T), to 5.0 (306 W/T) and 28.76 (712 W/T) g/s.

3.1.3.3 Specific initial alloy transfer rate. The initial alloy transfer rate is an indication of how rapidly alloy liquid mixes with steel. A 10 mm particle has two and three times the surface area to volume ratio of 20 and 30 mm particles, respectively. In order to better evaluate the effect of alloy size, an area specific alloy transfer rate was calculated. The initial alloy transfer rate was divided by the original alloy surface area (cm^2). The resulting units are grams per second · centimeter squared.

For area determination, lumps and pellets were assumed to be spherical, while nickel cathode and solid tin used actual surface area. Granular ferroniobium would have an estimated surface area of 3000 to 5500 cm^2/g, but in practice much of the material agglomerated on the melt surface prior to dissolving. This agglomeration precludes estimation of area specific alloy transfer rate.

Specific alloy transfer rate shows that for a given stirring power, 30 mm ferromanganese (300 W/T – 0.056 $g/s \cdot cm^2$ and 610 W/T – 0.095 $g/s \cdot cm^2$) has a lower transfer rate than 20 mm ferromanganese (290, 336, and 708 W/T with 0.16, 0.093, 0.168 $g/s \cdot cm^2$, respectively – Table 3.4). Nickel cathode had a higher transfer rate (0.22 to 0.28

g/s·cm^2) than nickel pellets (0.12 to 0.18 g/s·cm^2) at lower stirring powers (329 to 364 W/T), but nickel pellets (720 W/T – 0.28 g/s·cm^2) had a higher rate at the higher stirring power than nickel cathode (741 W/T – 0.11 g/s·cm^2). Solid tin (303 W/T - 0.065 g/s·cm^2) was very close to the lowest 30 mm ferromanganese value (300 W/T – 0.056 g/s·cm^2).

Ferroniobium lumps again had much lower transfer rates than Class I alloys. Transfer rates ranged from 0.003 to 0.005 g/s·cm^2 for stirring powers from 313 to 362 W/T and 0.013 to 0.019 g/s·cm^2 for 703 to 738 W/T (Table 3.5). Gourtsoyannis, Guthrie, and Ratz employed a similar method for determining alloy transfer rates when evaluating niobium dissolution (Section 1.5.6 p. 24; Table 1.5).[196] They published niobium transfer rates between 0.0043 and 0.057 g/s·cm^2.

In order to evaluate the effect of stirring power across alloys, the area specific alloy transfer rate was divided by stirring power. For Class I alloys, the values ranged from 1.6 x10^{-4} to 5.6 x10^{-4} g·T/ s·cm^2·W (Table 3.4). Ferroniobium was a full order of magnitude slower, ranging from 0.95 x10^{-5} to 2.7x10^{-5} g·T/ s·cm^2·W (Table 3.5). Scatter in the data likely reflects variation in experimental procedure, improved ladle practice with experience, and limited sampling resolution/sample position. The widest spread occurs within ferromanganese (experiments 1 to 5; 1.6x10^{-4} to 5.5x10^{-4}), which includes the first experimental series. The range narrows for nickel (3.0 x10^{-4} to 5.6 x10^{-4}) and the follow-up ferromanganese experiments (experiments 6 and 7; 2.4 x10^{-4} to 2.8 x10^{-4}).

3.1.3.4 Delay between alloy addition and appearance of alloy in melt. Trend lines used for the initial alloy transfer rate were extrapolated to the x-axis to approximate the time at which alloy first appeared in the melt (shown as ‘Melting Time Linear Fit’ in Table 3.6; temperature values shown were measured in the ladle just prior to alloy addition). This provides an estimate of the time required for the shell to melt and the alloy to be transported to the sample position.

For Class I alloys there appears to be a strong relationship between increasing ladle temperature and a decrease in the time required for alloy to be measured in the melt. Increasing stirring power also speeds the entry of alloy into the melt (see experiments 7 and 12).

Table 3.6. Melting Time from Linear fit of Experimental Data and Spreadsheet Model

Experiment #	Alloy	Size/form	Initial Ladle Temp °C	Stirring power W/T	Melting Time Linear Fit seconds	Predicted Steel Shell Period from Spreadsheet Model
2	FeMn	30 mm lump	1628	610	4.64	-
3	FeMn	20mm lump	1626	290	7.46	-
4	FeMn	30 mm lump	1640	300	2.97	-
5	FeMn	20mm lump	1629	-	6.90	-
6	FeMn	20mm lump	1642	336	3.34	1.56
7	FeMn	20mm lump	1625	708	2.37	1.75
9	Ni	13.5 mm pellet	1603	329	4.02	1.47
10	Ni	13.5 mm pellet	1620	720	2.38	1.32
11	Ni	22 mm cathode	1618	331	7.23	2.55
12	Ni	22 mm cathode	1620	741	3.69	2.52
13	Ni	13.5 mm pellet	1642	336	-	1.11
14	Ni	13.5 mm pellet	1643	686	-	1.10
15	Ni	22 mm cathode	1643	364	1.98	2.12
16	Ni	22 mm cathode	1662	758	-	1.85
25	FeNb	10 mm lump	1632	313	-	0.49
26	FeNb	10 mm lump	1630	703	1.37	0.49
27	FeNb	15 mm lump	1625	319	2.39	0.94
28	FeNb	15 mm lump	1632	710	2.48	0.89
29	FeNb	20 mm lump	1628	362	9	1.38
30	FeNb	20 mm lump	1631	738	5.28	1.35

For 20 mm ferromanganese, experiments 3 (290 W/T), 5 (no argon), and 6 (336 W/T) cluster along a line (R^2=0.9973) where the delay between alloy addition and a measured increase in alloy concentration is reduced from 7.46 seconds at 1626ºC to 3.34 seconds at 1642ºC (Figure 3.10). In contrast, experiment 7 (708 W/T - 1625 ºC; shown as outlier in Figure 3.10) which had more than twice the stirring power of 3, 5, and 6, falls

well below the trend line. In this experiment, there was a measurable change in manganese concentration 2.37 seconds after the alloy addition.

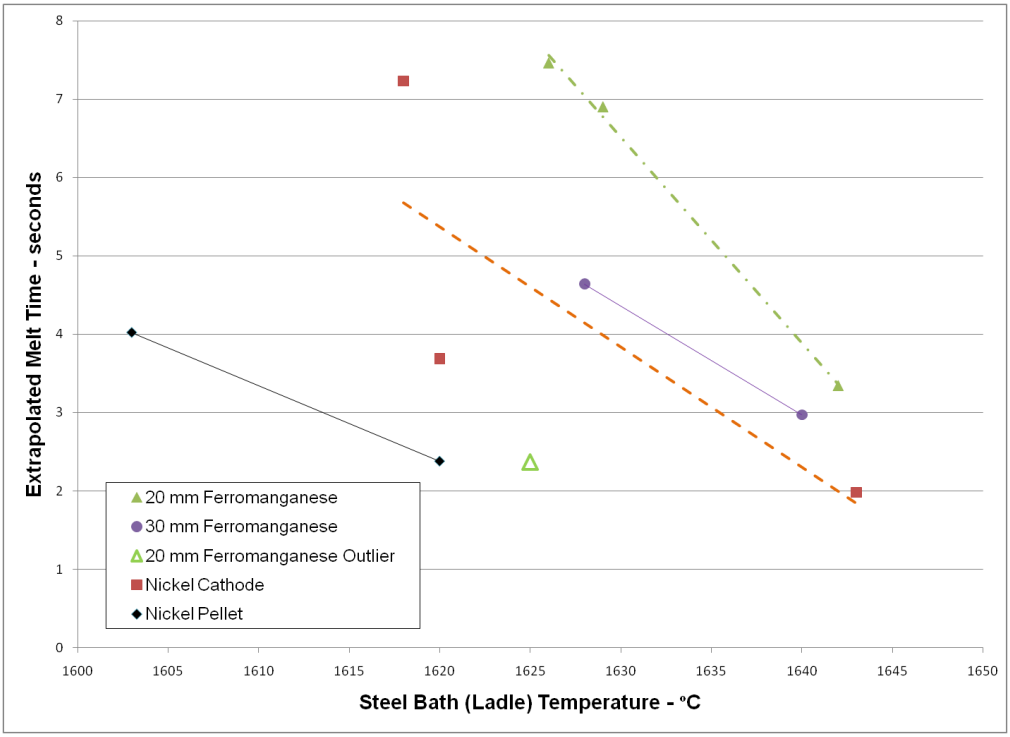

Figure 3.10. Time to First Appearance of Alloy in the Melt (combined steel shell melting time and initial mixing time delay) for Ferromanganese (20 and 30 mm) and Nickel (pellet and cathode) versus Initial Steel Bath (ladle) Temperature (extrapolated from experimental data). 20 mm Ferromanganese Outlier Had More Than Two Times the Stirring Power of the Other 20 mm Ferromanganese Experiments

Surprisingly, 30 mm ferromanganese particles have a shorter delay than the 20 mm ferromanganese. This delay was 4.64 and 2.97 seconds at 1628 and 1640 ºC. Experiment 4 (1640ºC) has relatively low alloy transfer rates which slopes the trend line towards a short delay (Figure 3.1). In addition, experiment 2 (4.64 seconds) has a measured value of 0.004% above the starting manganese concentration at 5 seconds.

Increasing the steel bath temperature, with nickel pellets, decreased the time between alloy addition and a measured change in nickel concentration. This time was 4.02 seconds at 1603ºC and 2.38 seconds at 1620 ºC (experiment 9 – 329 W/T and 10 – 720 W/T).

The time delay between nickel cathode addition and measured increase in nickel concentration was shortened by increasing bath temperature and to a lesser extent by increasing stirring power. In experiment 11 (331 W/T - 1618 ºC) and 12 (741 W/T - 1620ºC) the alloy concentration begins to rise 7.23 and 3.69 seconds after alloy addition. Experiment 15 (364 W/T - 1643ºC) conducted at a higher temperature only had a delay of 1.98 seconds. Nickel cathode with a surface area to volume ratio of 4 cm^{-1} took longer to deliver measurable alloy into the melt than nickel pellets (4.4 cm^{-1}) at 1620ºC.

For ferroniobium, the 10-mm lump addition (experiment 26 – 703 W/T) showed the shortest period between addition and measurement of alloy in the melt, requiring only 1.37 seconds at 1630ºC. Lumps of 20-mm ferroniobium (experiment 29 – 362 W/T and 30 – 738 W/T) required 9 and 5.28 seconds at 1628 and 1631ºC, respectively, to transfer alloy to the melt. 15-mm ferroniobium did not follow the trend seen with other alloys. Experiment 27 (319 W/T) had a delay of 2.39 seconds at 1625ºC but experiment 28 (710 W/T) required a slightly longer 2.48 seconds at 1632ºC. Increasing alloy size with lump ferroniobium increased the time between addition and a measurable rise in alloy concentration in the melt.

Overall, time required to melt the steel shell and transport the alloy to the sample position was decreased by increasing the steel bath temperature, increasing stirring power and by increasing the surface area to volume ratio of the alloy. Stirring power (for a bath of fixed depth) increases with argon flow rate and steel bath temperature. Surface area to volume ratio increases as the alloy diameter is reduced.

3.2. EXPERIMENTAL CONCLUSIONS

Natural convection (experiments 5, 8, 17, 20) was sufficient to partially mix alloys but was not sufficient to reach homogenization within the experimental period. Argon stirring with 4.1 to 10.5 liters per minute (or stirring power from 290 to 738 Watts per ton) was sufficient to homogenize the Class I alloys and Class II granular ferroniobium. This range of stirring did not homogenize ferroniobium lump additions, which only approached one third to just over one half of the alloy aim in the experimental time.

Increasing stirring power increased alloy transfer rates and shortens mixing times. Ferroniobium is very slow to dissolve, exhibiting very low specific alloy transfer rates. The lowest transfer rate for lump ferroniobium (experiment 25: 10-mm – 313 W/T) was 18.7 times slower than the slowest Class I alloy (experiment 4: 30-mm FeMn – 300 W/T), while the highest ferroniobium transfer rate (experiment 28: 25-mm – 710 W/T) was 14.7 times slower than the fastest solid Class I alloy (experiment 10: nickel pellet – 720 W/T). The observed area specific alloy transfer rates were similar to values published by Gourtsoyannis, Guthrie, and Ratz.[197] Very small Class II alloys, like granular ferroniobium, would likely be required for continuous steel making.

The difference between low and high stirring power experiments for lump ferroniobium was dramatic (Figure 3.8). This can be illustrated with the initial alloy transfer rates. Doubling the alloy size from 10 to 20 mm resulted in a 40% decrease in alloy transfer rate at low stirring. Increasing the stirring power from 313 to 703 W/T for 10 mm ferroniobium resulted in a 350% increase in alloy transfer rate. The higher stirring rates may prevent alloy agglomeration or break-up agglomerated particles.

Nickel and tin had higher alloy transfer rates than ferromanganese. Subsequent modeling (Section 3.2.2) indicated that ferromanganese may follow route 3, where the alloy only partially melts and a second steel shell forms. In this case, there would be less liquid alloy available to transfer to the bulk steel than for route 1 (where the alloy is fully molten). In addition, manganese is more likely to react with dissolved oxygen that nickel. A manganese oxide layer on the alloy surface could slow the transfer of manganese into the melt.

Higher ladle temperatures and increased stirring power shortened the time between alloy addition and the rise in measured alloy concentration. Modeling (Section 3.2.1) indicated that increasing temperature reduces the length of the steel shell period but model results were insensitive to steel velocity. With the exception of experiment 15, the model predicted steel shell period was shorter than the extrapolated time required for the shell to melt and alloy to reach the sample position by a factor of 1.4 to 6.5 (Table 3.6). This would indicate that the transport of liquid alloy to the sample position is as important as the steel shell period and/or that the steel shell model underestimates the steel shell period.

3.3. SPREADSHEET MODEL RESULTS

A theoretically based spreadsheet model was developed to help understand and explain the differences in mixing with the different types and forms of alloy additions. The experimental results were used to validate the model. The theory and construction of the model is detailed in Section 2.4.

The solidification temperature of the steel melt, in ºC, was approximated using equation 3.1, where the terms inside the parentheses represent the weight percent of each element in the melt.[198]

$$T = 1537 - 73.1(\%C) - 2.5(\%Al) - 1.5(\%Cr) - 4.0(\%Mn) - 3.5(\%Ni) - 14(\%Si) \quad (3.1)$$

Unless otherwise stated, solid alloy additions were assumed to be spherical with an initial temperature of 300 K, falling 0.2 meters into an upward steel flow with a velocity magnitude corresponding to the average ladle velocity from the CFD model. This average velocity is shown in Table 3.7 along with CFD computed maximum steel velocity and the argon flow rate dependent temperature loss rate. Velocities were generated by fitting curves to results taken from the CFD model (Section 2.3.2), while temperature loss rates were obtained by fitting a curve to experimental measurements.

Table 3.7. Steel Velocity and Heat Loss Rates Utilized in Spreadsheet Model

Argon Flow Rate	Average Steel Melt Velocity	Maximum Steel Melt Velocity	Temperature Loss Rate	Argon Flow Rate	Average Steel Melt Velocity	Maximum Steel Melt Velocity	Temperature Loss Rate
lpm	m/s	m/s	ºC/s	lpm	m/s	m/s	ºC/s
4	0.037	0.240	1.23	6.7	0.072	0.350	1.44
4.4	0.042	0.259	1.26	7.1	0.076	0.363	1.47
4.8	0.048	0.276	1.29	7.5	0.081	0.376	1.50
5.2	0.053	0.293	1.32	7.9	0.085	0.387	1.54
5.6	0.058	0.310	1.35	8.3	0.090	0.398	1.57
6	0.063	0.325	1.38	9.3	0.100	0.422	1.66
6.2	0.066	0.332	1.40	9.5	0.102	0.426	1.68
6.4	0.068	0.340	1.41	9.7	0.104	0.430	1.70
6.6	0.070	0.347	1.43	9.9	0.105	0.433	1.72

3.3.1. Constant Temperature Steel Shell Model Results. For the purpose of comparison, several alloys compositions/sizes, melt temperatures, argon flow rates, alloy preheats, model parameters, and alloy properties were evaluated with the steel shell model, using constant ladle temperatures between 1585ºC (1858 K) and 1620ºC (1893 K). Constant melt temperature is more representative of industrial scale ladles and continuous steelmaking, especially over the short time intervals evaluated. Spherical 20-mm diameter nickel was chosen as the basis for comparison due to its well defined thermo-physical properties. An alloy size of 20-mm was chosen as a compromise between industrial practice and the recommendations of Lee et al. and Argyropoulos et al.[199, 200]

From the model for a given size, alloy composition has the greatest influence on steel shell formation and melting. Tin has a low melting point (232ºC) and latent heat of fusion (about one fifth that of nickel), which results in a very thin shell and short melting time. Tin-steel composite particle diameters were only 3.3% (10 mm) to 3.4% (20 mm) larger than the starting diameter, while nickel under the same conditions increased, on average 42% (Table 3.8). The thin shell on the 10-mm tin addition melts rapidly, 0.03 seconds after alloy addition at 1600ºC (1873 K). For comparison, a10-mm nickel addition would require 0.88 seconds for the steel shell to melt after alloy addition. Doubling the tin addition size to 20-mm, resulted in only a small percentage increase in shell thickness but a 2.9 fold increase in melting time. Nickel, ferroniobium, and low carbon ferromanganese melting time increased by 2.6, 2.8, and 2.9 times, respectively when diameter increased from 10 to 20-mm.

Ferroniobium's low heat capacity and ferromanganese's low thermal conductivity, lead to a smaller temperature difference between the shell and alloy particle, which reduces the maximum size of the shell and shortens the shell period, relative to nickel. Results in Table 3.8, do not account for the reaction of the liquid alloy with steel on the inside of the shell, which could shorten the melting time for alloys through formation of a eutectic with iron or exothermic heats of dissolution (see Table 1.3).

Table 3.8. Steel Shell Model Output Comparing Ferroniobium, Low Carbon Ferromanganese, Tin, and Nickel

Alloy	Alloy Diameter – mm	Argon flow Rate – liters per minute	Ladle Temperature - K	Maximum Calculated Alloy Particle Diameter - mm	Model Shell Period - seconds	Temperature Alloy Center – Percent of Melting Temperature*
Ferroniobium	10	5	1873	12.41	0.55	99.0%
Ferroniobium	20	5	1873	24.97	1.52	96.0%
Ferroniobium	10	5	1893	12.32	0.47	98.0%
Ferroniobium	20	5	1893	24.79	1.29	93.5%
Ferroniobium	20	10	1893	24.80	1.29	93.5%
Low carbon ferromanganese	10	5	1873	14.42	0.67	21.0%
Low carbon ferromanganese	20	5	1873	29.22	1.90	20.4%
Low carbon ferromanganese	10	5	1893	14.28	0.56	20.5%
Low carbon ferromanganese	20	5	1893	28.94	1.61	20.3%
Low carbon ferromanganese	20	10	1893	28.94	1.61	20.3%
Tin	10	5	1873	10.33	0.03	59.4%
Tin	20	5	1893	20.67	0.08	59.5%
Nickel	10	5	1873	14.07	0.88	100%
Nickel	20	5	1873	28.53	2.30	97.9%
Nickel	10	5	1893	13.94	0.76	100%
Nickel	20	5	1893	28.26	1.97	93.7%
Nickel	20	10	1893	28.27	1.96	93.5%

*when steel shell just disappears

In Table 3.9, center temperature is the temperature at the center of the alloy particle when the steel shell just melts. This temperature is expressed as a percent of the alloys melting temperature. Center temperature gives an indication of the heat transport within the solid alloy. Thus ferromanganese, which only reaches 20.4% (20 mm 1873 K – 5 lpm), shows low thermal transport within the alloy particle. Tin is more effective at transporting heat than ferromanganese, reaching 59.5% (20 mm 1873 K – 5 lpm), while nickel has the highest transport rate of the three reaching 97.9% (20 mm 1873 K – 5 lpm). These results indicate that the Class I alloy additions may not following route 1(full

melting of the alloy prior to the steel shell melting) as assumed; this is likely due to excessive superheat.

Table 3.9. Steel Shell Model Output for Nickel Showing Variation with Ladle Temperature (no heat loss from ladle), Alloy Size, and Argon Flow Rate

Initial Alloy Diameter – mm	Argon Flow Rate – liters per minute	Ladle Temperature – K	Maximum Calculated Alloy Particle Diameter - mm	Model Shell Period - seconds	Temperature Alloy Center – Percent of Melting Temperature
5	10	1873	6.95	0.31	100%
10	10	1873	14.1	0.88	100%
15	10	1873	21.3	1.55	100%
20	10	1873	28.5	2.30	97.9%
25	10	1873	35.8	3.10	94.2%
30	10	1873	43.1	3.92	90.4%
20	10	1858	28.75	2.63	100%
20	10	1863	28.68	2.51	99.6%
20	10	1868	28.61	2.40	98.8%
20	10	1873	28.54	2.30	97.9%
20	10	1878	28.47	2.21	96.9%
20	10	1883	28.40	2.13	95.8%
20	10	1888	28.34	2.04	94.7%
20	10	1893	28.27	1.96	93.5%
20	4	1873	28.528	2.30	97.9%
20	5	1873	28.530	2.30	97.9%
20	6	1873	28.532	2.30	97.9%
20	7	1873	28.534	2.30	97.9%
20	8	1873	28.536	2.30	97.9%
20	9	1873	28.538	2.30	97.9%
20	10	1873	28.539	2.30	97.9%

Model results indicate that short shell melting times are favored by low alloy melting temperature, smaller alloy additions, higher ladle temperatures, and low alloy thermal conductivity. Short shell melting times can result in relatively low temperatures at the alloy core when the alloy is exposed to the melt (Table 3.8). This may lead low carbon ferromanganese to follow dissolution route 2 as depicted in Figure 1.5. Plots for

the temperature at the center of nickel spheres, at three ladle temperatures, are shown in Figure 3.11.

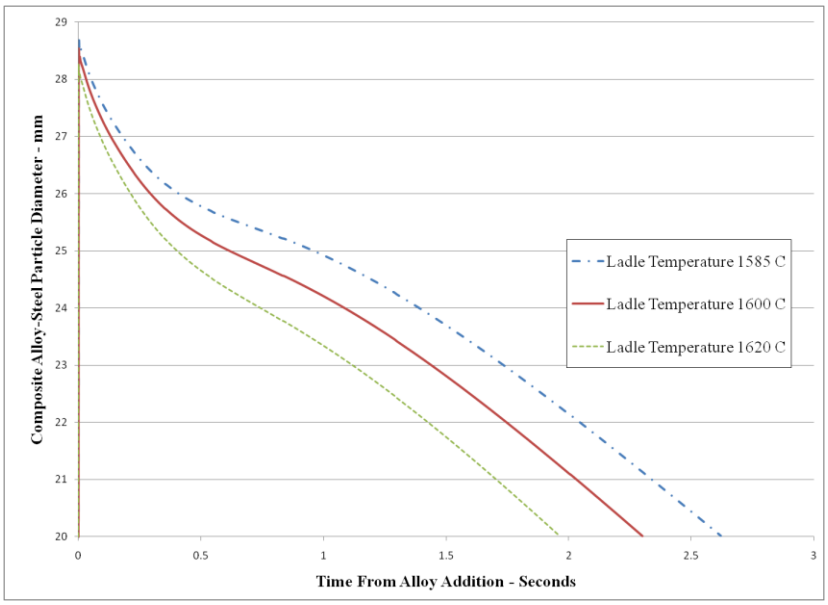

Figure 3.11. Steel Shell Model Output Showing Steel Shell-Alloy Composite Diameter versus Time from Addition of a 20-mm Diameter Nickel Particle (added gravimetrically) into a Ladle of Steel with a Constant Steel Bath Temperatures of 1585, 1600, and 1620°C and 10 lpm Argon Flow Rate

For a given alloy, the model suggests that alloy size and ladle temperature are much more critical than argon flow rate in determining the length of the shell period (Table 3.9). In terms of size, 5 and 10-mm nickel additions melted 86.6% and 32.5% faster than 20-mm additions, while 25 and 30-mm additions melted 34.5% and 70.2% slower. As for temperature, for every 5 degree increase in steel melt temperature, the steel shell period was reduced by about 4% (the effect is more pronounced at lower temperatures), thus increasing the steel melt temperature from 1600ºC (1873 K) to 1620ºC (1893 K) decreased the melting time by 14.7%; this result does not account for changes in steel melt viscosity or thermal diffusivity. The maximum shell diameter for nickel is between 28 and 29 mm for ladle temperatures between 1585 and 1620°C. The shell melts much more rapidly at 1620°C compared to 1600 and 1585°C, as illustrated in Figure 3.11.

Reducing the liquid steel temperature increases the alloy center temperature, as there is more time to transfer heat into the solid before the steel shell melts. Nickel (20-mm) immersed in a ladle at 1585ºC would reach 1455°C (100% of melting temperature) before the end of the shell period. The same nickel alloy spheres at 1600 and 1620ºC would be free of the steel shell before the center of the particle reached 100% of the alloy melting temperature, as shown in Figure 3.12.

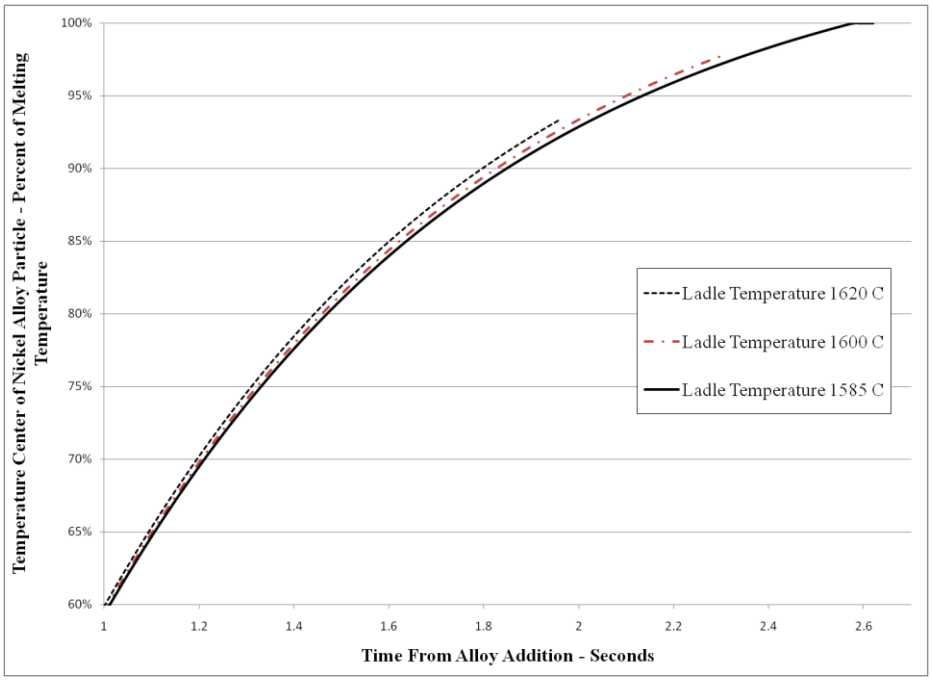

Figure 3.12. Steel Shell Model Output Showing Temperature at the Center a 20-mm Nickel Alloy Particle after Alloy is Submerged in a Ladle of Steel with Constant Steel Bath Temperatures of 1585, 1600, and 1620°C and 10 lpm argon flow rate. Center Temperature is expresses as a Percent of the Melting Temperature of the Alloy (1728 K). Model Stops at End of Steel Shell Period

Unlike alloy size or melt temperature, argon flow rate and its associated steel velocity, had very little effect on the calculated steel shell period or maximum particle diameter. More than doubling the argon flow rate (4 lpm to 10 lpm) increased the steel velocity in the model, from 0.37 to 1.06 m/s, yet, as seen in Table 3.9, the values for steel shell period and maximum particle diameter are unchanged. Zhang and Oeters also noted that slip velocity only had a weak effect on total melting time of alloy particles.[201]

Within the steel shell model, increasing the argon flow rate from 4 to 10 lpm increased the initial convective heat transfer coefficient by 1.58% (for 20 mm nickel at 1873K). This difference was only 0.20% at 0.1 seconds. There was no significant difference in the heat transfer coefficient after 0.3 seconds. The average convective heat transfer coefficient from alloy entry until the steel shell melted was 62,667 $W/m^2 \cdot K$ at 4 lpm, which increased to 62,757 $W/m^2 \cdot K$ at 10 lpm. When temperature loss is included in the shell model, increases in convective heat transfer associated with increasing argon flow rate is somewhat offset by the increase in melt temperature loss.

Alloy preheating could speed alloy homogenization by shortening the steel shell period. To quantify this reduction in steel shell period, the steel shell model was run for 20-mm nickel (10 lpm and 1873 K) with the alloy entering the melt at 300, 500 and 700 K. Increasing the alloy particle temperature from 300 to 500 K (227°C) resulted in a 0.24 second or 10% reduction in the steel shell period, as shown in Table 3.10. Increasing the alloy temperature from 300 to 700 K (427°C) resulted in a 0.53 second or 23% reduction in the steel shell period. Based on the model, preheating 20-mm nickel to 500 K is equivalent to a 15 K increase in ladle temperature in terms of reducing the steel shell period (0.24 versus 0.26 seconds).

Table 3.10. Steel Shell Model Output for 20 mm-Nickel Particles with Initial Alloy Temperatures of 300, 500 and 700 K to Show Effect of Preheating Alloy

Initial Alloy Temperature – K	Alloy Diameter – mm	Argon flow Rate – liters per minute	Ladle Temperature - K	Maximum Calculated Alloy Particle Diameter - mm	Model Shell Period - seconds	Temperature Alloy Center – Percent of Melting Temperature*
300	20	10	1873	28.54	2.30	97.9%
500	20	10	1873	27.64	2.06	96.0%
700	20	10	1873	26.67	1.77	93.5%

Uncertainties in model inputs were explored by varying the heat transfer coefficient, alloy thermal conductivity and alloy heat capacity. Whitaker suggests that

heat transfer correlations for spheres are generally accurate to within ±30%, so heat transfer coefficient was the first of these parameters investigated.[202]

The baseline average convective heat transfer coefficient from alloy addition to complete shell melting was 62,760 $W/m^2 \cdot K$. Increasing the convective heat transfer coefficient by 10% decreased the maximum shell size by 0.28% and decreased the shell period by 9.6%, (Table 3.11). Increasing the heat transfer coefficient by 10% also decreased the alloy center temperature by 2.7% at the end of the shell period. A 20% increase in heat transfer coefficient reduced the maximum shell diameter by 0.59%, the shell period by 17.8%, and the alloy center temperature by 5.4%.

Decreasing the heat transfer coefficient by 10 and 20% increased the shell period by 12.2 and 26.5%, respectively. In addition, reducing the heat transfer coefficient resulted in complete preheating of the alloy particle before the steel shell melted. This is shown in Table 3.11, where the temperature at the center of the alloy particle reaches 100% of the alloy melting temperature.

Table 3.11. Effect of Convective Heat Transfer Coefficient (h), on Steel Shell Model Output for 20 mm-nickel Particles

Convective Heat Transfer Coefficient – W/m^2K	Initial Alloy Diameter – mm	Argon Flow Rate – liters per minute	Ladle Temperature - K	Maximum Calculated Alloy Particle Diameter - mm	Model Shell Period - seconds	Temperature Alloy Center – Percent of Melting Temperature
(+20%)	20	5	1873	28.36	1.89	92.6%
(+10%)	20	5	1873	28.45	2.08	95.3%
(±0%)	20	5	1873	28.53	2.30	97.9%
(-10%)	20	5	1873	28.60	2.58	100%
(-20%)	20	5	1873	28.65	2.91	100%

One of the model assumptions was that the alloy particles entered the steel melt in an upward flow. The flow velocity was assumed to be the magnitude of the average ladle velocity given in Table 3.7. The model was reconfigured so that the alloy would enter a downward flowing region with a velocity equal in magnitude to the ladle average

velocity. The maximum particle diameter decreased insignificantly (0.07%), while the steel shell period was increased by 0.01 seconds (0.4%) when the flow direction was reversed (Table 3.12). This again shows that the model is not sensitive to velocity within the chosen argon flow rate range.

Table 3.12. Effect of Direction of Steel Flow, Alloy Thermal Conductivity, and Alloy Heat Capacity on Steel Shell Model Output for 20 mm-nickel Particles

Varied Parameter	Initial Alloy Diameter – mm	Argon Flow Rate – liters per minute	Ladle Temperature – K	Maximum Calculated Alloy Particle Diameter - mm	Model Shell Period - seconds	Temperature Alloy Center – Percent of Melting Temperature
Downward flow	20	5*	1873	28.51	2.31	97.9%
Thermal Conductivity +10%	20	5	1873	28.45	2.31	99.8%
Thermal Conductivity -10%	20	5	1873	28.62	2.29	95.3%
Heat Capacity +10%	20	5	1873	29.16	2.46	97.0%
Heat Capacity - 10%	20	5	1873	27.88	2.14	98.7%

*Average steel melt velocity equivalent to that generated by 5 liters per minute argon, but applied in opposite direction.

Alloy properties vary with chemistry, which for ferroalloys can vary from batch to batch, thus changes in thermal conductivity and heat capacity were evaluated (Table 3.12. A 10% increase in alloy thermal conductivity slightly increased the maximum shell thickness (0.3%) and shell period by 0.01 seconds. An increased alloy thermal conductivity does reduce internal thermal gradients, increasing the center temperature from 97.9% to 99.8%. Decreasing the alloy thermal conductivity showed changes similar in magnitude to increasing the conductivity, but with a reduced shell thickness, decreased shell period, and larger internal thermal gradients. Alloy heat capacity changes showed

greater impact. Increasing alloy heat capacity by 10% increased maximum diameter by 2.2% and shell period by 7%. Decreasing alloy heat capacity by 10% had the opposite effect.

The steel shell model evaluation showed that the steel shell period increases with increasing alloy size, decreases with increasing ladle temperature and varies considerably with alloy composition. In addition, the model is not sensitive to steel velocity, but of more interest is the calculated temperature at the center of the alloy when the steel shell melts. These results indicate that for Class I alloys, the dissolution route may not be route 1 (Figure 1.5) as assumed.

3.3.2. Shell Model Results for Experimental Conditions. Having evaluated the steel shell model for hypothetical conditions, the model was then configured to evaluate experimental conditions. The most significant difference between the model and the experimental conditions is that the steel melt temperature decreases with time in the experimental model. The temperature loss rate was taken from Table 3.7. Computed steel shell melting times were then used in the three-tanking mixing model (Section 3.2.2) or dissolution model (Section 3.2.4).

The maximum alloy diameter and shell period were computed, with temperature losses, for nickel, ferromanganese and ferroniobium under experimental conditions. Only liquid tin experiments were modeled, so no shell period was considered for tin. Nickel cathode was assumed to be a sphere. The result is a surface area to volume ratio that is 32 percent less than the actual surface area to volume ratio for nickel cathode. This should over-estimate the length of the shell period.

Model results using experimental conditions showed the same trends seen in the hypothetical simulations from Section 3.2.1. Ferroniobium had the shortest shell period, ranging from 0.49 seconds at 10 mm to 1.38 seconds for 20 mm (Table 3.13). Nickel pellets had the next shortest steel shell period at 1.10 to 1.47 seconds (Table 3.14). A modest increase in ladle temperature from 1893 to 1916 K (~1%) decreased the steel shell period of nickel pellets by nearly 20% (1.32 to 1.10 seconds) at the higher argon flow rate. Ferromanganese had steel shell periods of 1.56 and 1.75 seconds at 20 mm diameter. Nickel cathode steel shell period ranged from 1.85 to 2.55 seconds with the shortest time corresponding to the highest ladle temperature.

Table 3.13. Computed Ferroniobium Maximum Alloy-Shell Diameter, Shell Existence Time, and Alloy Center Temperature for Experimental Conditions

Experiment	Alloy Diameter – mm	Argon flow Rate – liters per minute	Initial Ladle Temperature - K	Maximum Calculated Alloy Particle diameter - mm	Model Shell Period - seconds	Temperature Alloy Center – Percent of Melting Temperature
25 - Nb-1	10	4.4	1905	12.34	0.49	99.2%
26 - Nb-2	10	9.9	1903	12.35	0.49	99.4%
27 - Nb-3	15	4.5	1898	18.62	0.94	97.5%
28 - Nb-4	15	10.0	1905	18.58	0.89	96.5%
29 - Nb-5	20	5.1	1901	24.86	1.38	94.1%
30 - Nb-6	20	10.4	1904	24.83	1.35	93.6%

Table 3.14. Computed Maximum Alloy-Shell Diameter, Shell Existence Time, and Alloy Center Temperature for Nickel and ferromanganese Under Experimental Conditions

Experiment	Alloy Form	Alloy Diameter – mm	Argon flow Rate – liters per minute	Initial Ladle Temperature - K	Maximum Calculated Alloy Particle diameter – mm	Model Shell Period - seconds	Temperature Alloy Center – Percent of Melting Temperature
9 - Ni-1	Pellet	13.5	4.7	1876	19.21	1.47	105.4%
10 - Ni-2	Pellet	13.5	10.2	1893	19.35	1.32	102.9%
11 - Ni-3	Cathode	22	4.7	1891	31.40	2.55	95.8%
12 - Ni-4	Cathode	22	10.5	1893	31.38	2.52	95.3%
13 - Ni-5	Pellet	13.5	4.7	1915	18.87	1.11	99.2%
14 - Ni-6	Pellet	13.5	9.6	1916	18.87	1.10	99.2%
15 - Ni-7	Cathode	22	5.1	1916	31.05	2.12	88.3%
16 - Ni-8	Cathode	22	10.5	1935	30.81	1.85	82.3%
6 - Mn-1	Spheroid	20	4.7	1915	28.86	1.56	20.3%
7 - Mn-2	Spheroid	20	10.0	1898	29.09	1.75	20.3%

The assumption of route 1 behavior for ferromanganese is not warranted. In both experiments 6 and 7, the alloy center temperature only reaches 20.3% of the alloy melting temperature (Table 3.14). This corresponds to a temperature just slightly above the initial temperature (or 300.03 K) and could lead to dissolution route 3.

Nickel pellets at the lower furnace tap temperature (experiment 9 and 10) show a center temperature above the alloy melting point. The alloy in this case would likely

follow dissolution route 1. Nickel pellets at the higher tap temperature may follow a hybrid of route 2 and 3, where alloy would melt under the steel shell but the remaining solid would be at a high enough temperature to prevent the formation of a new steel shell. Based on actual shape, nickel cathode would likely follow route 1, even though the model indicates temperatures at the center of 82.3 to 95.8% of the alloy melting temperature.

3.3.3. Combined Shell-Three Tank Class I Alloy Results. Having calculated the steel shell period, mixing of Class I alloys was considered. This was a two-step process of first establishing general model values and then secondly establishing specific experimental parameters. Liquid tin was considered separately from ferromanganese and nickel because it did not have a steel shell period and could thus use a two tank model.

An initial evaluation of the three tank model was performed by manually adjusting the three tank model inputs to match experimental results from experiments 6, 7, 9, 10, 11, 12, 13, 14, 15, and 16. The inputs adjusted were the alloy zone fraction, dead zone fraction, and volume exchange rates. Based on results of the initial evaluation, the alloy zone fraction was fixed at one tenth of the dead zone fraction. The dead zone fraction value was fixed at 0.089 for the lowest argon flow rates (4.7 to 5.1 lpm) and 0.082 for the high argon flow rate (9.6 to 10.5 lpm) experiments. Volume exchange rates (alloy to dead and dead to mixing zone) were left as variables for a second pass through all of the experiments.

With the alloy zone and dead zone fractions fixed, the alloy zone to dead zone and dead zone to mixing zone exchange rates were found. This was accomplished by minimizing the overall difference between experimental data points and their corresponding model values. Within the spreadsheet, the model value for alloy concentration at the time of the alloy sample was subtracted from the corresponding experimental value. These differences were then summed. The built in solver was utilized to bring the summed value to zero by simultaneously adjusting the exchange rates.

The alloy zone to dead zone and dead zone to mixing zone exchange rates ranged from 0.0054 to 0.796 and 0.0084 to 0.0750, respectively (Table 3.15). Predicted 95% mixing times ranged from 5.9 to 56.1 seconds and are shown with a corresponding measured mixing time range (time of sample just before and just after reaching 95%

mixed) in Table 3.15. For nickel experiments, the nominal alloy aim level was 0.35% and 0.30% for manganese.

Table 3.15. Computed and Measured 95% Mixing Time and Model Parameters for Nickel and Ferromanganese

Experiment	Alloy Form	Argon flow Rate – liters per minute	Initial Temperature & (loss rate) – K & (K/s)	Computed 95% Mixing time – seconds	Sample Time Just Before and after Reaching 95%	Alloy Volume Exchange Rate Fraction	Volume Exchange Rate Fraction
Ni-1	Pellet	4.7	1876 (1.28)	23.4	13 to 20	0.0124	0.0750
Ni-2	Pellet	10.2	1893 (1.75)	13.9	14 to 21	0.0502	0.0143
Ni-3	Cathode	4.7	1891 (1.28)	56.1	34 to 41	0.0054	0.0170
Ni-4	Cathode	10.5	1893 (1.78)	20.2	5 to 16	0.0108	0.0699
Ni-5	Pellet	4.7	1915 (1.28)	17.1	22 to 30	0.0796	0.0154
Ni-6	Pellet	9.6	1916 (1.69)	5.9	6 to 12	0.0541	0.0630
Ni-7	Cathode	5.1	1916 (1.31)	31.0	26 to 34	0.0097	0.0400
Ni-8	Cathode	10.5	1935 (1.78)	11.5	14 to 21	0.0295	0.0296
Mn-1	Spheroid	4.7	1915 (1.28)	34.6	23 to 29	0.0205	0.0084
Mn-2	Spheroid	10.0	1898 (1.73)	15.4	10 to 15	0.0252	0.0715

In experiments Ni-4 and Ni-6 the sampled alloy concentration peaked above the final homogenized alloy concentration (Figures 3.16 and 3.18). While in Ni-5, Ni-8, and Mn-1, the alloy concentration rose then fell, before rising to a homogenized value (Figures 3.17, 3.20, and 3.22). The combined shell-three tank model was not designed to reproduce this type of behavior. Instead, the model produces a continuous concentration curve which rises toward the homogenized value. In addition, the combined three-tank model has limited ability to adjust for the time required for the alloy to be transported to the sampling location after the steel shell melts. The alloy delay time extrapolated from experimental data in Section 3.1.3.4 shows that this time can be significantly longer than the calculated steel shell period.

As a result of these model limitations, the computed 95% mixing time falls outside of the experimental 95% mixing times for eight experiments. The difference between measured and modeled mixing times ranged from 0.1 seconds for Ni-2 and Ni-6

to more than 15 seconds for Ni-3. This difference represents a departure of 0.6, 1.1 and 40.3% from the mean of the mixing time range.

Unlike the alloy transfer rate approach, the three-tank model is able to represent experiments where the alloy concentration jumps immediately to a peak value without an intermediate point to fit a line through. Graphically the model does a good job of approximating the experimental behavior of the nickel and ferromanganese experiments.

The largest difference between measured and modeled mixing time is seen in experiments Ni-3 and Ni-4, where the shell period and/or initial alloy mixing is underestimated and there is a sudden increase in measured alloy concentration. Reducing the shell model convective-heat transfer coefficient by 20% has a very limited effect, on the initial shell period, as can be seen in Figure 3.13, where both the standard and modified models are plotted.

The Ni-1 model alloy concentration initially rises more rapidly than the experimental data but is at a lower concentration than the experiment from about 10 to 30 seconds (Figure 3.13). The difference between the experiment and model is due to the recirculation of an alloy rich region in the ladle. Model agreement improves as the alloy rich region is homogenized, thus the model aligns with the final three experimental data points.

Regardless of model shortcomings, all of the Class I alloys in the experiments presented, are approaching homogenization within one minute, which should be adequate for continuous steel making. As reported in Section 3.1.4, argon stirring (4.7 lpm minimum) of low carbon ferromanganese resulted in alloy levels approaching homogenization within the experimental period, with 20 mm spheroids homogenizing about 50% faster than 30 mm. However, natural convection within the same experimental vessel was insufficient to homogenize ferromanganese or nickel.

Although experimental conditions (temperature and argon flow rate) were not reproduced precisely from heat to heat, the results do provide insight into the general effect of alloy, argon flow rate, and melt temperature.

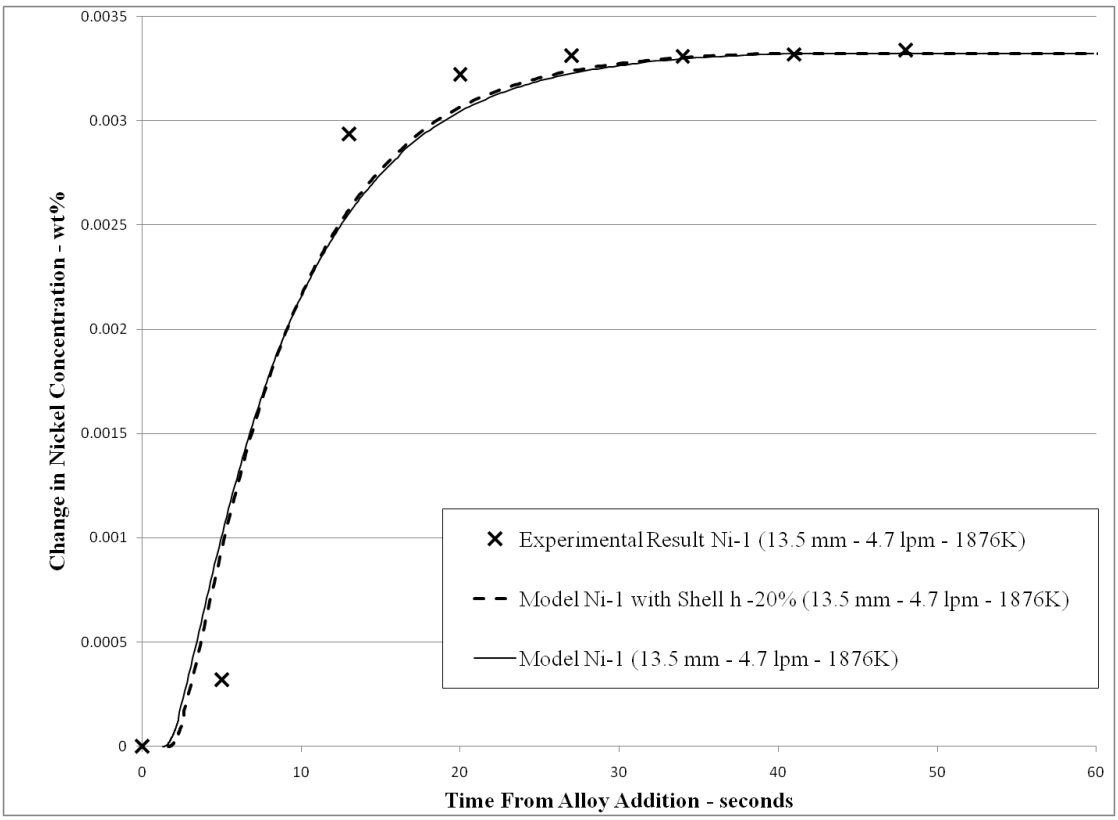

Figure 3.13. Change in Nickel Content in Liquid Steel after Making 0.35% Ni Addition of Nickel Pellets with Argon Stirring of 4.7 lpm and Initial Ladle Temperature of 1876 K. Points are Experimentally Measured for Experiment Ni-1. Solid Line is Shell-Three Tank Model Output. Dashed Line is Shell-Three Tank Model Output with Heat Transfer Coefficient Reduced 20 %

Table 3.16. Comparison of Experimental Conditions and Results for Ferromanganese and Nickel

	Model 95% Mixing Time - s	Argon Flow Rate - lpm	Initial Ladle Temperature-K	Stirring Power – W/T	Model Shell Period - s
Ni-2 13.5-mm spherical pellet	13.9	10.2	1893	720	1.32 s
Mn-2 20-mm spheroid	15.4	10.0	1898	708	1.75 s
Ni-5 13.5-mm spherical pellet	17.1	4.7	1915	336	1.11 s
Ni-4 cathode rectangular prism	20.2	10.5	1893	741	2.52 s
Mn-1 20-mm spheroid	34.6	4.7	1915	336	1.56 s

Selected nickel and ferromanganese experiments were compared to evaluate mixing times, stirring power and alloy size (Table 3.16). Experiment Ni-4 (nickel cathode – 740 W/T; Figure 3.4) was similar to Mn-2 (20-mm ferromanganese – 708 W/T; Figure 3.2). Experimentally, Ni-2 and Mn-2 reached 95% mixed between 5 and 16 and 10 and 15 seconds, respectively. In spite of a larger surface area (and higher alloy transfer rate of 11.97 versus 10.53 g/s), the nickel cathode model is slower to reach 95% mixed by nearly 5 seconds. The model steel shell period for Mn-2 is 0.77 seconds shorter than Ni-4 but delay before alloy is detected from Table 3.6 shows that alloy appeared in the ferromanganese experiment 1.32 seconds earlier than the nickel experiment.

Computed mixing times for the smaller nickel pellet experiments (Ni-2 – 13.9 seconds and Ni-5 – 17.1 seconds) fell on either side of ferromanganese experiment Mn-2 (15.4 second). This order is consistent with the stirring power of each experiment, where the highest stirring power had the shortest mixing time. The low stirring power ferromanganese experiment, Mn-1, had the same stirring power as nickel pellet experiment Ni-5 but the ferromanganese computed mixing time was twice as long (34.6 seconds). This could be an indication that the ferromanganese forms a second steel shell while nickel does not, under similar conditions.

The three-tank model result passes very close to the initial data point in experiment Ni-2 (experiment 10) before passing between experimental measurements at 10 seconds. Figure 3.14 shows model output for experiment Ni-2 (dashed line) superimposed on experimental data. The final predicted alloy concentration exceeded the homogenized values seen in the experiment (indicating lower than expected nickel recovery).

The model of experiment Ni-3 (experiment 11) starts slightly above the first three alloy samples, before intersecting the measured value at just over 20 seconds (Figure 3.15). The experimental measurement rises rapidly after 30 seconds, but the model continues to rise steadily. The model in this case overestimated the 95% mixing time due to the sluggish alloy transfer in the first 20 seconds of the experiment.

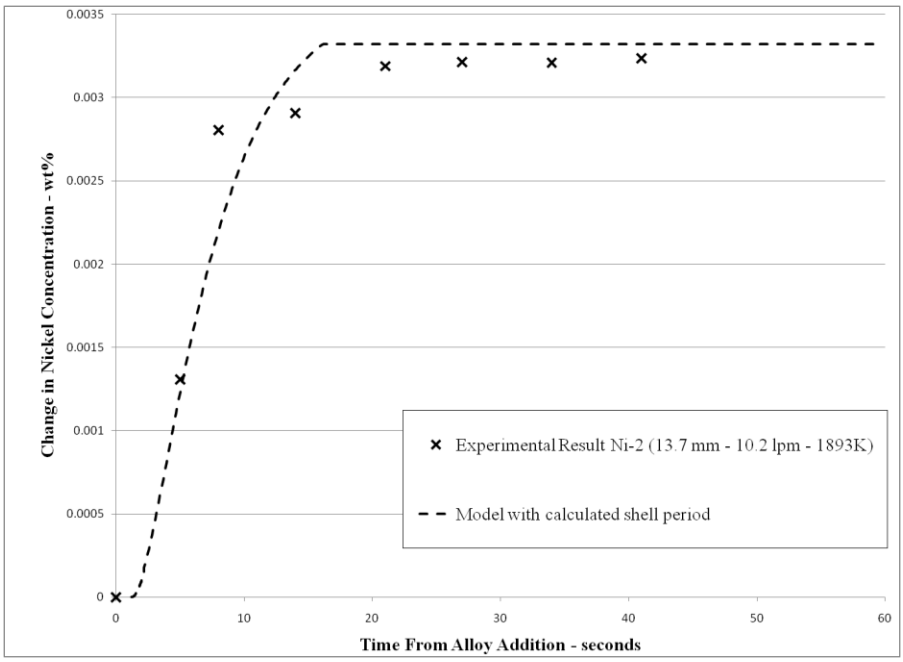

Figure 3.14. Change in Nickel Content in Liquid Steel after Making 0.35% Ni Addition of Nickel Pellets with Argon Stirring of 10.2 lpm and Initial Ladle Temperature of 1893 K. Points are Experimentally Measured for Experiment Ni-2. Dashed Line Is Shell-Three Tank Model Output

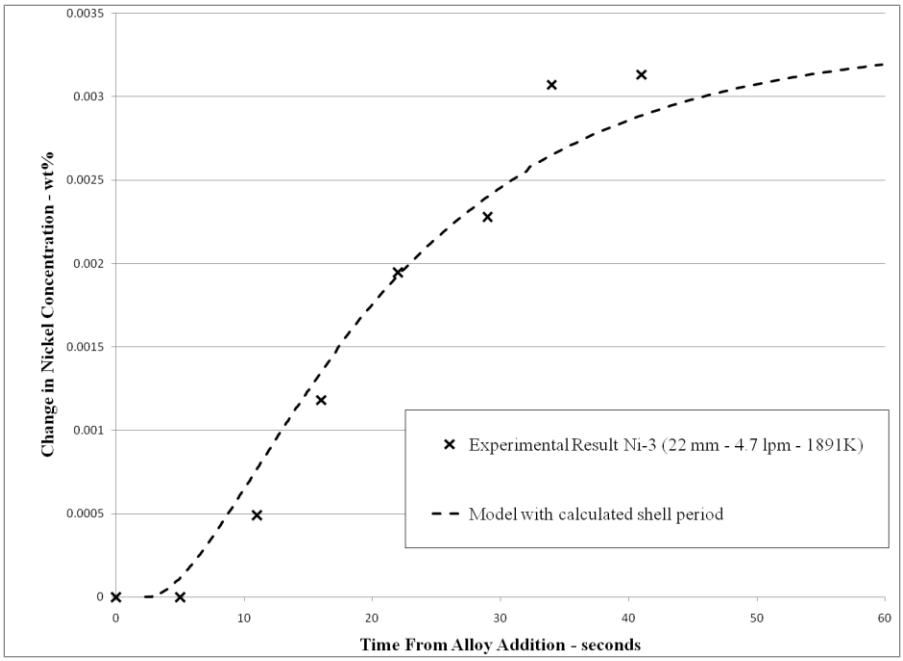

Figure 3.15. Change in Nickel Content in Liquid Steel after Making 0.35% Ni Addition of Nickel Pellets with Argon Stirring of 4.7 lpm and Initial Ladle Temperature of 1891 K. Points Are Experimentally Measured for Experiment Ni-3. Dashed Line Is Shell-Three Tank Model Output

Model output for experiment Ni-4 (experiment 12) very closely approximates the final five experimental data points but shows a lower initial alloy transfer rate than the experiment (Figure 3.16). As a result, the model 95% mixing time is longer than the experimental mixing time by about 10 seconds.

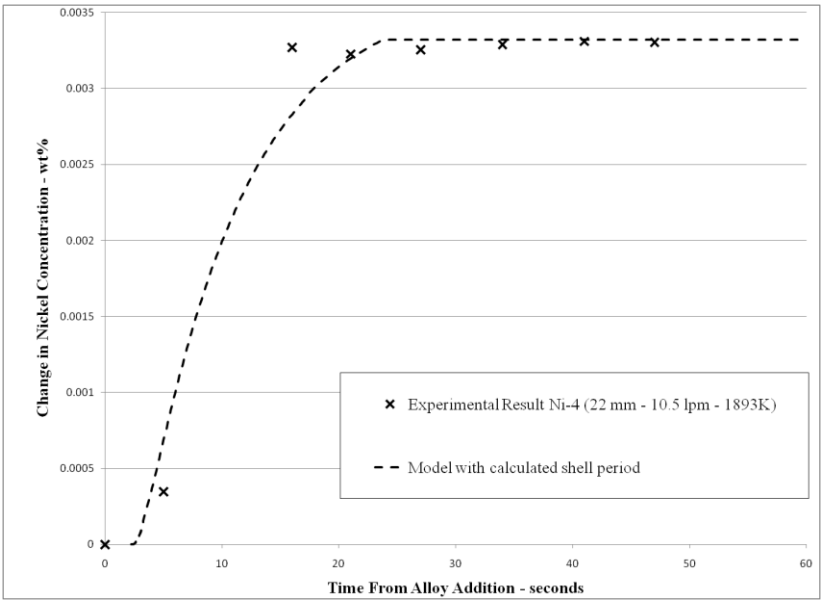

Figure 3.16. Change in Nickel Content in Liquid Steel after Making 0.35% Ni Addition of Nickel Cathode Pieces with Argon Stirring of 10.5 lpm and Initial Ladle Temperature of 1893 K. Points Are Experimentally Measured for Experiment Ni-4. Dashed Line Is Shell-Three Tank Model Output

Model output for experiment Ni-5 (experiment 13) slightly under estimates the initial alloy transfer to the melt (Figure 3.17). Experiment Ni-5 showed a slight dip in nickel concentration just past 20 seconds. The final three data points align with the model. There were not enough data points to establish the initial alloy transfer rate for Ni-6 (experiment 14). The nickel concentration rises rapidly to a near peak value at around 5 seconds (Figure 3.18). The next sample had an alloy concentration above the final homogenized value. The model passes through or very near the first, third, fourth, and sixth data points. The technique of minimizing the difference between model and experimental data results in the model passing between the peak and dip at the second and fifth data point.

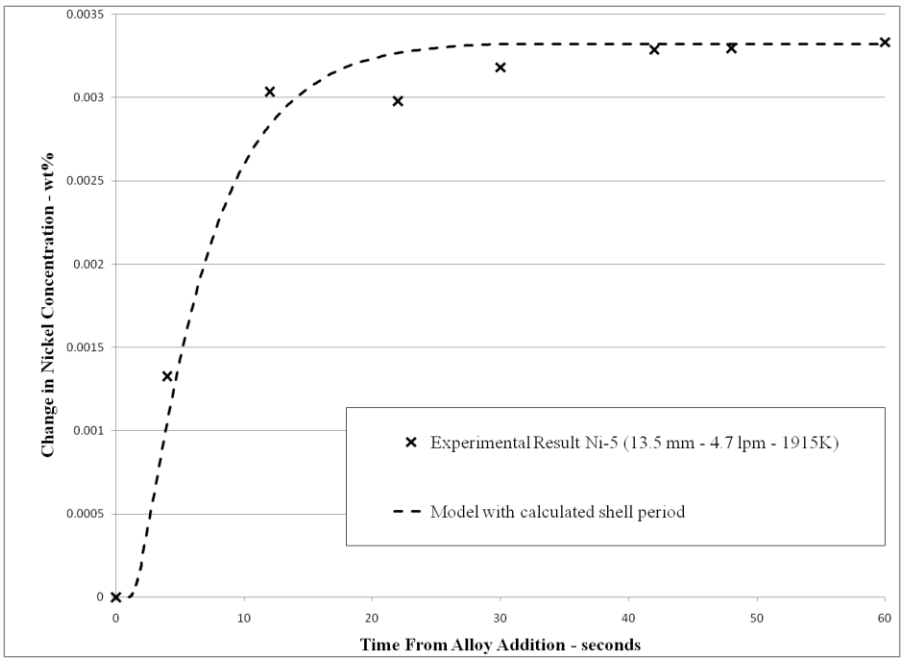

Figure 3.17. Change in Nickel Content in Liquid Steel after Making 0.35% Ni Addition of Nickel Cathode Pieces with Argon Stirring of 4.7 lpm and Initial Ladle Temperature of 1915 K. Points Are Experimentally Measured For Experiment Ni-5. Dashed Line Is Shell-Three Tank Model Output

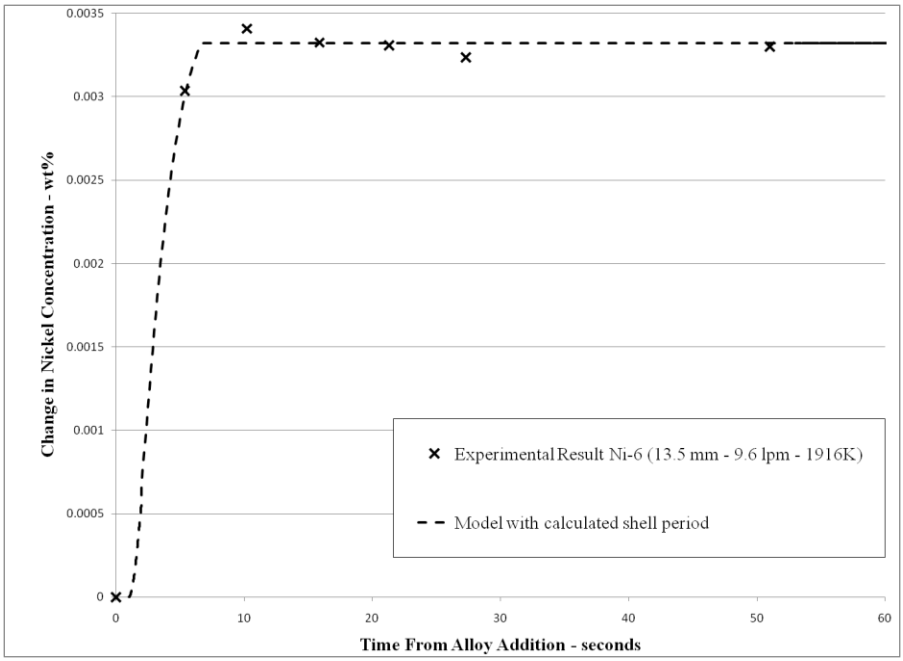

Figure 3.18. Change in Nickel Content in Liquid Steel after Making 0.35% Ni Addition of Nickel Pellets with Argon Stirring of 9.6 lpm and Initial Ladle Temperature of 1916 K. Points Are Experimentally Measured For Experiment Ni-6. Dashed Line Is Shell-Three Tank Model Output

The model output for experiment Ni-7 (experiment 15) very closely approximates the dissolution of the nickel cathode pieces (Figure 3.19). Again the technique for minimizing the difference between model and experiment results in the model initially overestimating alloy transfer to just past 10 seconds. This is followed by a slight underestimation of the alloy concentration for the next three data points. The fixed alloy zone fraction and dead zone fractions used in all the models resulted in a very close match between experimental values and the model for Ni-7. Ni-8 (experiment 16), Figure 3.20, is similar to experiment Ni-2 (Figure 3.14). The model predicted homogenized alloy concentration is higher than the final alloy concentration. This indicates that the nickel addition was either less than the desired amount or alloy recovery was lower than expected.

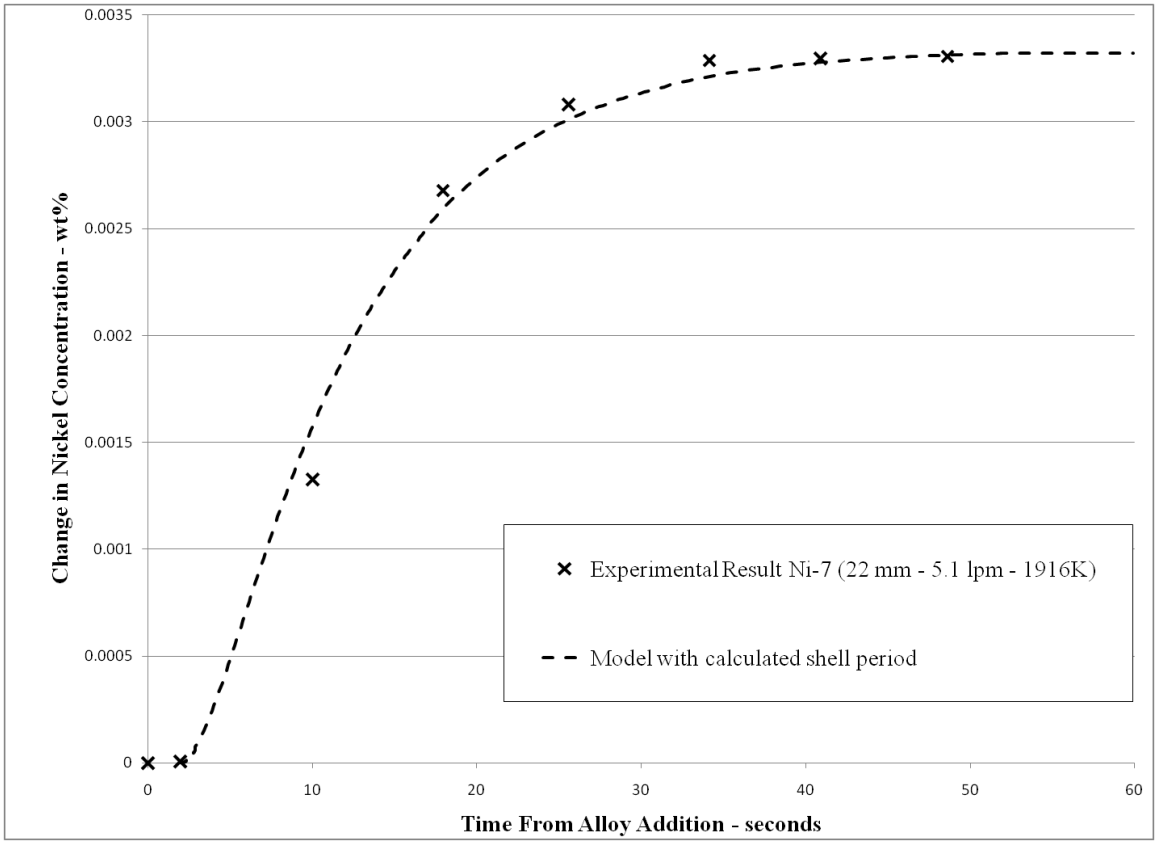

Figure 3.19. Change in Nickel Content in Liquid Steel after Making 0.35% Ni Addition of Nickel Cathode Pieces with Argon Stirring of 5.1 lpm and Initial Ladle Temperature of 1916 K. Points Are Experimentally Measured For Experiment Ni-7. Dashed Line Is Shell-Three Tank Model Output

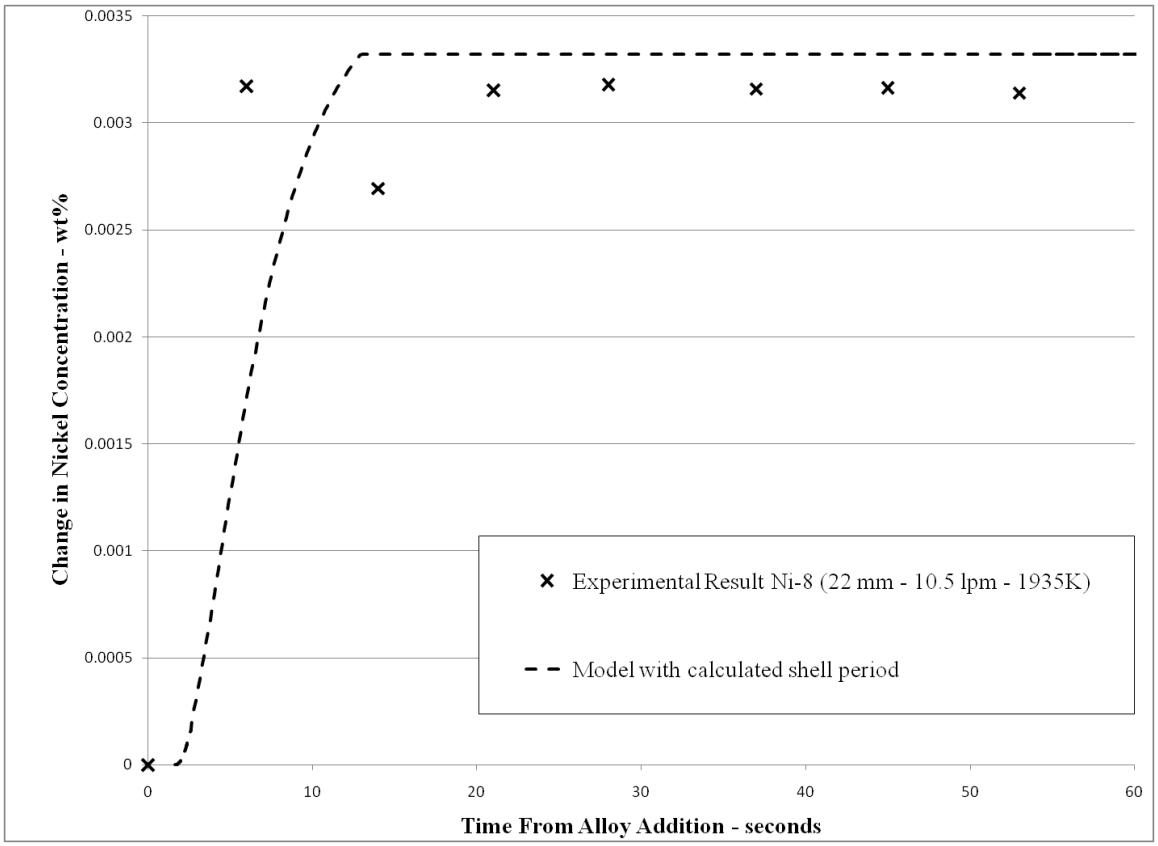

Figure 3.20. Change in Nickel Content in Liquid Steel after Making 0.35% Ni Addition of Nickel Cathode Pieces with Argon Stirring of 10.5 lpm and Initial Ladle Temperature of 1935 K. Points Are Experimentally Measured For Experiment Ni-8. Dashed Line Is Shell-Three Tank Model Output

For ferromanganese (Mn-1 and Mn-2), doubling the argon flow rate cut the computed 95% mixing time in half (34.6 to 15.4 seconds; Table 3.16 and Figure 3.21). This is in spite of the lower flow rate experiment having a higher steel bath temperature. In both cases, the model results underestimate 95% mixing time, but the discrepancy is greater for experiment Mn-1. From the experimental data, the actual 95% mixing time was between 23 and 29 seconds for Mn-1 not the 34.6 seconds calculated.

The model results align with the first experimental data points for the ferromanganese experiments. For Mn-1 (experiment 6) the model splits the difference between sample three and four. Use of a smoothed experimental curve instead of individual data points to represent the experiment would allow the model to better predict the 95% mixing times.

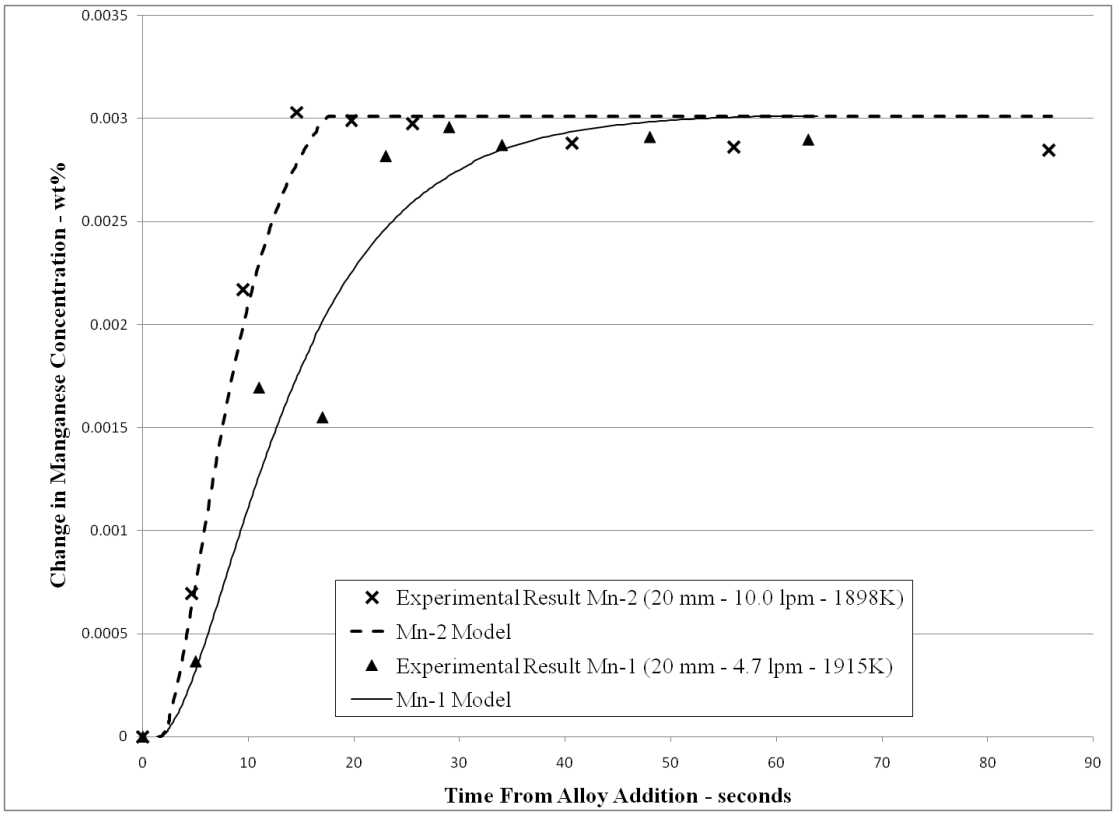

Figure 3.21. Change in Manganese Content in Liquid Steel after Making 0.30% Mn Addition of 20 mm Ferromanganese Lumps with Argon Stirring of 4.7 and 10.0 lpm and Initial Ladle Temperatures of 1898 and 1915 K. Points Are Experimentally Measured For Experiments Mn-1 and Mn-2. Dashed Line Is Shell-Three Tank Model Output For Experiment Mn-2. Solid Line Is Shell-Three Tank Output for Experiment Mn-1

To illustrate the effect of argon flow rate and temperature on nickel dissolution, model results were plotted for pellets (Figure 3.22) and cathodes (Figure 3.23) without the experimental data. The nickel concentration versus time curve for the high argon flow rate and high temperature experiment (Ni-6) is to the left of all other curves. This indicates rapid mixing relative to the other conditions. The high temperature results in early release of the nickel alloy from the steel shell. The low flow rate-high temperature experiment (Ni-5) is released from the steel shell 0.21 seconds earlier than the high flow rate-low temperature experiment (Ni-2). However, the high argon flow rate results in Ni-2 reaching 95% mixed before Ni-5. The low stirring – low temperature experiment (Ni-1) is slowest to reach homogenization.

For nickel cathode, the trends are similar to the nickel pellet, but there is greater separation between the high stirring – low temperature curve (Ni-4) and the low stirring – high temperature curve (Ni-7) (Figure 3.23). In the absence of the shorter shell period afforded by a higher temperature, argon flow rate appears to play a more critical role than temperature in the mixing of nickel and likely all Class I alloys. This supposition was supported using liquid tin and a two tank mixing model.

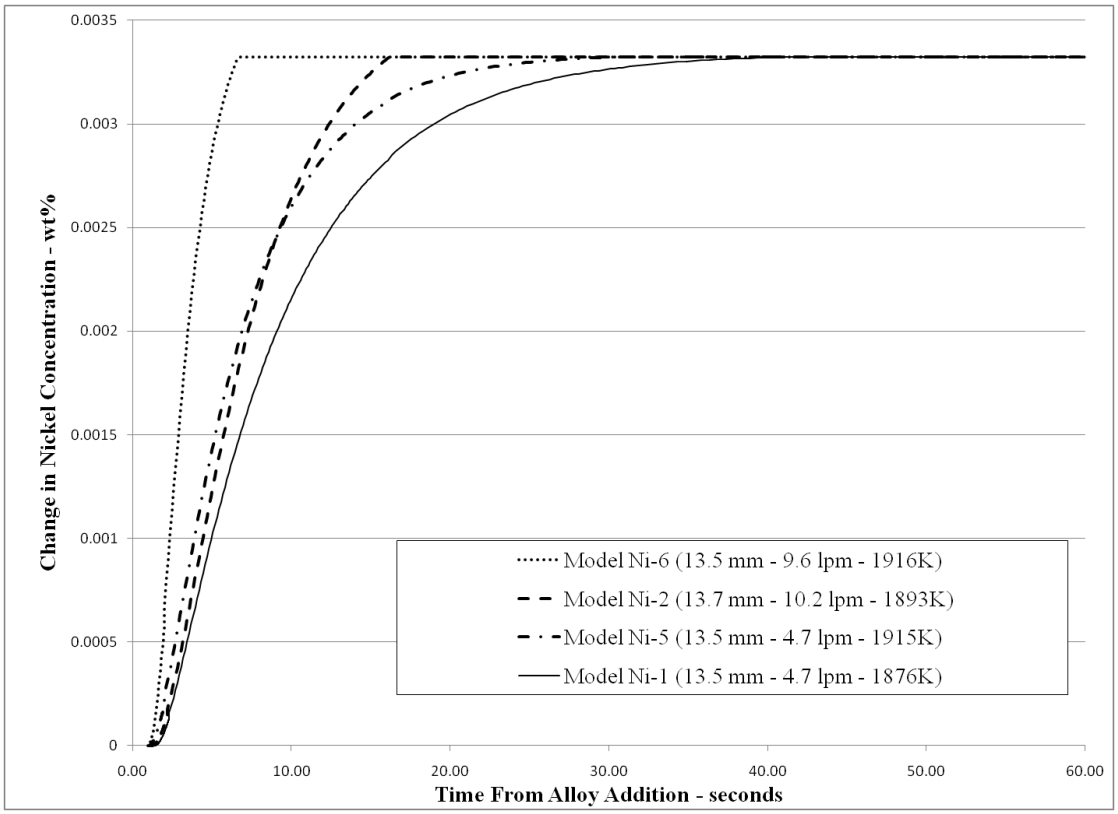

Figure 3.22. Shell-Three Tank Model Output for Nickel Pellet Experiments (Ni-1, Ni-2, Ni- 5, and Ni-6) Showing Change in Nickel Concentration in Liquid Steel after Alloy Addition with Argon Stirring of 4.7 to 10.2 lpm and Ladle Temperatures from 1876 K to 1916 K

In order to test mixing without a shell period, liquid tin (at 315ºC) was poured into the ladle eye. Experimentally, Sn-1 (4.1 lpm) reached 95% mixing time between 15 and 21 seconds with a two-tank model mixing time of 16.2 seconds (Table 3.17 and Figure 3.24). Experiment Sn-2 (4.8 lpm) had a measured 95% mixing time range of 12 to

18 seconds and a model predicted mixing time of 10.8 seconds. Sn-1 had a stirring power of 290 W/T while Sn-2 was 339 W/T. Under the influence of natural convection (Sn-3), an alloy rich region was found to circulate but the natural circulation was insufficient to homogenize the alloy within two minutes. All three experiments were conducted at similar temperatures and without a steel shell period. Results indicate that a small increase in argon flow rate (0.7 lpm) can significantly reduce mixing times (33% reduction based on two tank model or 17% using mean of experimental value range).

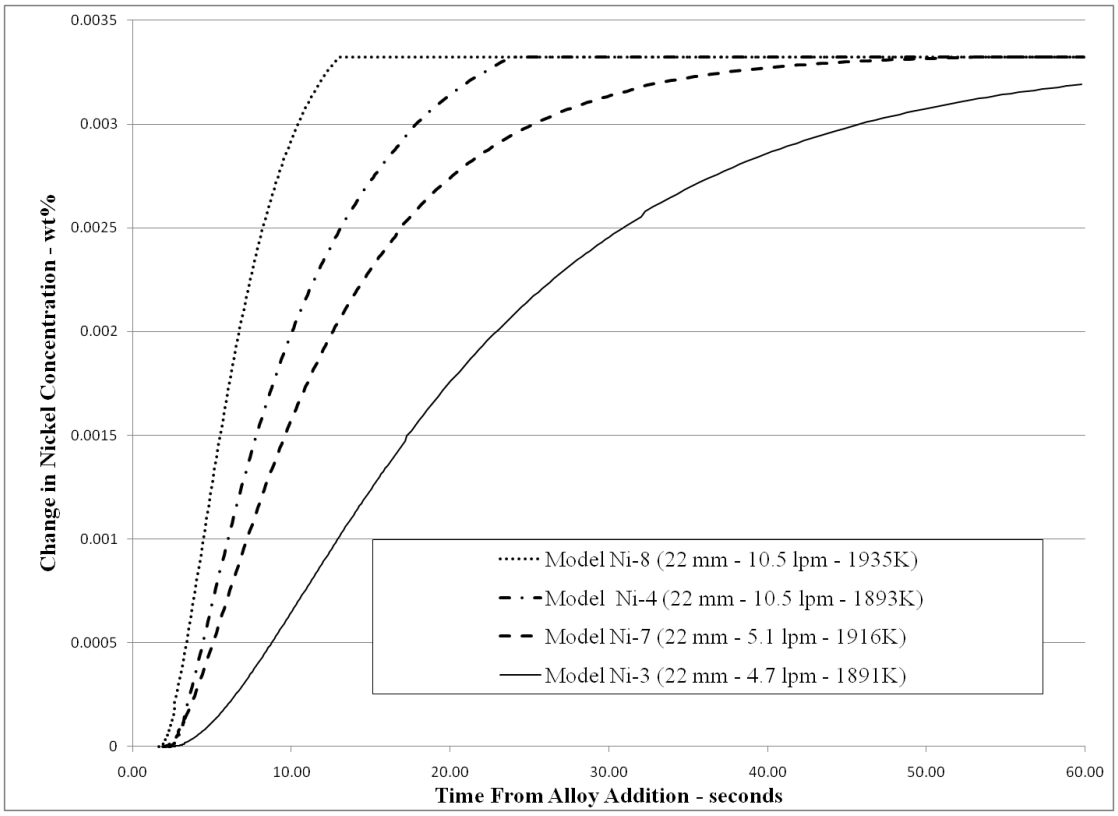

Figure 3.23. Shell-Three Tank Model Output for Nickel Cathode Experiments (Ni-3, Ni-4, Ni-7, and Ni-8) Showing Change in Nickel Concentration in Liquid Steel after Alloy Addition with Argon Stirring of 4.7 to 10.5 lpm and Ladle Temperatures from 1891 K to 1935 K

In order to test mixing without a shell period, liquid tin (at 315ºC) was poured into the ladle eye. Experimentally, Sn-1 (4.1 lpm) reached 95% mixing time between 15 and 21 seconds with a two-tank model mixing time of 16.2 seconds (Table 3.17 and

Figure 3.24). Experiment Sn-2 (4.8 lpm) had a measured 95% mixing time range of 12 to 18 seconds and a model predicted mixing time of 10.8 seconds. Sn-1 had a stirring power of 290 W/T while Sn-2 was 339 W/T. Under the influence of natural convection (Sn-3), an alloy rich region was found to circulate but the natural circulation was insufficient to homogenize the alloy within two minutes. All three experiments were conducted at similar temperatures and without a steel shell period. Results indicate that a small increase in argon flow rate (0.7 lpm) can significantly reduce mixing times (33% reduction based on two tank model or 17% using mean of experimental value range).

Table 3.17. Comparison of Conditions and Mixing Times for Tin

	Argon Flow Rate	Initial Temperature	Model 95% Mixing Time	Sample Time Just Before and After Reaching 95%
Sn-1 Liquid	4.1 lpm	1897 K	16.2	15 to 21
Sn-2 Liquid	4.8 lpm	1896 K	10.8	12 to 18
Sn-3 Liquid	0 lpm	1893 K	-	-

The combined steel shell-three tank model shows that increasing the steel bath temperature results in the alloy being released into the steel sooner. There is some indication that stirring power makes this alloy available sooner, but the effect is not as apparent as temperature. As was seen in the experimental results (Section 3.13), increasing stirring power decreased mixing time. Unlike the experimental conclusions, there was less difference in the modeled 95% mixing time between ferromanganese and nickel. This could be due to having only two ferromanganese experiments rather than eight evaluated in the experimental section (only two experiments met all of the experimental procedure requirements for inclusion in the modeling section). One of the two experiments showed a concentration dip on the third experimental chemical sample which shifted the model to a longer mixing time.

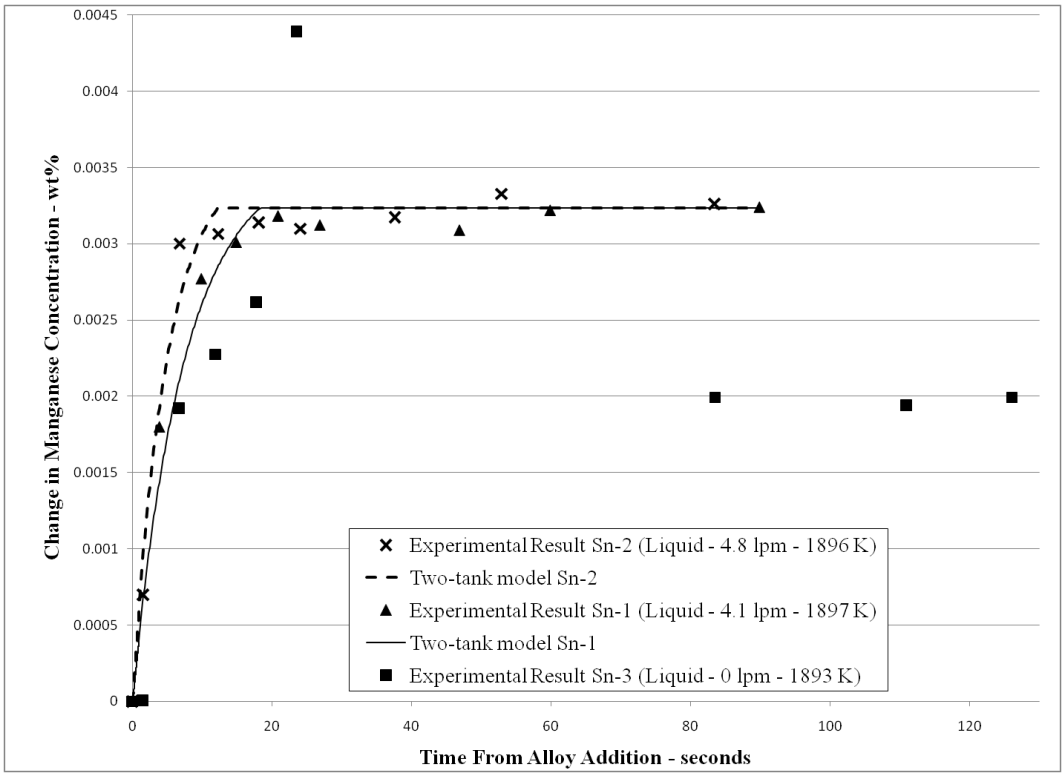

Figure 3.24. Change in Tin Content in Liquid Steel after Making 0.35% Sn Addition of Liquid Tin with Argon Stirring of 0, 4.1, and 4.8 lpm and Initial Ladle Temperatures of 1893, 1896, and 1897 K. Points Are Experimentally Measured for Experiments Sn-1, Sn-2, and Sn-3. Dashed Line Is Shell-Two Tank Model Output for Experiment Sn-2. Solid Line Is Shell-Two Tank Output for Experiment Sn-1

3.3.4. Class II Alloy Dissolution Model Results. After the steel shell melts, Class II alloy's dissolution is limited by diffusion across a boundary layer. The dissolution model initially requires that several values be input, including alloy size, ladle temperature, and argon flow rate. Unlike the three-tank model with zone fractions and exchange rates, the dissolution model only has one variable parameter. This parameter is an effective initial slip velocity.

The effective slip velocity was found using the spreadsheet solver function. This was done very much like the three-tank model, except the dissolution model only has one adjustable parameter rather than two. A table within the spreadsheet would calculate the difference between the dissolution model and the corresponding experimental value.

These differences were summed. The solver then adjusted the effective slip velocity to give the sum a value of zero.

None of the spheroidal ferroniobium additions approached the 95% mixing level within the experimental period. The steel in the ladle would be frozen long before reaching 95% mixed. A new mixing criterion of 33% was chosen to evaluate the dissolution model against the experimental results.

After modeling the experimental result, the effective slip velocity was used to predict a 95% mixing time using the argon flow rate and initial ladle temperature with no heat loss. The no heat loss condition was required to prevent the model temperatures from dropping below the steel liquidus temperature.

Ferroniobium lump experiments did not show the circulating alloy rich region exhibited by Class I alloys. Thus there is better agreement between the computed 33% mixing time and experimental 33% mixing time range with the dissolution model compared to the three tank model 95% mixing times. The alloy rich region is not likely to form as mixing in the ladle is rapid compared to the dissolution of alloy across the boundary layer.

Model results for 33% mixing times at high stirring rates showed little dependence on alloy size. Model mixing times ranged from 34 seconds for 10 and 15 mm lumps to 41 seconds for 20 mm lumps (Table 3.18). The lack of size dependence is similar to the surface area specific alloy transfers rates in Section 3.1.3.1. Unfortunately, the argon flow rate varied from 9.9 to 10.4 lpm for the high stirring rate. This may mask subtle results based on size. At low stirring rates, 33% mixing times increased with size. For 10, 15 and 20 mm ferroniobium spheroids, the model mixing times were 79, 106 and 147 seconds, respectively. Again the argon flow rate varied causing the stirring power to increase in each of the low stirring rate experiments. This would indicate that dissolution time is probably proportional to alloy size.

The model's predicted 95% mixing times (Table 3.18) were excessively long at low stirring rates. 20 mm additions would require more than 10 minutes to reach 95% mixed. Even at high flow rates 10 mm lumps are projected to require 153 seconds to reach 95% mixed. Gourtsoyannis, Guthrie, and Ratz predicted that a 50.8 mm diameter sphere would only require 384 seconds to dissolve, while Argyropoulos and Guthrie

indicated dissolution times of 32 seconds for a 20 mm sphere at 0.9 m/s slip velocity and 120 seconds at 0.3 m/s.[203, 204]

Table 3.18. Computed and Measured 33% Mixing Time and Project 95% Mixing Time for Class II Alloy – Ferroniobium

Experiment	Alloy Diameter – mm	Argon flow Rate – liters per minute	Initial Ladle Temperature – K	Stirring Power – W/T	Computed 33% Mixing time – seconds	Sample Time Just Before and After Reaching 33%	Projected 95% mixing time – seconds
Nb-1	10	4.4	1905	313	79	53 to 83	271
Nb-2	10	9.9	1903	703	34	28 to 42	153
Nb-3	15	4.5	1898	319	106	>89	446
Nb-4	15	10.0	1905	710	34	26 to 44	146
Nb-5	20	5.1	1901	362	147	>85	628
Nb-6	20	10.4	1904	738	41	28 to 43	188

Effective slip velocity for the dissolution model was much lower than the slip velocities used by Argyropoulos and Guthrie. The model slip velocities ranged from 0.0014 m/s to 0.045 m/s. The slip velocities are shown in Table 3.19. At low stirring power (313 to 362 W/T) the slip velocity increased with stirring power from 0.0014 through 0.0027 to 0.0037 m/s. The high stirring rate experiments showed dramatic increases in effective slip velocity. At 703, 710, and 738 W/T, the effective slip velocities were 0.0079, 0.027, and 0.045 m/s, respectively.

There is a transition in effective slip velocity between 5 and 10 lpm argon flow rate. This higher flow rate may prevent or break-up alloy agglomeration and/or change where the alloy particles are dissolving in the ladle.

Granular ferroniobium may be a better choice than lump additions in time critical applications. Granular ferroniobium homogenized much faster than the lump additions, reaching 95% by 60 seconds at 4.3 lpm and 40 seconds at 10.1 lpm. Unfortunately, the granular niobium tended to float on the surface and stick to the side of the vessel at the steel surface, thus the granular niobium should be introduced subsurface to prevent loss to the slag layer.

Table 3.19. Effective Slip Velocities Used to Model Ferroniobium Experiments

Experiment	Effective Slip Velocity – m/s	Stirring Power – W/T	Average Heat Transfer Coefficient – $W/m^2 \cdot K$	Average Mass Transfer Coefficient – m/s
Nb-1	0.0014	313	2388	$1.07x10^{-5}$
Nb-2	0.0079	703	5628	$2.51x10^{-5}$
Nb-3	0.0027	319	2619	$1.17x10^{-5}$
Nb-4	0.027	710	8376	$3.73x10^{-5}$
Nb-5	0.0037	362	2617	$1.17x10^{-5}$
Nb-6	0.045	738	9347	$4.16x10^{-5}$

Another option to speed dissolution would be to use a nonstandard ferroniobium. Gourtsoyannis et al. determined that standard 66% ferroniobium would contain two high melting point intermediate phases ε (melting range 1655 to 1928°C) and ζ (melting point 2073°C).[205] They prepared a 50% niobium ferroalloy which appeared to dissolve three times faster than standard ferroniobium.

For 10-mm ferroniobium lumps, the 4.4 lpm experiment, Nb-1follows the model line to the end of the experiment (Figure 3.25). In contrast, experimental measurements for Nb-2 show a steep initial rise in alloy concentration which slows between 20 and 30 seconds. The model for Nb-2 strikes a balance between the two slopes shown in the experiment. This results in the model initially underestimating dissolution but ultimately the model shows greater dissolution than the experimental results.

Experiment Nb-3 and the dissolution model show good agreement through 60 seconds, but the 90 second sample falls below the model (Figure 3.26). The model for Nb-4 is a reasonable approximation of the experimental results for the first 60 seconds. The final measured value at 90 seconds is well below the model. This drop in dissolution may be related to the low ladle temperature near the end of the experiment.

The model for Nb-6, Figure 3.27, initially overestimates alloy dissolution, but the experimental measurements shows a jump in niobium concentration around 20 seconds. This causes the model to ultimately underestimate dissolution rate at the end of the experiment. Experiment Nb-5 shows similar behavior, where early in the experiment the dissolution rate is low and then a change occurs between 25 and 30 seconds where the

dissolution rate increases. This change could be the result of agglomerated particles breaking-up.

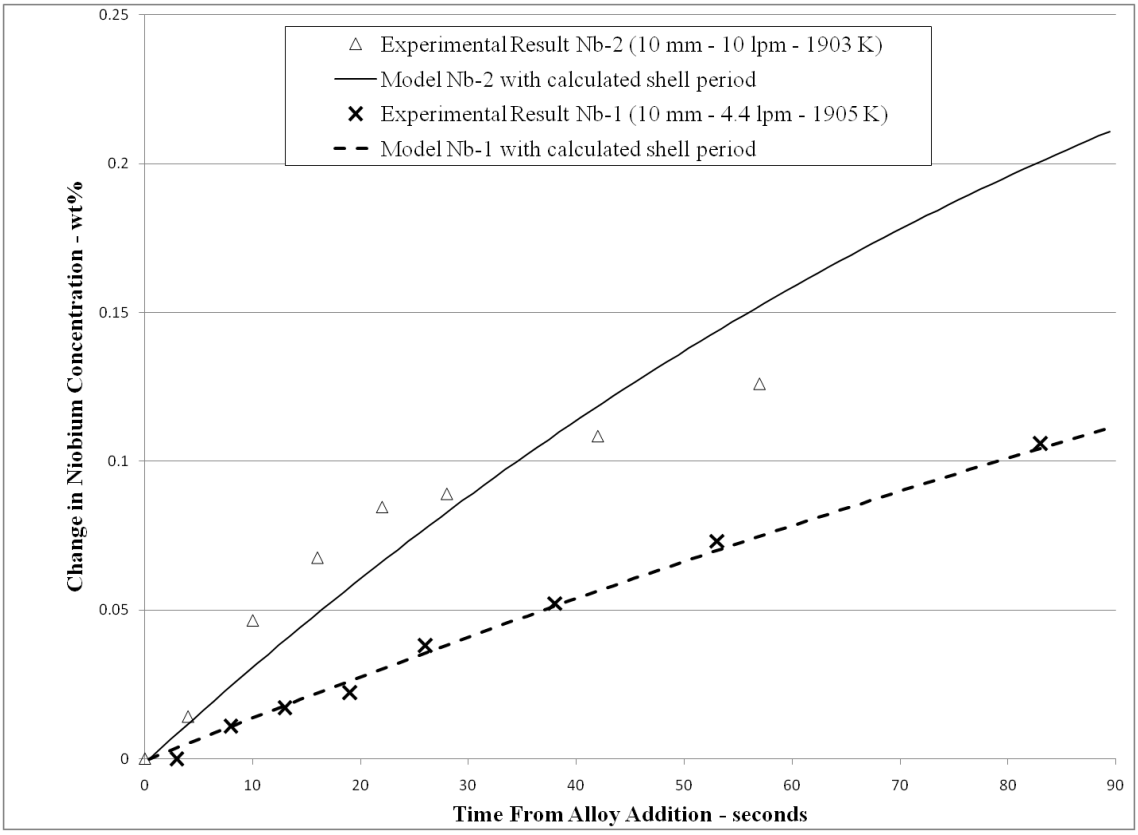

Figure 3.25. Change in Niobium Content in Liquid Steel after Making 0.30% Nb Addition of 10 mm Ferroniobium Lumps with Argon Stirring of 4.4 and 10 lpm and Initial Ladle Temperature of 1903 K and 1905 K. Points Are Experimentally Measured For Experiments Nb-1 and Nb-2. Dashed Line Is Dissolution Model Output For Experiment Nb-1. Solid Line Is Dissolution Model Output for Experiment Nb-2

Overall, the dissolution models show good agreement with the experimental data. Effective slip velocities were lower than expected. Ferroniobium may be dissolving in an area of the ladle with low steel velocity, or the calculated heat/mass transfer coefficient may not reflect actual conditions. As was seen in the experimental results (Section 3.1.2) ferroniobium lumps mix at least an order of magnitude slower than similarly sized Class I alloys and granular ferroniobium.

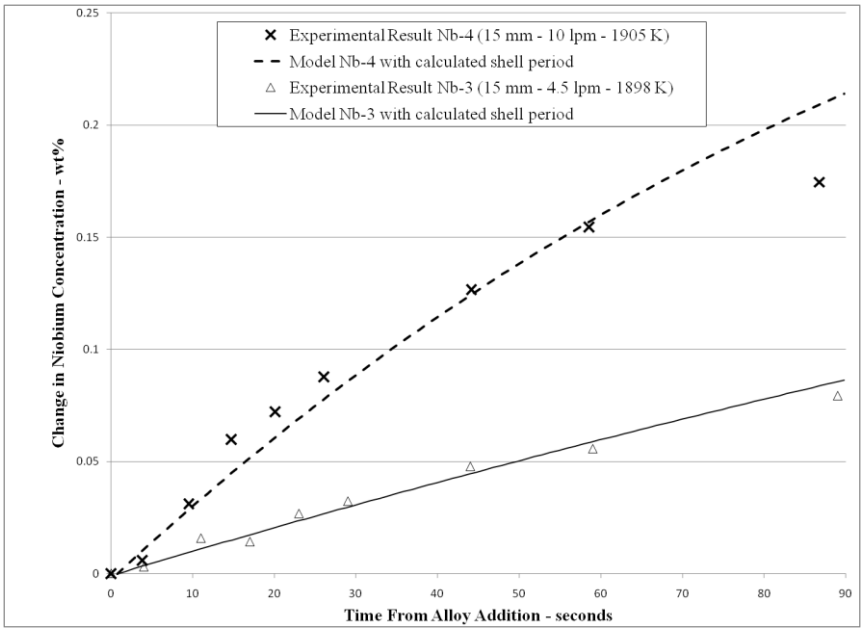

Figure 3.26. Change in Niobium Content in Liquid Steel after Making 0.30% Nb Addition of 15 mm Ferroniobium Lumps with Argon Stirring of 4.5 and 10 lpm and Initial Ladle Temperatures of 1898 K and 1905 K. Points Are Experimentally Measured For Experiments Nb-3 and Nb-4. Dashed Line Is Dissolution Model Output For Experiment Nb-4. Solid Line Is Dissolution Model Output for Experiment Nb-3

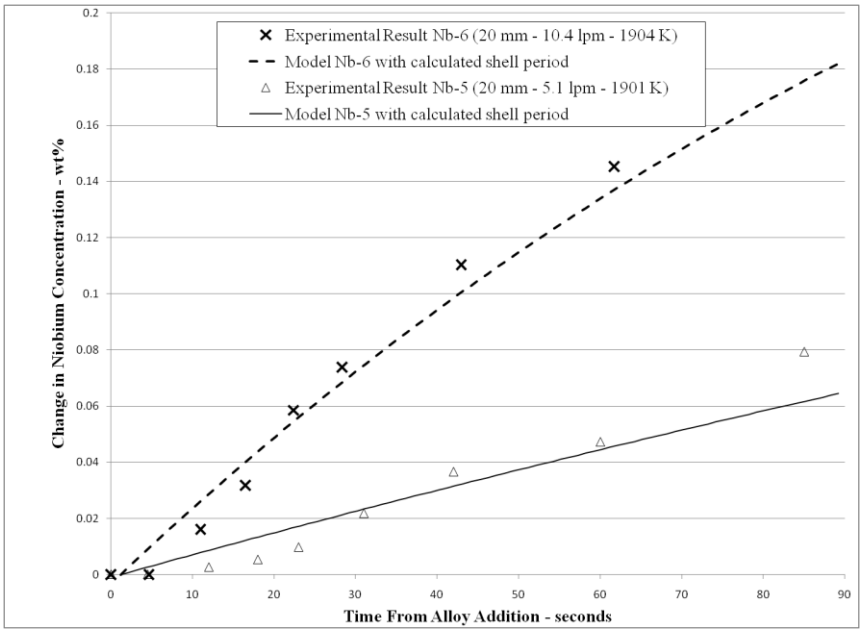

Figure 3.27. Change in Niobium Content in Liquid Steel after Making 0.30% Nb Addition of 20 mm Ferroniobium Lumps with Argon Stirring of 5.1 and 10.4 lpm and Initial Ladle Temperature of 1901 K and 1904 K. Points Are Experimentally Measured For Experiments Nb-5 and Nb-6. Dashed Line Is Dissolution Model Output For Experiment Nb-6. Solid Line Is Dissolution Model Output for Experiment Nb-5

3.3.5. Spreadsheet Model at Industrial Scales. The steel shell and dissolution model were evaluated for additional alloys and conditions that better reflect continuous steelmaking and/or industrial scale operations. Alloy properties were more thoroughly evaluated to determine which thermo-physical properties are most critical in shell formation. In addition, the three-tank model was applied to the manganese dissolution data from Peter et al.s' study of silicomanganese in a 120 ton ladle.

3.3.5.1 Steel shell model – additional alloys. To better understand the influence of alloy properties, nine alloys were evaluated with sizes between 10 and 80 mm diameter. These spherical alloys, with an initially temperature of 300 K, were then added to a steel bath at 1585°C with a constant slip velocity of 0.40 m/s (Table 3.20 and Figure 3.28). This temperature was chosen to match the finishing vessel in Missouri S&T continuous steel making process.[206] The slip velocity was selected from Peter et al.s' Ladle dissolution model.[207]

For a given alloy, increasing the size eight fold resulted in a 26 to 28 times increase in the steel shell period, while the maximum variation in steel shell period between species was 3.5 times (50% ferrosilicon to electrolytic chromium). Electrolytic chromium showed the widest range in steel shell period, ranging from 1.17 seconds at 10 mm to 31.17 seconds at 80 mm. 50% ferrosilicon showed the least range (0.33 to 9.32 seconds). Predicted times for 75% ferrosilicon do not include the exothermic reaction between silicon and iron. This reaction would shorten the actual steel shell period.

Steel shell formation depends on the alloy's ability to act as a heat sink. Steel shell period is proportional to the product of density, heat capacity, and melting point, for alloys of similar thermal conductivity (this product is listed for nine alloys in Table 3.20). Data points for steel shell period plotted against the product of density, heat capacity and melting point fall along nearly linear lines for a given alloy size, as shown in Figure 3.29. Linear trend lines fit through the data with R^2 values of 0.994, 0.9948, and 0.9961 for 40, 80 and 20 mm diameter particles (six alloys: 50% ferrosilicon, 75% ferrosilicon, silicomanganese, low carbon ferromanganese, low carbon ferrochrome, and high carbon ferrochrome). Manganese, nickel, and electrolytic chromium are not plotted in Figure 3.28 because they have thermal conductivities more than four times higher than the other alloys.

Table 3.20. Predicted Steel Shell Period and Alloy Center Temperature (ladle with constant slip velocity of 0.40 m/s and temperature of 1858 K)

Alloy	Diameter	Length of Steel Shell Period - s	Product of $\rho \cdot C_p$ and melting point – GJ/kg	Alloy Center Temperature – Percent of Melting Temperature	Alloy Center Temperature – K	Thermal Conductivity – W/m·K
50% Ferrosilicon (T_{melt}=1500 K)	10	0.33	3.92	22.9%	344	9.62
	20	1.05		21.0%	315	
	40	3.19		20.1%	302	
	80	9.32		20.0%	300	
75% Ferrosilicon (T_{melt}= 1605 K)	10	0.39	4.22	18.7%	300	2.93
	20	1.10		18.7%	300	
	40	3.44		18.7%	300	
	80	10.08		18.7%	300	
Silicomanganese (T_{melt}= 1566 K)	10	0.44	5.50	19.3%	302	6.28
	20	1.38		19.2%	300	
	40	4.10		19.2%	300	
	80	12.22		19.2%	300	
Low Carbon Ferromanganese (T_{melt}= 1478 K)	10	0.57	7.69	20.5%	304	7.53
	20	1.69		20.3%	300	
	40	5.21		20.3%	300	
	80	15.33		20.3%	300	
Low Carbon Ferrochrome (T_{melt}= 1943 K)	10	0.59	8.93	15.7%	305	6.5
	20	1.94		15.5%	301	
	40	6.01		15.4%	300	
	80	17.66		15.4%	300	
High Carbon Ferrochrome (T_{melt}= 1773 K)	10	0.67	10.9	19.5%	346	12.55
	20	2.22		18.1%	322	
	40	6.69		17.2%	305	
	80	19.83		16.9%	300	
Manganese (T_{melt}= 1523 K)	10	0.83	9.07	102.8%	1565	50
	20	2.49		86.9%	1324	
	40	7.04		67.6%	1029	
	80	18.75		44.0%	671	
Nickel (T_{melt}= 1728 K)	10	0.88	8.77	103.9%	1795	85.5
	20	2.62		101.2%	1749	
	40	8.00		94.9%	1640	
	80	22.39		83.2%	1439	
Electrolytic Chromium (T_{melt}= 2173 K)	10	1.17	14.6	80.7%	1753	60
	20	3.76		76.9%	1670	
	40	11.15		68.4%	1486	
	80	31.17		55.2%	1200	

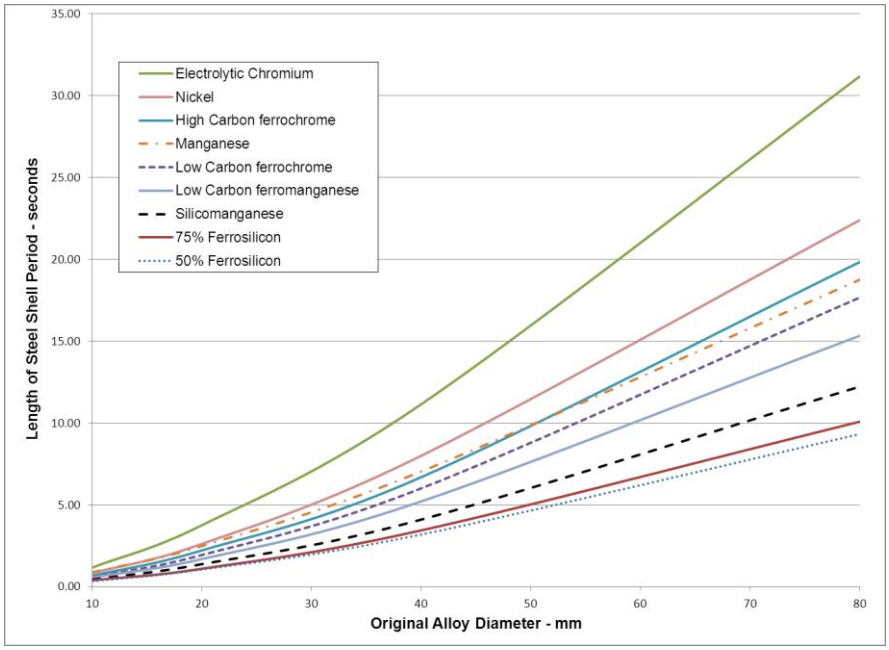

Figure 3.28. Predicted Length of Steel Shell Period for Spherical Alloys Initially at 300 K Added to a Ladle with Constant Slip Velocity of 0.40 m/s and Temperature of 1858 K (1585°C) Versus Original Alloy Diameter

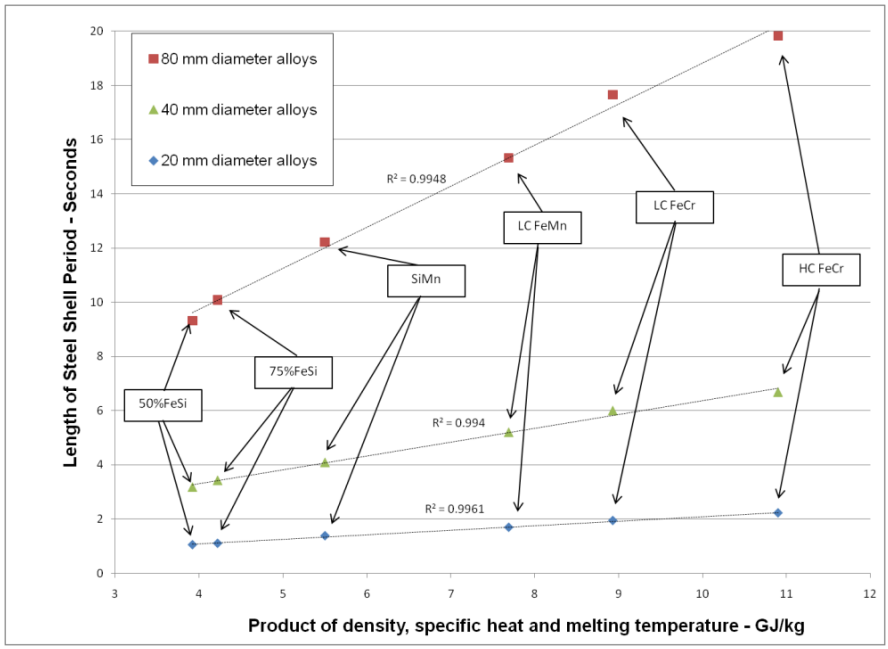

Figure 3.29. Steel Shell Period for Six Alloys (50% ferrosilicon, 75% ferrosilicon, silicomanganese, low carbon ferromanganese, low carbon ferrochrome, and high carbon ferrochrome) and Three Alloy Sizes (20, 40, and 80 mm) Plotted Against the Product of the Alloys Density, Specific Heat, and Melting Point to Show Relationship between Alloy Properties and Length of Steel Shell Period. (Linear trend lines were fit through the data points; R^2 ranges from 0.994 to 0.9961)

Alloy thermal conductivity also plays a significant role in the steel shell period. Low thermal conductivity results in a large thermal gradient within the alloy particle. This reduces the temperature difference between the frozen shell and alloy surface. A smaller temperature difference results in less heat transfer, a smaller shell and a shorter shell period. Manganese and nickel have relatively high thermal conductivities. As a result, they have longer steel shell periods than would be predicted based on their density, heat capacity, and melting temperature alone.

For mixing and dissolution modeling, Class I alloys were assumed to be fully melted and Class II alloys uniformly heated to the steel melt temperature at the end of the shell period. These assumptions were not supported by the steel shell model, even at the reduced temperature of 1585°C. In spite of transferring at least 98.7% of the energy required to melt the alloy particles (for all nine alloys evaluated with a constant slip velocity of 0.40 m/s in steel at 1585°C).

The temperature at the center of the alloy sphere for 75% ferrosilicon, silicomanganese, and low carbon ferrochromium would be within five degrees of their starting temperature, just as the steel shell melts (shown graphically in Figure 3.30 with data in Table 3.20). In contrast, the three elemental metals (chromium, nickel and manganese) show temperature increases from 371 to 1495 K. While, 20 mm nickel and 10 mm manganese spheres would reach their melting temperature and experience a thermal arrest, prior to the steel shell melting. In the absence of exothermic mixing all other alloys would have a solid core at the end of the steel shell period.

Modeling with additional alloys confirmed the results seen when evaluating the steel shell model in Section 3.3.1. First, thermal gradients are likely to exist in all but the most conductive alloys when the steel shell melts. Second, for a given ladle temperature, alloy size plays the most significant role in steel shell period length. Third, alloy specie plays an important role in steel shell formation.

For a given alloying element, reducing the melting temperature or density would shorten the steel shell period, making alloy available sooner. This could be accomplished for a few alloying elements by switching to a ferroalloy from an elemental addition. In most cases this would also reduce the thermal conductivity as well, which would shorten the steel shell period.

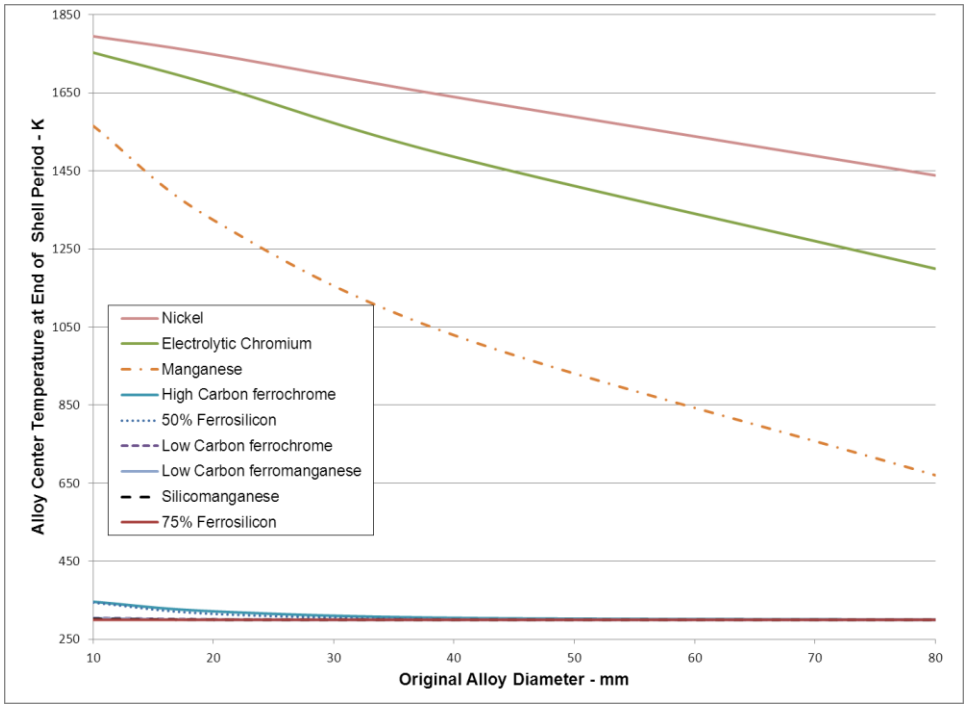

Figure 3.30. Predicted Temperature at the Center of Alloy Spheres Just as the Steel Shell is Completely Melted for a Constant Slip Velocity of 0.40 m/s in a Ladle at 1858 K (1585°C) versus Original Alloy Diameter. (Alloy sphere was initially at a uniform temperature of 300 K).

3.3.5.2 Using the steel shell model for selecting Class I alloy size. Lee suggested that for good alloying practice, low and high density additions should be free of the steel shell prior to either resurfacing in the ladle or reaching the ladle bottom.[208] The steel shell model was configured to track alloy depth relative to the melt surface, for the purpose of sizing alloy additions for the Missouri S&T continuous steelmaking operation.

In the Missouri S&T continuous steelmaking operation, alloying will primarily occur in the reducer vessel with final chemistry adjustment in the finishing vessel. Residence time in each vessel is expected to be 15 minutes. Steel enters the reducer at 1585°C and exits at 1554°C.[209] Alloy spheres were assumed to fall 1.5 meters into stagnant steel at 1585°C, with a reducer vessel depth of two meters.

Under these conditions, neutral density alloys like ferromanganese would completely melt (alloy and shell) before reaching the ladle surface or bottom with two restrictions. First, the alloy had to be 40 mm diameter or smaller and second, the alloy

density had to be within 20% of the steel bath density. With neutral density alloys evaluated, 50% ferrosilicon and nickel were chosen to represent low and high density additions.

The low density addition, 50% ferrosilicon was selected based on density, a nearly neutral heat of mixing, and because it had the shortest steel shell period of the nine alloys evaluated in Section 3.3.5.1. The shell model does not account for an exothermic reaction between the liquid alloy and steel shell. Aluminum, silicon, and 75% ferrosilicon are all less dense than 50% ferrosilicon but they would all be expected to react with the steel shell (likely follow dissolution route 4).

The model predicted that Spherical 50% ferrosilicon additions of 10, 20, and 40 mm would resurface in 0.17, 0.24, and 0.34 seconds. Unfortunately, none of these particles would be free of the steel shell in this time. The 50% ferrosilicon would need to be introduced subsurface rather than gravimetrically to prevent resurfacing. In general, the model predicted that alloys with densities less than 40% of the density of liquid steel would tend to reach the slag layer prior to melting.

Nickel had the highest density of all Class I alloys, as well as having a relatively high melting point and thermal conductivity. Thus nickel should represent the limiting case (longest shell period) for Class I alloys that sink.

Nickel spheres of 10, 20 and 40 mm diameter would reach a depth of two meters in 7, 4.8, and 3.2 seconds. These particles had predicted steel shell periods of 0.61, 1.82, and 5.55 seconds, so the 40 mm nickel would reach the ladle bottom still encased in the steel shell. The model also indicates that the 20 mm and smaller particles would follow route 1 and be fully melted when the steel shell disappears. Based on this result, Class I alloys with densities greater than the liquid steel should be 20 mm or smaller, where possible (the alloy must still penetrate the slag layer).

3.3.5.3 Class II alloys for continuous steelmaking. Based on experimental results, Class II alloys take much longer to dissolve than Class I alloys. This could result in unhomogenized alloys at the caster if the alloy particles were too large. To investigate size requirements, the dissolution model was configured with an initial temperature of 1585°C and a temperature loss rate to reach 1554°C in 15 minutes to match the reducer vessel. The stirring power (738 W/T), alloy size (20 mm) and initial slip velocity (0.045

m/s) from experiment 30 were used to evaluate dissolution of six Class II alloys. The models were then rerun with a slip velocity of 0.40 m/s.

Using these conditions, Class II alloys with exothermic heats of dissolution mixed more rapidly than endothermic chromium and molybdenum, (Figure 3.31-0.045 m/s and Figure 3.32-0.40 m/s). Spherical 20-mm diameter titanium (-996.9 kJ/kg heat of dissolution) mixed in 55 seconds and 20 seconds at 0.045 and 0.40 m/s slip velocity, while vanadium required twice as long as titanium to reach 95% mixed (Table 3.21).

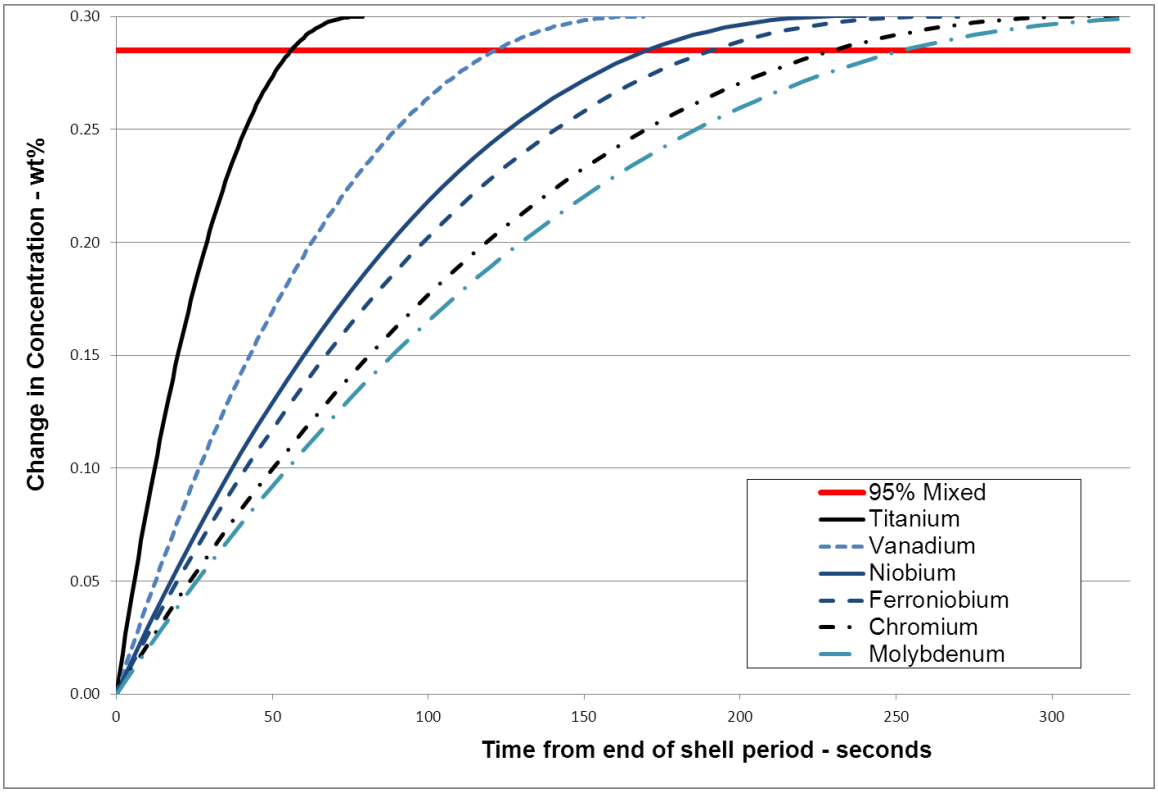

Figure 3.31. Predicted Change in Class II Alloy Concentration in Liquid Steel after Making a 20-mm Diameter Alloy Addition of 0.30% with Stirring Power of 738 W/T and Initial Ladle Temperature of 1585°C (after steel shell melts, initial slip velocity 0.045 m/s, temperature loss rate 0.034°C/s)

Niobium and ferroniobium required more than three times longer than titanium. Niobium has a more exothermic heat of mixing than ferroniobium. As a result, niobium dissolves slightly faster than ferroniobium.

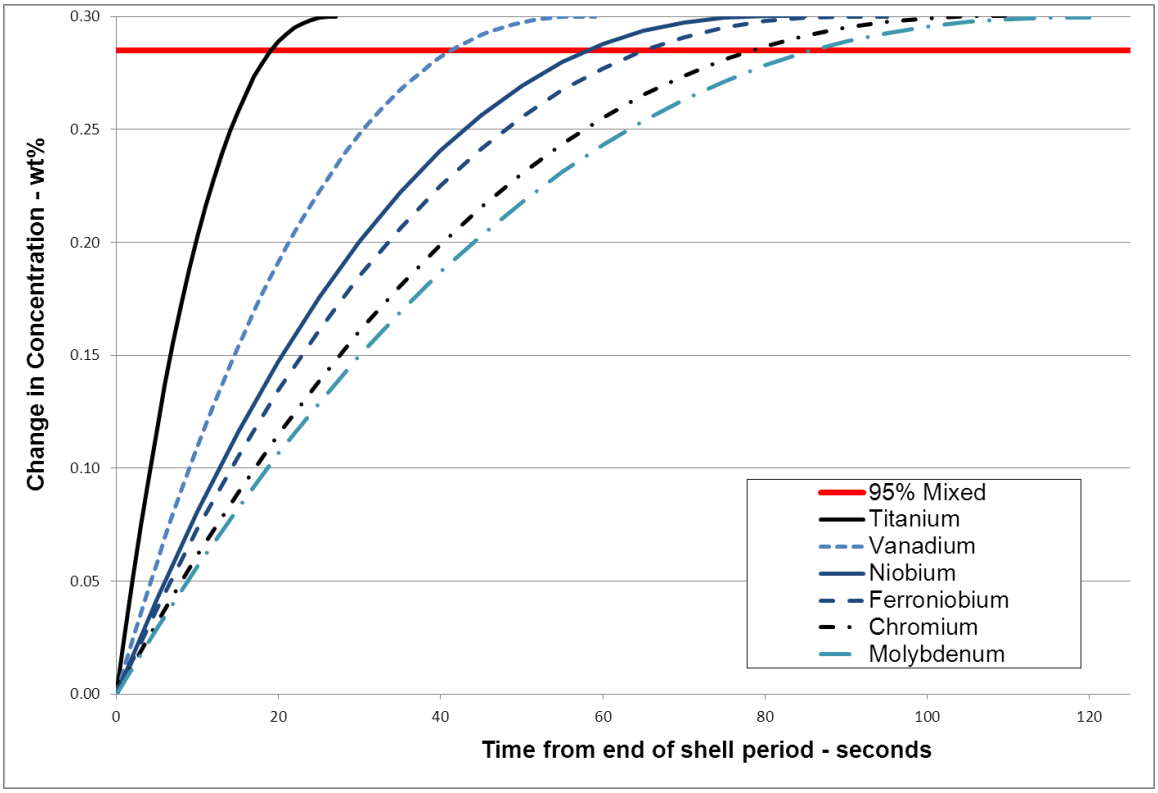

Figure 3.32. Predicted Change in Class II Alloy Concentration in Liquid Steel after Making a 20-mm Diameter Alloy Addition of 0.30% with Initial Slip Velocity of 0.4 m/s and Reducer Vessel Temperature of 1585°C (after steel shell melts, temperature loss rate 0.034°C/s).

Table 3.21. Predicted 95% Mixing Times for Class II Alloys (without steel shell period) in Steel at 1858 K (1585°C) with initial slip Velocities of 0.045 and 0.40 m/s

Alloy	95% mixing time with initial slip velocity of 0.045 m/s - seconds	95% mixing time with initial slip velocity of 0.40 m/s - seconds
Titanium	55	20
Vanadium	120	40
Niobium	170	60
Ferroniobium	190	65
Chromium	230	80
Molybdenum	255	85

Chromium required 230 and 80 seconds (84 seconds including the steel shell period) to reach 95% mixed. 20 and 40 mm molybdenum would dissolve in 4.5 and 12

minutes at 0.045 m/s slip velocity. This is less than the 15 minute residence time of the reducer vessel but molybdenum (density of 10,280 kg/m^3) additions would likely sink to the bottom of the reducer vessel where steel velocities tend to be low.

Based on these results and the granular ferroniobium experiments, the smallest available Class II alloys should be employed. To avoid reactions with slag, granular type alloys should be introduced below the slag.

3.3.5.4 Three tank models applied to 120-ton ladle. Dissolution data from Peter et al.s' study of silicomanganese was used with the three tank model (results in Figure 3.33).[210] The model does not predict the alloy rich recirculation seen in the data between 50 and 150 seconds, but does provide good agreement for data after 150 seconds.

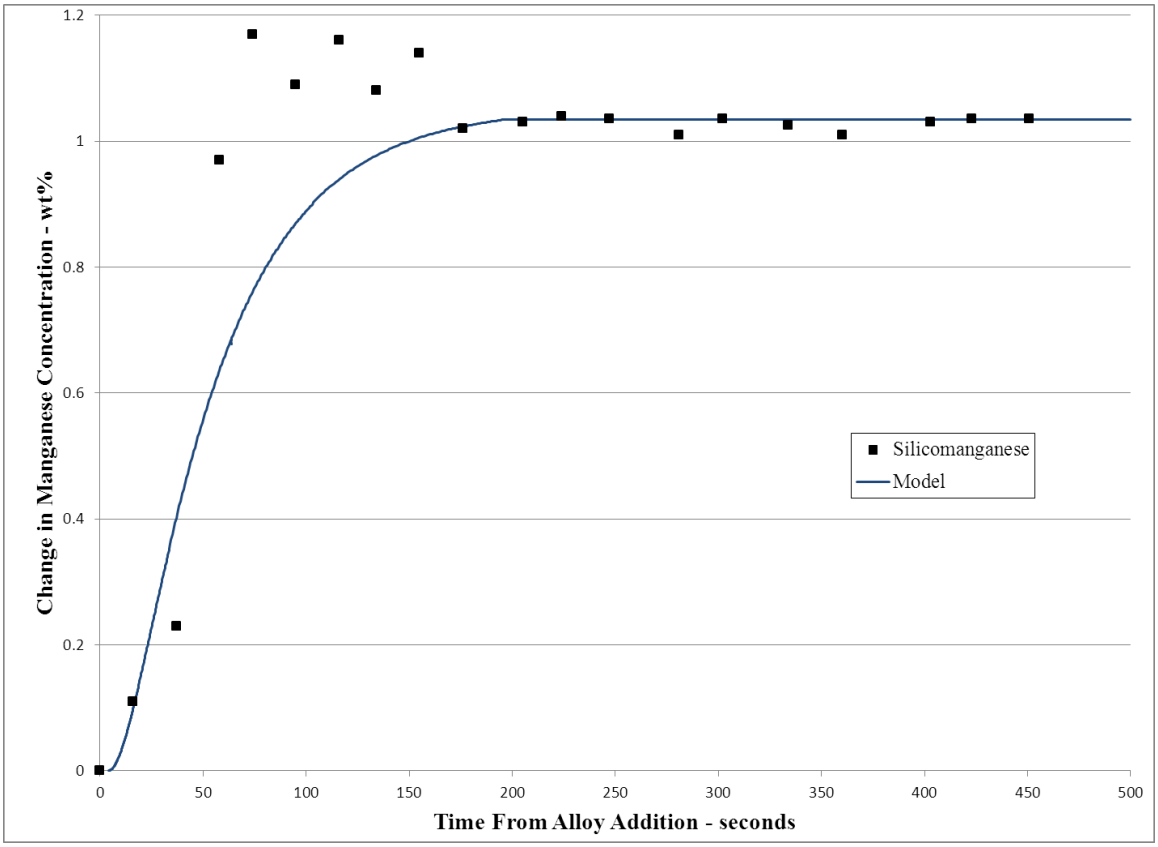

Figure 3.33. Change in the Manganese Content in Liquid Steel after a Silicomanganese Addition of 13 to 64 mm Spheroids to a 120-ton Ladle with Argon Stirring of 113 lpm, Shown with Three Tank Model Output (solid line)[211]

The model used the same dead zone volume fraction (0.089) and alloy zone fraction as the low argon flow rate experiments and the model was adjusted in the same manner as described in Section 3.2.3. Dead zone to mixing zone volume exchange rate was similar to experiment Mn-1 but the alloy zone to dead zone exchange rate was an order of magnitude slower (values in Table 3.22).

Table 3.22. Computed and Measured 95% Mixing Time and Model Parameters for 120-ton Ladle and Experiment Mn-1

Experiment	Alloy	Argon flow Rate – lpm	Computed 95% Mixing time – seconds*	Experimental Mixing Time	Alloy Volume Exchange Rate Fraction	Volume Exchange Rate Fraction
120-ton Ladle	Silicomanganese	113	133.5	135	0.0018	0.008
Mn-1	Ferromanganese	4.7	34.6	23 to 29	0.0205	0.0084

*Time for alloy to stay within +/- 5% of alloy aim

The experimental data suggests that the manganese concentration fell to within 105% of the alloy aim at 135 seconds and then continued to a homogenized value. The three tank model predicted a 95% mixing time of 133.5 seconds. These values indicate that the three tank model can be applied at larger scales.

4. CONCLUSIONS AND RECOMMENDATIONS

4.1. CONCLUSIONS

This research has led to the following conclusions:

1. Based on the experimental results, smaller diameter Class I (low melting point) as well as Class II (high melting point) alloys homogenize faster and have a shorter steel shell period. The Steel Shell Model confirms that the steel shell period is shorter for smaller size alloys of both Class I and Class II alloys.
    a. Nickel, 20 mm diameter or less, would be fully melted before reaching the ladle bottom. Nickel represents the limiting case for Class I alloys denser than steel due to a combination of density, thermal conductivity, and melting point.
    b. For Class I alloys with densities within 20% of liquid steel, modeling indicates that alloy particles up to 40 mm would be fully molten. However, Class I alloys less than 40% of the density of liquid steel would tend to float into the slag prior to melting.
2. The experimental results indicate that for alloys of similar size, Class II ferroniobium dissolution is ten times slower than Class I alloys mixing at high stirring power and twenty times slower at low stirring power. The Dissolution Model shows that Class II alloy dissolution rates are limited by diffusion across a boundary layer at the alloy-steel melt interface.
3. Increasing stirring power was experimentally found to decrease homogenization time for both Class I and Class II alloys. Higher stirring power also decreased the time between the alloy addition and the first appearance of alloy in the melt. In addition, increasing the steel bath temperature shortens the delay between the alloy addition and the first appearance of alloy in the melt.

    The Steel Shell Model supports the result that increasing steel bath temperature reduces the steel shell period. According to this model, every 5°C increase in the steel bath temperature results in about a four percent reduction in the length of the steel shell period.

4. The Steel Shell Model shows that for a given thermal conductivity, the steel shell period is proportional to the alloy density, specific heat, and melting temperature. This may support moving from an elemental alloy addition to a ferroalloy in order to reduce the steel shell period.

4.2. RECOMMENDATIONS AND FUTURE WORK

All of the alloys investigated were expected to follow dissolution route 1 or 5 in Figure 1.5, but likely followed routes 1, 3 and 5. In addition, the alloying elements investigated were transferred to the melt without an intermediate reaction. Thus the following recommendations are proposed for future work:

1. Evaluate Class I and II alloys with strongly exothermic behavior. This should result in a dissolution route (route 4) not evaluated in the current research.
2. Evaluate an alloy addition where an intermediate reaction is required to introduce alloy into the steel melt. Examples would include molybdenum oxide for molybdenum and scheelite ($CaWO_4$) for tungsten.

4.3. SUGGESTED CHANGES FOR EXPERIMENTS

The following suggestions are made to improve the experimental process:

1. Prior to evaluating additional alloys, a pressure independent flow meter should be added to the ladle gas system to better regulate argon flow rate. Additionally, a sampling fixture/guide should be added to improve sample location consistency.

2. Continuous chemistry measurement could be investigated to improve experimental resolution and to provide a consistent sample location. This measurement might be obtained by solidifying a layer of steel on a copper or molybdenum wire continuously run across the melt surface. The wire could be sectioned and analyzed with energy dispersive x-ray spectroscopy.

APPENDIX

Shell Model Source Code

The Visual Basic for Access source code called from the Excel steel shell model is shown in Table A.1. This code has several functions. These include the calculation of: Reynolds number, drag force on the alloy sphere, alloy surface area, alloy surface temperature, alloy center temperature, amount of energy transferred, and the transcendental roots required to solve the heat transfer approximation. The steps followed in the steel shell model are shown in Table A.2.

Table A.1. Steel Shell Model VBA Source Code

```
Option Explicit

Function Reynolds (Diameter As Double, Velocity As Double, Density As Double, Viscosity As
Double) As Double
Reynolds = (Density * Velocity * Diameter) / Viscosity
End Function

Function Drag (Density As Double, Velocity As Double, Cd As Double, Radius As Double) As
Double
Drag = 0.5 * Density * Velocity ^ 2 * Cd * (Application.Pi() * Radius ^ 2)
End Function

Function Surface_Area (Radius As Double) As Double
Surface_Area = 4 * Application.Pi() * Radius ^ 2
End Function

Function Theta_surface (Bi As Double, Fo As Double) As Variant
Dim v(), z(), c() As Variant
Dim x, L As Integer Dim count, theta, zeta, Cn, guess, zn, term, term_C, theta_c, Q_ratio, Qterm,
Qsum As Double
ReDim v(0 To 2)
                x = 1 'root counter
                guess = 2.5 'starting point for finding root
                theta = 0 'dimensionless surface temperature
                theta_c = 0 'dimensionless center temperature
                zeta = 0 'transcendental root for dimensionless temperatures and Q/Qo
                Cn = 0 'term used for dimensionless temperatures and Q/Qo
                zn = 0 'variable used when seeking roots
                term = 0 'term inside summation for surface temperature
```

Table A.1. Steel Shell Model VBA Source Code (cont.)

```
term_C = 0 'term inside summation for center temperature
Q_ratio = 0 'Q/Qo
Qterm = 0 'term inside summation
Qsum = 0 'summation of terms


'Determine number of required terms
   L = Int((-2.3 * Log(Fo) + 4) + 0.5) 'log is natural log
ReDim z(1 To L)
ReDim c(1 To L)


'Start finding roots 1 to L
Do Until x = L + 1
   count = 1
   zn = 1 - guess * (1 / Tan(guess))

    Do Until Int(zn * 100) / 100 = Bi Or count > 2500000
      If zn < Bi Then guess = guess + 0.000001
      Else guess = guess -0.000001
       zn = 1 - guess * (1 / Tan(guess))
       count = count + 1
       Loop
    z(x) = guess 'fill root array
    c(x) = 4 * (Sin(z(x)) - z(x) * Cos(z(x))) / (2 * z(x) - Sin(2 * z(x)))
    term = c(x) * Exp(-1 * z(x) ^ 2 * Fo) * ((1 / z(x)) * Sin(z(x)))
    theta = theta + term 'sum term
    term_C = c(x) * Exp(-1 * z(x) ^ 2 * Fo)
    theta_c = theta_c + term_C 'sum series
  x = x + 1 'increment counter
  guess = guess + 3
Loop


'get Q/Qo using final center temperature
x = 1
For x = 1 To L
Qterm = ((3 * theta_c) / (z(x) ^ 3)) * (Sin(z(x)) - z(x) * Cos(z(x)))
Qsum = Qsum + Qterm
Next x
Q_ratio = 1 – Qsum
v(0) = theta; v(1) = theta_c; v(2) = Q_ratio
Theta_surface = v
End Function
```

Table A.2. Steps in Steel Shell Model

	Calculation (units)	Description
Velocity and Position		
1	Increment time (s)	Update time by addition of time step which does not have to be uniform.
2	Update particle velocity (m/s)	Utilize acceleration computed in previous step and length of time step.
3	Determine particle position (m)	Using an average of current velocity, previous velocity and time step.
4	Determine velocity relative to melt (m/s)	Add or subtract melt velocity, to get slip velocity of the particle.
5	Update particle diameter (m)	New diameter is calculated near the end of the previous step.
6	Compute Reynolds number	Required for drag calculation and Nusselt number calculation.
7	Determine drag coefficient, C_D	Used in calculation of drag force on the particle.
8	Compute drag force (N)	Force acts on alloy particle, due to frictional interaction with fluid, in direction opposite to travel.
9	Compute particle weight (N)	Weight is one of the three forces summed to determine particle acceleration. Weight includes the alloy and steel shell (determined in previous step).
10	Calculate buoyancy force (N)	Force due to displacement of fluid by the alloy particle; this force opposes weight force.
11	Sum forces (N)	Determine net force acting on the particle by summing drag, weight, and buoyant forces.
12	Calculate acceleration (m/s^2)	Using Newton's second law, F=m·a, and the mass of the composite alloy-steel shell particle, determine acceleration. Composite particle mass is determined from the weight force.
Heat Transfer		
13	Update melt temperature (K)	Temperature of the melt is reduced using curve fits of experimentally determined heat loss.
14	Compute Nusselt number	
15	Calculate heat transfer coefficient ($W \cdot m^{-2} \cdot K^{-1}$)	Convective heat transfer coefficient used to determine energy transferred from melt to steel shell
16	Compute surface area of composite particle (m^2)	$\text{Surface Area} = 4\pi R^2$
17	Calculate Biot number	Used in calculation of heat transfer from shell to alloy particle
18	Calculate Forier number	Used in calculation of heat transfer from shell to alloy particle
19	Determine Dimensionless temperature	Used for transient conduction calculation
20	Compute alloy center and surface temperature (K)	Obtained from dimensionless temperature. Alloy surface temperature is checked to verify model behavior.

Table A.2. Steps in Steel Shell Model (cont.)

21	Calculate ratio of heat transferred	The method used to determine transient conduction results in a ratio of heat transferred (Q) to the maximum heat that could be transferred (Q_o). Q_o is the amount of energy required to raise the alloy to its melting temperature.
22	Calculate heat transferred to alloy (J)	Take difference between Q/Q_o from previous and current step to obtain amount of heat absorbed by alloy core.
23	Compute heat transferred to shell (J)	Product of composite particle surface area, heat transfer coefficient, time interval, and temperature difference between melt and melt solidification temperature.
24	Get difference between heat transferred to shell and core (J)	Subtract energy transferred into alloy from energy transferred to shell from the melt.
25	Determine mass of steel frozen or melted (kg)	Divide net energy by the sum of the latent heat and product of specific heat of the melt and temperature difference between melt and solidification temperature. $\text{Mass} = \frac{Q_{net}}{\Delta H_f + Cp(T_{melt} - T_{solidificaiton})}$
26	Update mass of shell (kg)	Add or subtract amount frozen/melted in this step to the running total.
27	Compute shell volume and add to volume of alloy (m^3)	Total composite particle volume, ignoring thermal expansion.
28	Compute composite particle radius/diameter (m)	$R = \left(\frac{3V}{4\pi}\right)^{\frac{1}{3}}$ Check for complete shell melting by comparing to initial condition (if true, then start mixing model).
29	Compute ratio of heat transferred to alloy versus total heat required to melt particle	If alloy is completely melted start mixing model; otherwise return to step 1.

BIBLIOGRAPHY

[1] Peter, J., Peaslee, K. D., Robertson, D.G., Zhang, L., and Thomas, B.G. "Introduction of a Novel, Scrap-based, Fully Continuous Steelmaking Process" Proceedings of the 2005 Conference of the Association of Iron Steel Technology Vol. 2, 2005. 623-635

[2] Peaslee, K.D., Peter, J., Robertson, D.G., Thomas, B.G., and Zhang, l. "Continuous Steel Production and Apparatus." United States Patent 7,618,582 B2, November 17, 2009

[3] Peaslee, K. D., Webber, D.S., Lekakh, S., and Randall, B., "Alloy Recovery and Control in Steel Making", Proceedings of 58th SFSA T&O conference, Steel Founders Society of America, 2005. 4.1-1 – 4.1-13

[4] Berg, H., Laux, H., Johansen, S. T., and Klevan, O. S., "Flow Pattern and Alloy Dissolution During Tapping of Steel Furnaces." Ironmaking and Steelmaking, Vol. 26, No. 2 (1999): 127-139

[5] Schade, J., Argyropoulus, S. A., and Mclean, A., "Cored-Wire Microexothermic Alloys for Tundish Metallurgy." Transactions of the Iron and Steel Society, Vol. 12 (1991): 19-31

[6] Berg, H., Laux, H., Johansen, S. T., and Klevan, O. S., "Flow Pattern and Alloy Dissolution During Tapping of Steel Furnaces." Ironmaking and Steelmaking, Vol. 26, No. 2 (1999): 127-139

[7] Zughbi, H.D. "Decarburization of Fe/C Melts in a Crucible: Effects of Gas Flow Rate and Composition." Scandinavian Journal of Metallurgy Vol. 33, No. 4 (2003): 194-202

[8] Mandal, J., Patil, S., Madan, M., and Mazumdar, D. "Mixing Time and Correlation for Ladles Stirred with Dual Porous Plugs." Metallurgical and Materials Transactions B, Vol. 36 No. 4 (2005): 479-487

[9] Szekely, J., Lehner, T., and Chang, C. "Flow Phenomena, Mixing, and Mass Transfer in Argon Stirred Ladles." Ironmaking and Steelmaking, Vol. 6, No. 6 (1979): 285-293

[10] Turkdogan, E.T. Fundamentals of Steelmaking Cambridge: The Institute of Materials, 1996

[11] Zhang, L., Aoki, J., Thomas, B.G., Peter J., and Peaslee, K.D. "Designing a New Scrap-Based Continuous Steelmaking Process using CFD Simulation." 3rd International. Congress on Science & Technology of Steelmaking, Charlotte, NC, May 9-11, 2005. 577-590.

[12] Zhang, L., Aoki, J., Thomas, B.G., Peter J., and Peaslee, K.D. "Designing a New Scrap-Based Continuous Steelmaking Process using CFD Simulation." 3rd International. Congress on Science & Technology of Steelmaking, Charlotte, NC, May 9-11, 2005. 577-590.

[13] Zhang, L., and Oeters, F., Melting and Mixing of Alloying Agents in Steel Melts : Methods of Mathematical Modeling Düsseldorf: Verlag Stahleisen, 1999.

[14] Zhang, L., and Oeters, F., Melting and Mixing of Alloying Agents in Steel Melts : Methods of Mathematical Modeling Düsseldorf: Verlag Stahleisen, 1999.

[15] Argyropoulos, S. and Guthrie, R. "Dissolution Kinetics of Ferroalloys in Steelmaking." 65th Steelmaking Conference Proceedings, Iron and Steel Society, Vol. 65 (1982). 156-167

[16] Aoki, J., Thomas, B., Peter, J., and Peaslee, K. "Experimental and Theoretical Investigation of Mixing in a Bottom Gas-Stirred Ladle." AISTech Proceedings, 2004. 1045-1056

[17] Zhang, L. and Oeters, F. "Mathematical Modeling of Alloy Melting in Steel Melts." Steel Research Vol. 70, No. 4+5, (1999): 128-134

[18] Zhang, L. and Oeters, F. "Mathematical Modeling of Alloy Melting in Steel Melts." Steel Research Vol. 70, No. 4+5, (1999): 128-134

[19] Aboutalebi, M. and Khaki, J. "Heat Transfer Modeling of the Melting of Solid Particles in an Agitated Molten Metal Bath." Canadian Metallurgical Quarterly, Vol. 37 No. 3-4 (1998): 305-311

[20] Aboutalebi, M. and Khaki, J. "Heat Transfer Modeling of the Melting of Solid Particles in an Agitated Molten Metal Bath." Canadian Metallurgical Quarterly, Vol. 37 No. 3-4 (1998): 305-311

[21] Jauhiainen, A., Jonsson, L. and Sheng, D. "Modeling of Alloy Mixing into Steel." Scandinavian Journal of Metallurgy, Vol. 30 No. 4 (2001): 242-253

[22] Aoki, J., Thomas, B., Peter, ,J., and Peaslee, K. "Experimental and Theoretical Investigation of Mixing in a Bottom Gas-Stirred Ladle." AISTech Proceedings, 2004. 1045-1056

[23] Peter, J., Unpublished Work (2005)

[24] Berg, H., Laux, H., Johansen, S. T., and Klevan, O. S., "Flow Pattern and Alloy Dissolution During Tapping of Steel Furnaces." Ironmaking and Steelmaking, Vol. 26, No. 2 (1999): 127-139

[25] Berg, H., Laux, H., Johansen, S. T., and Klevan, O. S., "Flow Pattern and Alloy Dissolution During Tapping of Steel Furnaces." Ironmaking and Steelmaking, Vol. 26, No. 2 (1999): 127-139

[26] Lee, Y, Berg, H., Jensen, B., and Sandberg, J. "Ferroalloy Size in Steelmaking." 54th Electric Furnace Conference Proceedings, Iron and Steel Society, Vol. 54 (1996). 237-242

[27] Lee, Y., Berg, H. and Jensen, B. "Dissolution Kinetics of Ferroalloys in Steelmaking Processes." Ironmaking and Steelmaking, Vol. 22 No. 6 (1995): 486-494

[28] Crawford, G.P. "Wire Injection of Metallurgical Powders into Molten Steel." Steel Times International Vol. 16 No. 4 (1992): 31-34

[29] Ferroalloys & Alloying Additives Online Handbook. 15 Jul. 2011 http://www.metallurgvanadium.com/contents.html

[30] Crawford, G.P. "Wire Injection of Metallurgical Powders into Molten Steel." Steel Times International Vol. 16 No. 4 (1992): 31-34

[31] Tateyama, M., Hiraga, Y., Yaniguchi, S., Okimura, T., and Hirata, K. "Deoxidation and Desulfurization of Molten Steel with Mg Containing Wire." SEAISI Quarterly, Vol. 29 No. 4 (2000): 43-47

[32] Argyropoulos, S. and Guthrie, R. "Dissolution Kinetics of Ferroalloys in Steelmaking." 65th Steelmaking Conference Proceedings, Iron and Steel Society, Vol. 65 (1982). 156-167

[33] Chart T.G. and Kubachewski, O. "Metallurgical Chemistry." Proceedings of a symposium held at Brunel University and the National Physical Laboratory on the 14, 15 and 16 July 1971. 567

[34] Zhang, L. and Oeters, F. "Melting and Dissolution of High-melting Alloys in Steel Melts" Steel Research Vol. 71 No.5 (2000): 141-144

[35] King, R.J. and Chilcott, W.R. "Chilling Effects of Ferroalloy Additions to Liquid Steel." Physical Chemistry of Production or Use of Alloy Additives, 103rd AIME Annual Meeting Proceedings, 1974. 69-83

[36] King, R.J. and Chilcott, W.R. "Chilling Effects of Ferroalloy Additions to Liquid Steel." Physical Chemistry of Production or Use of Alloy Additives, 103rd AIME Annual Meeting Proceedings, 1974. 69-83

[37] King, R.J. and Chilcott, W.R. "Chilling Effects of Ferroalloy Additions to Liquid Steel." Physical Chemistry of Production or Use of Alloy Additives, 103rd AIME Annual Meeting Proceedings, 1974. 69-83

[38] Schade, J., Argyropoulus, S. A., and Mclean, A., "Cored-Wire Microexothermic Alloys for Tundish Metallurgy." Transactions of the Iron and Steel Society, Vol. 12 (1991): 19-31

[39] Ferroalloys & Alloying Additives Online Handbook. 15 Jul. 2011 http://www.metallurgvanadium.com/contents.html

[40] Ferroalloys & Alloying Additives Online Handbook. 15 Jul. 2011 http://www.metallurgvanadium.com/contents.html

[41] Ferroalloys & Alloying Additives Online Handbook. 15 Jul. 2011 http://www.metallurgvanadium.com/contents.html

[42] Argyropoulos, S. and Guthrie, R. "Dissolution Kinetics of Ferroalloys in Steelmaking." 65th Steelmaking Conference Proceedings, Iron and Steel Society, Vol. 65 (1982). 156-167

[43] Argyropoulos, S. and Guthrie, R. "Dissolution Kinetics of Ferroalloys in Steelmaking." 65th Steelmaking Conference Proceedings, Iron and Steel Society, Vol. 65 (1982). 156-167

[44] Argyropoulos, S. and Guthrie, R. "Dissolution Kinetics of Ferroalloys in Steelmaking." 65th Steelmaking Conference Proceedings, Iron and Steel Society, Vol. 65 (1982). 156-167

[45] Argyropoulos, S. and Guthrie, R. "Dissolution Kinetics of Ferroalloys in Steelmaking." 65th Steelmaking Conference Proceedings, Iron and Steel Society, Vol. 65 (1982). 156-167

[46] Barbalace, K. “Periodic Table of the Elements – Tin.” 23 Oct. 2010 http://EnvironmentalChemistry.com/yogi/periodic/Sn.html

[47] King, R.J. and Chilcott, W.R. “Chilling Effects of Ferroalloy Additions to Liquid Steel.” Physical Chemistry of Production or Use of Alloy Additives, 103rd AIME Annual Meeting Proceedings, 1974. 69-83

[48] Zhang, L., and Oeters, F., Melting and Mixing of Alloying Agents in Steel Melts : Methods of Mathematical Modeling Düsseldorf: Verlag Stahleisen, 1999.

[49] Zhang, L., and Oeters, F., Melting and Mixing of Alloying Agents in Steel Melts : Methods of Mathematical Modeling Düsseldorf: Verlag Stahleisen, 1999.

[50] Zhang, L., and Oeters, F., Melting and Mixing of Alloying Agents in Steel Melts : Methods of Mathematical Modeling Düsseldorf: Verlag Stahleisen, 1999.

[51] Zhang, L., and Oeters, F., Melting and Mixing of Alloying Agents in Steel Melts : Methods of Mathematical Modeling Düsseldorf: Verlag Stahleisen, 1999.

[52] Zhang, L., and Oeters, F., Melting and Mixing of Alloying Agents in Steel Melts : Methods of Mathematical Modeling Düsseldorf: Verlag Stahleisen, 1999.

[53] Zhang, L., and Oeters, F., Melting and Mixing of Alloying Agents in Steel Melts : Methods of Mathematical Modeling Düsseldorf: Verlag Stahleisen, 1999.

[54] Zhang, L., and Oeters, F., Melting and Mixing of Alloying Agents in Steel Melts : Methods of Mathematical Modeling Düsseldorf: Verlag Stahleisen, 1999.

[55] Zhang, L., and Oeters, F., Melting and Mixing of Alloying Agents in Steel Melts : Methods of Mathematical Modeling Düsseldorf: Verlag Stahleisen, 1999.

[56] Hulka, K. “Ferroniobium – Alloying Techniques.” 21Jun. 2010 <http://www.cbmm.com.br/portug/sources/techlib/info/feralloy/feralloy.htm accessed>

[57] Zhang, L., and Oeters, F., Melting and Mixing of Alloying Agents in Steel Melts : Methods of Mathematical Modeling Düsseldorf: Verlag Stahleisen, 1999.

[58] Zhang, L., and Oeters, F., Melting and Mixing of Alloying Agents in Steel Melts : Methods of Mathematical Modeling Düsseldorf: Verlag Stahleisen, 1999.

[59] Zhang, L., and Oeters, F., Melting and Mixing of Alloying Agents in Steel Melts : Methods of Mathematical Modeling Düsseldorf: Verlag Stahleisen, 1999.

[60] Zhang, L., and Oeters, F., Melting and Mixing of Alloying Agents in Steel Melts : Methods of Mathematical Modeling Düsseldorf: Verlag Stahleisen, 1999.

[61] Zhang, L., and Oeters, F., Melting and Mixing of Alloying Agents in Steel Melts : Methods of Mathematical Modeling Düsseldorf: Verlag Stahleisen, 1999.

[62] King, R.J. and Chilcott, W.R. “Chilling Effects of Ferroalloy Additions to Liquid Steel.” Physical Chemistry of Production or Use of Alloy Additives, 103rd AIME Annual Meeting Proceedings, 1974. 69-83

[63] Zhang, L., and Oeters, F., Melting and Mixing of Alloying Agents in Steel Melts : Methods of Mathematical Modeling Düsseldorf: Verlag Stahleisen, 1999.

[64] Zhang, L., and Oeters, F., Melting and Mixing of Alloying Agents in Steel Melts : Methods of Mathematical Modeling Düsseldorf: Verlag Stahleisen, 1999.

[65] Zhang, L., and Oeters, F., Melting and Mixing of Alloying Agents in Steel Melts : Methods of Mathematical Modeling Düsseldorf: Verlag Stahleisen, 1999.

[66] Zhang, L., and Oeters, F., Melting and Mixing of Alloying Agents in Steel Melts : Methods of Mathematical Modeling Düsseldorf: Verlag Stahleisen, 1999.

[67] Zhang, L., and Oeters, F., Melting and Mixing of Alloying Agents in Steel Melts : Methods of Mathematical Modeling Düsseldorf: Verlag Stahleisen, 1999.

[68] King, R.J. and Chilcott, W.R. “Chilling Effects of Ferroalloy Additions to Liquid Steel.” Physical Chemistry of Production or Use of Alloy Additives, 103rd AIME Annual Meeting Proceedings, 1974. 69-83

[69] Argyropoulos, S.A. “Dissolution Characteristics of Ferroalloys in Liquid Steel.” 41st Electric Furnace Conference Proceedings, 1983. 81-93

[70] Argyropoulos, S.A. “Dissolution Characteristics of Ferroalloys in Liquid Steel.” 41st Electric Furnace Conference Proceedings, 1983. 81-93

[71] Argyropoulos, S.A. “Dissolution Characteristics of Ferroalloys in Liquid Steel.” 41st Electric Furnace Conference Proceedings, 1983. 81-93

[72] Argyropoulos, S.A. “Dissolution Characteristics of Ferroalloys in Liquid Steel.” 41st Electric Furnace Conference Proceedings, 1983. 81-93

[73] Barbalace, K. “Periodic Table of the Elements – Tin.” 23 Oct. 2010 http://EnvironmentalChemistry.com/yogi/periodic/Sn.html

[74] Argyropoulos, S. and Guthrie, R. “Dissolution Kinetics of Ferroalloys in Steelmaking.” 65th Steelmaking Conference Proceedings, Iron and Steel Society, Vol. 65 (1982). 156-167

[75] Argyropoulos, S. and Guthrie, R. “Dissolution Kinetics of Ferroalloys in Steelmaking.” 65th Steelmaking Conference Proceedings, Iron and Steel Society, Vol. 65 (1982). 156-167

[76] Argyropoulos, S. and Guthrie, R. “Dissolution Kinetics of Ferroalloys in Steelmaking.” 65th Steelmaking Conference Proceedings, Iron and Steel Society, Vol. 65 (1982). 156-167

[77] Lee, Y. E., Klevan, O. and Jensen, B. “Dissolution of FeSi Alloys in a Steel Melt.” 55th Electric Furnace Conference Proceedings, Iron and Steel Society, Vol. 55 (1997). 289-295

[78] Argyropoulos, S. and Guthrie, R. "Dissolution Kinetics of Ferroalloys in Steelmaking." 65th Steelmaking Conference Proceedings, Iron and Steel Society, Vol. 65 (1982). 156-167

[79] Argyropoulos, S. A. "On the Recovery and Solution Rate of Ferroalloys." Transactions of the Iron and Steel Society, Vol. 12 (May 1990): 77-86

[80] Lee, Y., Berg, H. and Jensen, B. "Dissolution Kinetics of Ferroalloys in Steelmaking Processes." Ironmaking and Steelmaking, Vol. 22 No. 6 (1995): 486-494

[81] Argyropoulos, S. A. "On the Recovery and Solution Rate of Ferroalloys." Transactions of the Iron and Steel Society, Vol. 12 (May 1990): 77-86

[82] Argyropoulos, S.A. "Dissolution Characteristics of Ferroalloys in Liquid Steel." 41st Electric Furnace Conference Proceedings, 1983. 81-93

[83] Gourtsoyannis, L., Guthrie R.I.L. and Ratz, G.A. "The Dissolution of Ferromolybdenum, Ferroniobium, and Rare Earth Silicide in Cast Iron and Steel Melts." 42nd Electric Furnace Conference Proceedings 1984. 119-132

[84] Gourtsoyannis, L., Guthrie R.I.L. and Ratz, G.A. "The Dissolution of Ferromolybdenum, Ferroniobium, and Rare Earth Silicide in Cast Iron and Steel Melts." 42nd Electric Furnace Conference Proceedings 1984. 119-132

[85] Gourtsoyannis, L., Guthrie R.I.L. and Ratz, G.A. "The Dissolution of Ferromolybdenum, Ferroniobium, and Rare Earth Silicide in Cast Iron and Steel Melts." 42nd Electric Furnace Conference Proceedings 1984. 119-132

[86] Zhang, L. and Oeters, F. "Melting and Dissolution of High-melting Alloys in Steel Melts" Steel Research Vol. 71 No.5 (2000): 141-144

[87] Zhang, L., and Oeters, F., Melting and Mixing of Alloying Agents in Steel Melts : Methods of Mathematical Modeling Düsseldorf: Verlag Stahleisen, 1999.

[88] Zhang, L., and Oeters, F., Melting and Mixing of Alloying Agents in Steel Melts : Methods of Mathematical Modeling Düsseldorf: Verlag Stahleisen, 1999.

[89] Zhang, L., and Oeters, F., Melting and Mixing of Alloying Agents in Steel Melts : Methods of Mathematical Modeling Düsseldorf: Verlag Stahleisen, 1999.

[90] Zhang, L., and Oeters, F., Melting and Mixing of Alloying Agents in Steel Melts : Methods of Mathematical Modeling Düsseldorf: Verlag Stahleisen, 1999.

[91] Zhang, L., and Oeters, F., Melting and Mixing of Alloying Agents in Steel Melts : Methods of Mathematical Modeling Düsseldorf: Verlag Stahleisen, 1999.

[92] Zhang, L., and Oeters, F., Melting and Mixing of Alloying Agents in Steel Melts : Methods of Mathematical Modeling Düsseldorf: Verlag Stahleisen, 1999.

[93] Zhang, L., and Oeters, F., Melting and Mixing of Alloying Agents in Steel Melts : Methods of Mathematical Modeling Düsseldorf: Verlag Stahleisen, 1999.

[94] Zhang, L., and Oeters, F., Melting and Mixing of Alloying Agents in Steel Melts : Methods of Mathematical Modeling Düsseldorf: Verlag Stahleisen, 1999.

[95] Lee, Y., Berg, H. and Jensen, B. "Dissolution Kinetics of Ferroalloys in Steelmaking Processes." Ironmaking and Steelmaking, Vol. 22 No. 6 (1995): 486-494

[96] Argyropoulos, S. and Guthrie, R. "Dissolution Kinetics of Ferroalloys in Steelmaking." 65th Steelmaking Conference Proceedings, Iron and Steel Society, Vol. 65 (1982). 156-167

[97] Zhang, L., and Oeters, F., Melting and Mixing of Alloying Agents in Steel Melts : Methods of Mathematical Modeling Düsseldorf: Verlag Stahleisen, 1999.

[98] Argyropoulos, S. and Guthrie, R. "Dissolution Kinetics of Ferroalloys in Steelmaking." 65th Steelmaking Conference Proceedings, Iron and Steel Society, Vol. 65 (1982). 156-167

[99] Lee, Y., Berg, H. and Jensen, B. "Dissolution Kinetics of Ferroalloys in Steelmaking Processes." Ironmaking and Steelmaking, Vol. 22 No. 6 (1995): 486-494

[100] Zhang, L., and Oeters, F., Melting and Mixing of Alloying Agents in Steel Melts : Methods of Mathematical Modeling Düsseldorf: Verlag Stahleisen, 1999.

[101] Ferroalloys & Alloying Additives Online Handbook. 15 Jul. 2011 http://www.metallurgvanadium.com/contents.html

[102] Zhang, L. and Oeters, F. "Mathematical Modeling of Alloy Melting in Steel Melts." Steel Research Vol. 70, No. 4+5, (1999): 128-134

[103] Zhang, L., and Oeters, F., Melting and Mixing of Alloying Agents in Steel Melts : Methods of Mathematical Modeling Düsseldorf: Verlag Stahleisen, 1999.

[104] Incropera, F. and De Witt, D. Fundamentals of Heat and Mass Transfer 3rd ed. Wiley 1990.

[105] Zhang, L., and Oeters, F., Melting and Mixing of Alloying Agents in Steel Melts : Methods of Mathematical Modeling Düsseldorf: Verlag Stahleisen, 1999.

[106] Aoki, J., Thomas, B., Peter ,J., and Peaslee, K. "Experimental and Theoretical Investigation of Mixing in a Bottom Gas-Stirred Ladle." AISTech Proceedings, 2004. 1045-1056

[107] Poirier, D. and Geiger, G. Transport Phenomena in Materials Processing" The Minerals, Metals, and Materials Society 1994.

[108] Poirier, D. and Geiger, G. Transport Phenomena in Materials Processing" The Minerals, Metals, and Materials Society 1994.

[109] Argyropoulos, S. and Guthrie, R. "Dissolution Kinetics of Ferroalloys in Steelmaking." 65th Steelmaking Conference Proceedings, Iron and Steel Society, Vol. 65 (1982). 156-167

[110] Zhang, L., and Oeters, F., Melting and Mixing of Alloying Agents in Steel Melts : Methods of Mathematical Modeling Düsseldorf: Verlag Stahleisen, 1999.

[111] Zhang, L., and Oeters, F., Melting and Mixing of Alloying Agents in Steel Melts : Methods of Mathematical Modeling Düsseldorf: Verlag Stahleisen, 1999.

[112] Argyropoulos, S. and Guthrie, R. "Dissolution Kinetics of Ferroalloys in Steelmaking." 65th Steelmaking Conference Proceedings, Iron and Steel Society, Vol. 65 (1982). 156-167

[113] Zhang, L., and Oeters, F., Melting and Mixing of Alloying Agents in Steel Melts : Methods of Mathematical Modeling Düsseldorf: Verlag Stahleisen, 1999.

[114] Argyropoulos, S. A. and Sismanis, P. "The Mass Transfer Kinetics of Niobium Solution into Liquid Steel." Metallurgical and Materials Transactions B Vol. 22 No. 4 (1991): 417-427

[115] Zhang, L. and Oeters, F. "Melting and Dissolution of High-melting Alloys in Steel Melts" Steel Research Vol. 71 No.5 (2000): 141-144

[116] Zhang, L. and Oeters, F. "Melting and Dissolution of High-melting Alloys in Steel Melts" Steel Research Vol. 71 No.5 (2000): 141-144

[117] Zhang, L. and Oeters, F. "Melting and Dissolution of High-melting Alloys in Steel Melts" Steel Research Vol. 71 No.5 (2000): 141-144

[118] Zhang, L., and Oeters, F., Melting and Mixing of Alloying Agents in Steel Melts : Methods of Mathematical Modeling Düsseldorf: Verlag Stahleisen, 1999

[119] Argyropoulos, S. and Guthrie, R. "Dissolution Kinetics of Ferroalloys in Steelmaking." 65th Steelmaking Conference Proceedings, Iron and Steel Society, Vol. 65 (1982). 156-167

[120] Argyropoulos, S. and Guthrie, R. "Dissolution Kinetics of Ferroalloys in Steelmaking." 65th Steelmaking Conference Proceedings, Iron and Steel Society, Vol. 65 (1982). 156-167

[121] Argyropoulos, S. and Guthrie, R. "Dissolution Kinetics of Ferroalloys in Steelmaking." 65th Steelmaking Conference Proceedings, Iron and Steel Society, Vol. 65 (1982). 156-167

[122] Aoki, J., Thomas, B., Peter, J., and Peaslee, K. "Experimental and Theoretical Investigation of Mixing in a Bottom Gas-Stirred Ladle." AISTech Proceedings, 2004. 1045-1056

[123] Oeters, F. Metallurgy of Steelmaking Düsseldorf: Verlag Stahleisen 1994.

[124] Oeters, F. Metallurgy of Steelmaking Düsseldorf: Verlag Stahleisen 1994.

[125] Oeters, F. Metallurgy of Steelmaking Düsseldorf: Verlag Stahleisen 1994.

[126] Mazumdar, D. and Guthrie, R.I.L. "Mixing Models for Gas Stirred Metallurgical Reactors." Metallurgical Transactions B Vol. 17 No. 4 (1986): 725-733

[127] Mazumdar, D. and Guthrie, R.I.L. "Mixing Models for Gas Stirred Metallurgical Reactors." Metallurgical Transactions B Vol. 17 No. 4 (1986): 725-733

[128] Mietz, J. and Oeters, F. "Model Experiments on Mixing Phenomena in Gas-Stirred Melts." Steel Research Vol. 59 (1988): 452-59

[129] Mandal, J., Patil, S., Madan, M., and Mazumdar, D. “Mixing Time and Correlation for Ladles Stirred with Dual Porous Plugs.” Metallurgical and Materials Transactions B, Vol. 36 No. 4 (2005): 479-487

[130] Naksnishi, K., Fujii, T. and Szekely, J. “Possible Relationship Between Energy Dissipation and Agitation in Steel Processing Operations.” Ironmaking Steelmaking No. 2 (1975): 193-197

[131] Naksnishi, K., Fujii, T. and Szekely, J. “Possible Relationship Between Energy Dissipation and Agitation in Steel Processing Operations.” Ironmaking Steelmaking No. 2 (1975): 193-197

[132] Mazumdar, D. and Guthrie, R.I.L. “Mixing Models for Gas Stirred Metallurgical Reactors.” Metallurgical Transactions B Vol. 17 No. 4 (1986): 725-733

[133] Mazumdar, D. and Guthrie, R. “Mixing Times and Correlations for Gas Stirred Ladle Systems.” Iron and Steel Society Transactions, Vol. 26 No. 9 (1999): 89-96

[134] Mazumdar, D. and Guthrie, R. “Mixing Times and Correlations for Gas Stirred Ladle Systems.” Iron and Steel Society Transactions, Vol. 26 No. 9 (1999): 89-96

[135] Mazumdar, D. and Guthrie, R. “Mixing Times and Correlations for Gas Stirred Ladle Systems.” Iron and Steel Society Transactions, Vol. 26 No. 9 (1999): 89-96

[136] Mazumdar, D. and Guthrie, R. “Mixing Times and Correlations for Gas Stirred Ladle Systems.” Iron and Steel Society Transactions, Vol. 26 No. 9 (1999): 89-96

[137] Mazumdar, D. “Communication: Dynamic Similarity Considerations in Gas-Stirred Ladle Systems.” Metallurgical Transactions B Vol. 21 No.5 (1990): 925-928

[138] Mazumdar, D., Kim, H.B. and Guthrie, R.I.L. “Modeling Criteria for Flow Simulation in Gas Stirred Ladles: Experimental Study.” Ironmaking and Steelmaking, Vol. 27 No. 4 (2000): 302-309

[139] Mazumdar, D., Kim, H.B. and Guthrie, R.I.L. “Modeling Criteria for Flow Simulation in Gas Stirred Ladles: Experimental Study.” Ironmaking and Steelmaking, Vol. 27 No. 4 (2000): 302-309

[140] Oeters, F. Metallurgy of Steelmaking Düsseldorf: Verlag Stahleisen 1994.

[141] Oeters, F. Metallurgy of Steelmaking Düsseldorf: Verlag Stahleisen 1994.

[142] Oeters, F. Metallurgy of Steelmaking Düsseldorf: Verlag Stahleisen 1994.

[143] Oeters, F. Metallurgy of Steelmaking Düsseldorf: Verlag Stahleisen 1994.

[144] Oeters, F. Metallurgy of Steelmaking Düsseldorf: Verlag Stahleisen 1994.

[145] Oeters, F. Metallurgy of Steelmaking Düsseldorf: Verlag Stahleisen 1994.

[146] Oeters, F. Metallurgy of Steelmaking Düsseldorf: Verlag Stahleisen 1994.

[147] Oeters, F. Metallurgy of Steelmaking Düsseldorf: Verlag Stahleisen 1994.

[148] Oeters, F. Metallurgy of Steelmaking Düsseldorf: Verlag Stahleisen 1994.

[149] Oeters, F. Metallurgy of Steelmaking Düsseldorf: Verlag Stahleisen 1994.

[150] Zhang, L. and Oeters, F. "Melting and Dissolution of High-melting Alloys in Steel Melts" Steel Research Vol. 71 No.5 (2000): 141-144

[151] Zhang, L., and Oeters, F., Melting and Mixing of Alloying Agents in Steel Melts : Methods of Mathematical Modeling Düsseldorf: Verlag Stahleisen, 1999.

[152] Oeters, F. Metallurgy of Steelmaking Düsseldorf: Verlag Stahleisen 1994.

[153] Aboutalebi, M. and Khaki, J. "Heat Transfer Modeling of the Melting of Solid Particles in an Agitated Molten Metal Bath." Canadian Metallurgical Quarterly, Vol. 37 No. 3-4 (1998): 305-311

[154] Argyropoulos, S. and Guthrie, R. "Dissolution Kinetics of Ferroalloys in Steelmaking." 65th Steelmaking Conference Proceedings, Iron and Steel Society, Vol. 65 (1982). 156-167

[155] Mazumdar, D. and Guthrie, R.I.L. "Mixing Models for Gas Stirred Metallurgical Reactors." Metallurgical Transactions B Vol. 17 No. 4 (1986): 725-733

[156] Zhang, L., Aoki, J., Thomas, B.G., Peter J., and Peaslee, K.D. "Designing a New Scrap-Based Continuous Steelmaking Process using CFD Simulation." 3rd International. Congress on Science & Technology of Steelmaking, Charlotte, NC, May 9-11, 2005. 577-590.

[157] Kaltek 4000 Product Literature, Foseco Foundry Division of Vesuvius, 2009.

[158] Rotameters: Variable Area Flowmeters Tech Info. 5 Jul. 2011 http://www.coleparmer.com/techinfo/techinfo.asp?htmlfile=V_AFLowRotometers.htm&ID=813

[159] Aoki, J., Thomas, B., Peter, J., and Peaslee, K. "Experimental and Theoretical Investigation of Mixing in a Bottom Gas-Stirred Ladle." AISTech Proceedings, 2004. 1045-1056

[160] Zhang, L., Aoki, J., Thomas, B.G., Peter J., and Peaslee, K.D. "Designing a New Scrap-Based Continuous Steelmaking Process using CFD Simulation." 3rd International. Congress on Science & Technology of Steelmaking, Charlotte, NC, May 9-11, 2005. 577-590.

[161] Aoki, J., Zhang, L., Thomas, B. "Modeling of Inclusion Removal in Ladle Refining." 3rd International Congress on the Science & Technology of Steelmaking, Charlotte, NC, May 8-11, 2005. 577-590

[162] Aoki, J., Thomas, B., Peter, J., and Peaslee, K. "Experimental and Theoretical Investigation of Mixing in a Bottom Gas-Stirred Ladle." AISTech Proceedings, 2004. 1045-1056

[163] "The Euler-Lagrange Approach." Fluent 6.3 User's Guide 25 Jul. 2011 <http://my.fit.edu/itresources/manuals/fluent6.3/help/html/ug/node806.htm>

[164] "Multiphase Flow Regimes." Fluent 6.3 User's Guide 25 Jul. 2011 < http://my.fit.edu/itresources/manuals/fluent6.3/help/html/ug/node873.htm>

[165] Zhang, L., and Oeters, F., Melting and Mixing of Alloying Agents in Steel Melts : Methods of Mathematical Modeling Düsseldorf: Verlag Stahleisen, 1999.

[166] Aoki, J., Thomas, B., Peter, J., and Peaslee, K. "Experimental and Theoretical Investigation of Mixing in a Bottom Gas-Stirred Ladle." AISTech Proceedings, 2004. 1045-1056

[167] Guthrie, R.I.L. Engineering in Process Metallurgy, Oxford Science Publications, 1992.

[168] Incropera, F. and De Witt, D. Fundamentals of Heat and Mass Transfer 3rd ed. Wiley 1990.

[169] Incropera, F. and De Witt, D. Fundamentals of Heat and Mass Transfer 3rd ed. Wiley 1990.

[170] Heisler, M. "Temperature Charts for Induction and Constant Temperature Heating." Transactions of ASME Vol. 69 (1947): 227-236

[171] Aoki, J., Thomas, B., Peter, J., and Peaslee, K. "Experimental and Theoretical Investigation of Mixing in a Bottom Gas-Stirred Ladle." AISTech Proceedings, 2004. 1045-1056

[172] Incropera, F. and De Witt, D. Fundamentals of Heat and Mass Transfer 3rd ed. Wiley 1990.

[173] Zhang, L., Aoki, J., Thomas, B.G., Peter J., and Peaslee, K.D. "Designing a New Scrap-Based Continuous Steelmaking Process using CFD Simulation." 3rd International. Congress on Science & Technology of Steelmaking, Charlotte, NC, May 9-11, 2005. 577-590.

[174] Aoki, J., Thomas, B., Peter, J., and Peaslee, K. "Experimental and Theoretical Investigation of Mixing in a Bottom Gas-Stirred Ladle." AISTech Proceedings, 2004. 1045-1056

[175] Zhang, L., Aoki, J., Thomas, B.G., Peter J., and Peaslee, K.D. "Designing a New Scrap-Based Continuous Steelmaking Process using CFD Simulation." 3rd International. Congress on Science & Technology of Steelmaking, Charlotte, NC, May 9-11, 2005. 577-590.

[176] Zhang, L. and Oeters, F. "Mathematical Modeling of Alloy Melting in Steel Melts." Steel Research Vol. 70, No. 4+5, (1999): 128-134

[177] Zhang, L., Aoki, J., Thomas, B.G., Peter J., and Peaslee, K.D. "Designing a New Scrap-Based Continuous Steelmaking Process using CFD Simulation." 3rd International. Congress on Science & Technology of Steelmaking, Charlotte, NC, May 9-11, 2005. 577-590.

[178] Oeters, F. Metallurgy of Steelmaking Düsseldorf: Verlag Stahleisen 1994.

[179] Mazumdar, D. and Guthrie, R.I.L. "Mixing Models for Gas Stirred Metallurgical Reactors." Metallurgical Transactions B Vol. 17 No. 4 (1986): 725-733

[180] Oeters, F. Metallurgy of Steelmaking Düsseldorf: Verlag Stahleisen 1994.

[181] Oeters, F. Metallurgy of Steelmaking Düsseldorf: Verlag Stahleisen 1994.

[182] Oeters, F. Metallurgy of Steelmaking Düsseldorf: Verlag Stahleisen 1994.

[183] Zhang, L. and Oeters, F. "Melting and Dissolution of High-melting Alloys in Steel Melts" Steel Research Vol. 71 No.5 (2000): 141-144

[184] Zhang, L., and Oeters, F., Melting and Mixing of Alloying Agents in Steel Melts : Methods of Mathematical Modeling Düsseldorf: Verlag Stahleisen, 1999.

[185] Zhang, L., and Oeters, F., Melting and Mixing of Alloying Agents in Steel Melts : Methods of Mathematical Modeling Düsseldorf: Verlag Stahleisen, 1999.

[186] Zhang, L. and Oeters, F. "Mathematical Modeling of Alloy Melting in Steel Melts." Steel Research Vol. 70, No. 4+5, (1999): 128-134

[187] Paul, E., Swartzendruber, P. E. "Fe (Iron) Binary Alloy Phase Diagrams: Fe-Nb." ASM Handbook Vol. 3, 10th ed. (online).

[188] Guthrie, R.I.L. Engineering in Process Metallurgy, Oxford Science Publications, 1992.

[189] "Terminal Velocity." NASA Glenn Research Center, 12 Jun. 2011 < http://www.grc.nasa.gov/WWW/K-12/airplane/termv.html>

[190] Ferroalloys & Alloying Additives Online Handbook. 15 Jul. 2011 http://www.metallurgvanadium.com/contents.html

[191] Aoki, J., Thomas, B., Peter, J., and Peaslee, K. "Experimental and Theoretical Investigation of Mixing in a Bottom Gas-Stirred Ladle." AISTech Proceedings, 2004. 1045-1056

[192] Aoki, J., Thomas, B., Peter, J., and Peaslee, K. "Experimental and Theoretical Investigation of Mixing in a Bottom Gas-Stirred Ladle." AISTech Proceedings, 2004. 1045-1056

[193] Aoki, J., Thomas, B., Peter, J., and Peaslee, K. "Experimental and Theoretical Investigation of Mixing in a Bottom Gas-Stirred Ladle." AISTech Proceedings, 2004. 1045-1056

[194] Gourtsoyannis, L., Guthrie R.I.L. and Ratz, G.A. "The Dissolution of Ferromolybdenum, Ferroniobium, and Rare Earth Silicide in Cast Iron and Steel Melts." 42nd Electric Furnace Conference Proceedings 1984. 119-132

[195] Argyropoulos, S. A. and Sismanis, P. "The Mass Transfer Kinetics of Niobium Solution into Liquid Steel." Metallurgical and Materials Transactions B Vol. 22 No. 4 (1991): 417-427

[196] Gourtsoyannis, L., Guthrie R.I.L. and Ratz, G.A. "The Dissolution of Ferromolybdenum, Ferroniobium, and Rare Earth Silicide in Cast Iron and Steel Melts." 42nd Electric Furnace Conference Proceedings 1984. 119-132

[197] Gourtsoyannis, L., Guthrie R.I.L. and Ratz, G.A. "The Dissolution of Ferromolybdenum, Ferroniobium, and Rare Earth Silicide in Cast Iron and Steel Melts." 42nd Electric Furnace Conference Proceedings 1984. 119-132

[198] Turkdogan, E.T. Fundamentals of Steelmaking Cambridge: The Institute of Materials, 1996

[199] Lee, Y, Berg, H., Jensen, B., and Sandberg, J. "Ferroalloy Size in Steelmaking." 54th Electric Furnace Conference Proceedings, Iron and Steel Society, Vol. 54 (1996). 237-242

[200] Sismanis, P.G. and Argyropoulus, S. A. "The dissolution of Niobium, Boron, and Zirconium." 45th Electric Furnace Conference Proceedings, Vol. 45, Iron and Steel Society, 1987. 39-47

[201] Zhang, L., and Oeters, F., Melting and Mixing of Alloying Agents in Steel Melts : Methods of Mathematical Modeling Düsseldorf: Verlag Stahleisen, 1999.

[202] Whitaker, S. "Forced Convection Heat Transfer Correlations for Flow in Pipes, Past Flat Plates, Single Cylinders, Single Spheres, and For Flow in Packed Beds and Tube Bundles." AIChE Journal Vol.18 No. 2 (1972): 361-371.

[203] Gourtsoyannis, L., Guthrie R.I.L. and Ratz, G.A. "The Dissolution of Ferromolybdenum, Ferroniobium, and Rare Earth Silicide in Cast Iron and Steel Melts." 42nd Electric Furnace Conference Proceedings 1984. 119-132

[204] Argyropoulos, S. and Guthrie, R. "Dissolution Kinetics of Ferroalloys in Steelmaking." 65th Steelmaking Conference Proceedings, Iron and Steel Society, Vol. 65 (1982). 156-167

[205] Gourtsoyannis, L., Guthrie R.I.L. and Ratz, G.A. "The Dissolution of Ferromolybdenum, Ferroniobium, and Rare Earth Silicide in Cast Iron and Steel Melts." 42nd Electric Furnace Conference Proceedings 1984. 119-132

[206] Zhang, L., Aoki, J., Thomas, B.G., Peter J., and Peaslee, K.D. "Designing a New Scrap-Based Continuous Steelmaking Process using CFD Simulation." 3rd International. Congress on Science & Technology of Steelmaking, Charlotte, NC, May 9-11, 2005. 577-590.

[207] Aoki, J., Thomas, B., Peter, J., and Peaslee, K. "Experimental and Theoretical Investigation of Mixing in a Bottom Gas-Stirred Ladle." AISTech Proceedings, 2004. 1045-1056

[208] Zhang, L., Aoki, J., Thomas, B.G., Peter J., and Peaslee, K.D. "Designing a New Scrap-Based Continuous Steelmaking Process using CFD Simulation." 3rd International. Congress on Science & Technology of Steelmaking, Charlotte, NC, May 9-11, 2005. 577-590.

[209] Lee, Y, Berg, H., Jensen, B., and Sandberg, J. "Ferroalloy Size in Steelmaking." 54th Electric Furnace Conference Proceedings, Iron and Steel Society, Vol. 54 (1996). 237-242

[210] Aoki, J., Thomas, B., Peter, J., and Peaslee, K. "Experimental and Theoretical Investigation of Mixing in a Bottom Gas-Stirred Ladle." AISTech Proceedings, 2004. 1045-1056

[211] Aoki, J., Thomas, B., Peter, J., and Peaslee, K. "Experimental and Theoretical Investigation of Mixing in a Bottom Gas-Stirred Ladle." AISTech Proceedings, 2004. 1045-1056

VITA

Darryl Scott Webber is a native of Montana. He received a Bachelor of Science degree in Engineering Science from Montana College of Mineral Science and Technology (1992) and a Master of Science degree in Metallurgical Engineering from Montana Tech of the University of Montana (1998). Mr. Webber's Master's thesis focused on melt decontamination of radioactive scrap metal.

Prior to studying at Missouri S&T, Mr. Webber was a research and development engineer for Lockheed Martin, where he developed melting equipment and techniques for reactive and refractory metals. In addition, Mr. Webber worked on various radioactive waste vitrification projects.

Mr. Webber joined the faculty of the Wade Department of Mechanical and Aerospace Engineering at Trine University (formerly Tri-State University) in January of 2006. He serves as the Foundry Educational Foundation Key Professor, Materials Advantage/American Foundry Society advisor, and as faculty advisor for the Tri-State chapter of Delta Chi. He has been recognized with two John McKetta teaching awards, an Upstate Indiana Business Journal Future 40 award, and two Outstanding Faculty Advisor awards from Delta Chi International.

Mr. Webber has been married for more than nineteen years to his wife Katherine. They live with their three children, Kiley, Keagan, and Drake in Angola, Indiana.